


2022

## Characterization and Coherent Spin Selective Manipulation of Quantum Dot Energy Levels

Tristan Anthony Wilkinson  
West Virginia University, [taw0035@mix.wvu.edu](mailto:taw0035@mix.wvu.edu)

Follow this and additional works at: <https://researchrepository.wvu.edu/etd>

 Part of the [Condensed Matter Physics Commons](#), [Optics Commons](#), and the [Quantum Physics Commons](#)

---

### Recommended Citation

Wilkinson, Tristan Anthony, "Characterization and Coherent Spin Selective Manipulation of Quantum Dot Energy Levels" (2022). *Graduate Theses, Dissertations, and Problem Reports*. 11286.  
<https://researchrepository.wvu.edu/etd/11286>

This Dissertation is protected by copyright and/or related rights. It has been brought to you by the The Research Repository @ WVU with permission from the rights-holder(s). You are free to use this Dissertation in any way that is permitted by the copyright and related rights legislation that applies to your use. For other uses you must obtain permission from the rights-holder(s) directly, unless additional rights are indicated by a Creative Commons license in the record and/ or on the work itself. This Dissertation has been accepted for inclusion in WVU Graduate Theses, Dissertations, and Problem Reports collection by an authorized administrator of The Research Repository @ WVU. For more information, please contact [researchrepository@mail.wvu.edu](mailto:researchrepository@mail.wvu.edu).

---

# Characterization and Coherent Spin Selective Manipulation of Quantum Dot Energy Levels

---

Tristan Anthony Wilkinson

Dissertation submitted  
to the Eberly College of Arts and Sciences  
at West Virginia University  
in partial fulfillment of the requirements for the degree of  
Doctor of Philosophy in  
Physics



Edward Flagg, Ph.D., Chair  
Alan Bristow, Ph.D.  
Aldo Romero, Ph.D.  
Marcelo Davanco, Ph.D.

Department of Physics and Astronomy  
Morgantown, West Virginia  
2022

Keywords:  
Quantum Dots, AC Stark Effect, Coherent Control, Spectroscopy, Polarimetry

Copyright 2022 Tristan A. Wilkinson

# *Abstract*

## **Characterization and Coherent Spin Selective Manipulation of Quantum Dot Energy Levels**

Tristan Anthony Wilkinson

Semiconductor quantum dots (QDs) are promising candidates to fulfill a wide range of applications in real-world quantum computing, communication, and networks. Their excellent optical properties such as high brightness, single-photon purity, and narrow linewidths show potential utility in many areas. In order to realize long term goals of integration into complex and scalable quantum information systems, many current challenges must be overcome. One of these challenges is accomplishment of all necessary computing operations within a QD, which might be enabled by coherent manipulation of single QD energy level structures. In the realm of scalability for quantum devices, a way to address problems posed by the inhomogeneous distribution of individual QD spectral properties is necessary.

This dissertation presents record large AC Stark shifts applied to the energy level structure of a single semiconductor QD, as well as an automated spectroscopy method for efficient characterization of many QDs. The AC Stark shifts are spin-selective and fast, which are highly desirable qualities in a mechanism for energy level reconfiguration. The AC Stark shifts are measured by resonant excitation spectroscopy; a coherent technique which explicitly shows the change in energetic structure. A novel optical filtering scheme is developed to discriminate the high-powered laser inducing the shifts from the weak QD photoluminescence, and a polarimeter device is constructed to accurately measure the polarization state of a laser beam. Machine vision is used to automate spectroscopy of many QDs in bulk by acquiring high-resolution emission spectra, which allows characterization of individual QD energy level structures prior to device fabrication.

*To my parents, Meg and Tony, who always emphasized  
and supported my education and learning.*



## *Acknowledgements*

I owe an incalculable debt of gratitude to my advisor, Ned Flagg, who agreed to hire me as an RA for the summer after only a single 15 minute meeting. My time as a graduate student has been shaped more than anything by your patient and tireless commitment to always help me understand that which I struggle with, guide me through experimental problems, and provide honest advice about whatever I may ask. Working with you for the last 5 years has truly been a joy, and knowing that I have always had an understanding and compassionate advisor helped immeasurably in managing the inevitable stress and hard times of graduate school.

I must also acknowledge my de facto second advisor, Marcelo Davanco, at the National Institute of Standards and Technology. Designing and implementing a program using your incredible wealth of laboratory resources was some of the most fun I have ever had. Thank you for the freedom to mess around and develop the code as I saw fit. Also thank you to Ashish for spending many hours aligning the optics for my work, and for escorting me off campus after 7:00pm many times. Thank you to Glenn Solomon for letting me borrow your Sacher laser to perform the AC Stark shift measurements.

Thank you to Disheng for patiently teaching me the operation of almost the entire lab in only a few months time.

Thank you to my parents for your love and support, and for raising me to think like a scientist.

Finally, thank you to all of the many friends who have helped me through these 5 long years. Thank you Dustin for being a great roommate, and teaching me how to achieve a reasonable work-life balance in grad school. Thank you to Matt for encouraging me to learn guitar and being an excellent teacher, and even better friend. Thank you to the Geneseo folk for taking my mind off of grad school at my cabin every few months.

Lastly, I wish to thank George Marcus, and the Geneseo physics department as a whole, for preparing me so remarkably well for graduate school. This dissertation would not have been possible without the indestructible foundation of learning and knowledge forged in your department. For this I will always be grateful.

# Contents

<b>Abstract</b>	<b>ii</b>
<b>Acknowledgements</b>	<b>iv</b>
<b>1 Introduction</b>	<b>1</b>
<b>2 Background Information</b>	<b>7</b>
2.1 Quantum Dots: Artificial Atoms . . . . .	7
2.1.1 Concept and Growth . . . . .	7
2.1.2 Optical Properties and Charge States . . . . .	11
2.1.3 Control of Charge States with Diode Structure . . . . .	14
2.2 The Stokes Vector and the Poincaré Sphere . . . . .	17
2.3 The AC Stark Effect . . . . .	23
<b>3 Experimental Techniques and Setup</b>	<b>31</b>
3.1 Semiconductor Quantum Optics Laboratory (SQUOL) at WVU . . . . .	32
3.2 Automated Quantum Dot Spectroscopy at NIST . . . . .	42
<b>4 Polarimetry</b>	<b>51</b>
4.1 Motivation . . . . .	51
4.2 Operating Theory . . . . .	53
4.3 Device Description . . . . .	55
4.4 Discussion . . . . .	57
4.5 Conclusions . . . . .	60
<b>5 Spin-selective AC Stark shifts on Charged Quantum Dots</b>	<b>61</b>
5.1 Motivation . . . . .	61
5.2 Background and Theory . . . . .	63
5.3 Results and Discussion . . . . .	64
5.3.1 Excitation Spectra . . . . .	64

5.3.2	Red- and Blue-Detunings . . . . .	65
5.3.3	Dynamic Nuclear Polarization . . . . .	66
5.3.4	Spin-Selective Polarization Control . . . . .	68
5.3.5	Low-Power AC Stark Regime . . . . .	69
5.3.6	Linewidth Analysis . . . . .	71
5.4	Conclusions . . . . .	73
<b>6</b>	<b>Summary and Outlook</b>	<b>75</b>
<b>A</b>	<b>Automatic Focusing of Imaging System</b>	<b>77</b>
<b>B</b>	<b>Calibration of Liquid Crystal Variable Retarders (LCVRs)</b>	<b>79</b>
<b>C</b>	<b>Calibrating the Azimuth of an Optic to a Rotation Mount</b>	<b>83</b>
<b>D</b>	<b>Polarimeter Device Construction</b>	<b>85</b>
D.1	Drawings of Mechanical System . . . . .	85
D.2	Calibrating the Polarimeter . . . . .	92
D.3	Circuit Diagram and Printed Circuit Board (PCB) . . . . .	93
D.4	Arduino Code . . . . .	94
	<b>Bibliography</b>	<b>103</b>

# List of Figures

2.1	QD growth via molecular beam epitaxy . . . . .	8
2.2	Sample schematic . . . . .	10
2.3	InGaAs QD band structure . . . . .	11
2.4	Neutral QD $X^0$ energy level structure . . . . .	12
2.5	Negatively charged QD $X^-$ energy level structure . . . . .	13
2.6	Negatively charged QD $X^-$ in a magnetic field . . . . .	14
2.7	Diode sample band structure . . . . .	15
2.8	The polarization ellipse . . . . .	19
2.9	The Poincaré sphere . . . . .	21
2.10	Rate equations for a resonantly excited two-level quantum system	26
2.11	Dressed states picture . . . . .	28
2.12	AC Stark shifts of a two-level quantum system . . . . .	29
3.1	Resonant photoluminescence excitation (RPLE) concept . . . . .	32
3.2	Bias voltage map . . . . .	34
3.3	Excitation spectra bias dependence . . . . .	34
3.4	Waveguide excitation geometry . . . . .	35
3.5	Volume Bragg grating (VBG) operating principle . . . . .	36
3.6	QD PL overlain with VBG transmission . . . . .	36
3.7	VBG transmission angular dependence . . . . .	37
3.8	Experimental setup for AC Stark measurements . . . . .	38
3.9	Sample reflection spectrum . . . . .	40
3.10	NIST experimental imaging and spectroscopy setup . . . . .	43
3.11	Traveling salesman genetic algorithm . . . . .	44
3.12	Machine vision QD tracking method . . . . .	45
3.13	Fabry-Perot emission spectrum methodology . . . . .	47
3.14	Emission spectra from QDs in bulk . . . . .	48
3.15	Virtually imaged phased array (VIPA) . . . . .	49

4.1	Measurement head of the polarimeter . . . . .	54
4.2	Quarter-wave plate retardance measurements . . . . .	57
4.3	Polarimeter polarization measurements . . . . .	58
4.4	Polarimeter accuracy evaluation . . . . .	59
5.1	AC Stark effect on negatively charged dot $X^-$ . . . . .	63
5.2	Excitation spectra showing AC Stark shifts . . . . .	65
5.3	AC Stark frequency shifts for red- and blue-detunings . . . . .	66
5.4	Dynamic nuclear polarization . . . . .	67
5.5	Control of QD energy level structure . . . . .	69
5.6	Low-power AC Stark shifts . . . . .	70
5.7	QD excitation spectra linewidth analysis . . . . .	71
5.8	Nuclear spin bath polarization . . . . .	73
A.1	Automatic focusing of image system methodology . . . . .	78
B.1	Optical setup for LCVR calibration using the polarimeter . . . . .	79
B.2	Longitude and elevation angle intensity plots . . . . .	81
B.3	LCVR calibration maps . . . . .	82

# List of Tables

B.1	Poincaré sphere angles for 6 polarizations . . . . .	80
-----	--	----



# Chapter 1

## Introduction

Deeply rooted in the foundations of physics is the idea that the search for knowledge we embark on be both for the sake of understanding, and that this deep, elemental knowledge be applied to build technologies that might serve to improve human quality of life. From medical physics to civil engineering and to computing and communication we see this idea at play; all of these fields are built upon fundamental understanding of the underlying physics. For almost a century, classically based computation and communication has been expanding to the point where humans have constructed a globally interconnected network through which information can be sent from one continent to another in mere seconds. This extensive expansion has been enabled by the advent of classically based communication and computation, where information is sent as photons through fiber optic cables and transistors are used to implement binary logic, respectively. The proliferation of classical communication relies on key elements of technology: the laser<sup>1</sup>, and computation implemented by the transistor. The design and engineering of both of these devices rely on the understanding of quantum mechanics. As such, these technologies are often referred to as belonging to the first "quantum revolution". We now stand on the cusp of a second "quantum revolution" where quantum communication and computation leading to large-scale quantum networks may significantly change the world we live in. While the development of classical computing is underpinned by our understanding of quantum mechanics, all current information processing occurring in cellphones, laptops, etc. relies solely on classical notions of information processing. Quantum computation algorithms, in contrast, will run on machines where the laws of quantum mechanics are directly connected to the processing of information. This difference has the potential to enable the construction of

---

<sup>1</sup>An acronym for light amplification by stimulated emission of radiation.



quantum computers which are more powerful than their classical counterparts<sup>2</sup>. Similarly, quantum communication and networks may well realize applications and protocols with benefits that we cannot yet imagine at present day.

Several quantum platforms with potential to help realize real world quantum network goals are currently being worked on around the globe [1]. These include superconducting circuits, cold ion traps, vacancy centers in diamond, and semiconductor quantum dots (QDs), among others. Each of these provides unique advantages and pose their own set of challenges in experimental implementation [2, 3]. It is reasonably likely that any realization of a large scale quantum network will incorporate attributes and methods developed or designed in multiple platforms to maximize functionality, efficiency, and robustness [4, 5]. Thus, work continues on potential applications and protocols for all of these platforms.

Many different kinds of semiconductor QDs have been designed and fabricated for quantum information and other applications. Some examples include the monolayer thickness fluctuations in a GaAs quantum-well [6, 7], CdSe colloidal QDs synthesized in a chemical solution [8], electrostatically defined QDs in a two-dimensional electron gas [9], and epitaxially-grown self-assembled QDs [10–12], such as InGaAs QDs. These self-assembled QDs possess several desirable properties relevant to quantum applications. Grown via the well-developed method of molecular beam epitaxy (MBE) [13] these dots have an excellent means for incorporation into complex photonic and electrical device structures. Additionally they have a large carrier confinement, tailorable ensemble dot size [14, 15], and a designable composition. These attributes make self-assembled QDs appealing not only to quantum computing, communication, and network endeavors, but also the large solid-state industry with devices such as electrically pumped QD lasers [16] and infrared single photon detectors [17, 18] already in large-scale production.

A point of extremely high attractiveness are the excellent optical properties of self-assembled semiconductor QDs, excelling as a source of single photons, with

---

<sup>2</sup>Since classical physics is simply a limiting case of quantum mechanics, it follows that quantum computation is *at least* as powerful as classical computation. Notably, according to the Church-Turing thesis, any computation that can be performed on a quantum computer can also be performed on a classical one. However, the quantum computation may require a fewer number of elementary steps, which leads to a speedup in computation time.

achievements in high brightness [19–25], indistinguishably [24–30], and single-photon purity [23, 30–37] being made over the past three decades. These properties have been shown to enable applications in quantum computation [38–46] and quantum key distribution [47–49]. The strong emission properties of self-assembled semiconductor quantum dots make them an excellent candidates for spin-photon interfaces in quantum networks [30, 31, 38, 50, 51], while drawbacks include their short spin coherence time [38, 52] and inhomogeneous distribution of individual dot properties due to the stochastic nature of the growth process [10, 53–56].

This dissertation concerns the characterization and coherent manipulation of the energy level structure of single self-assembled InGaAs QDs grown by MBE. Measurements are performed in two different laboratories: the Semiconductor Quantum Optics Lab (SQUOL) at West Virginia University (WVU), and the Davanco lab housed at the National Institute of Standards and Technology (NIST) in Gaithersburg, MD. This lab is part of the Single Emitters Group in the Physical Measurement Lab. In the WVU lab, a novel optical filtering scheme is developed and implemented to produce record large AC Stark shifts. These shifts are spin-selective, reversible, and can be applied or removed rapidly<sup>3</sup>. Additionally a polarimeter device to measure the polarization state of a laser beam is constructed. In the Davanco lab at NIST, a method for automated spectroscopy of QDs is developed with the goal of yielding a high throughput method of QD characterization. In principle, this automation will enable more efficient device fabrication.

The lab work at NIST centers around improving the efficiency with which spectroscopic measurements can be performed on individual QDs, to enable high throughput fabrication of devices. The inhomogeneous distribution of self-assembled QD properties due to the stochastic nature of the growth process [10, 53–56] generally necessitates that individual QD characterization be done manually prior to device fabrication, or that many devices be fabricated with the hope of finding a desirable dot positioned at the correct location within a device. In the Davanco lab at NIST, a program is developed to automate the spectroscopy process using machine vision and a combination of a scanning Fabry-Perot cavity and a spectrometer to record high-resolution emission spectra. The signal

---

<sup>3</sup>In this context rapidly means faster than the spin coherence time of a single trapped electron within the dot, which is on the order of microseconds [38]. Comparatively, electro-optic modulators can enable the cycling of a laser on the order of nanoseconds.

to noise ratio (SNR) of the acquired emission spectra are poor due to the low transmission efficiency of the Fabry-Perot. However, the method shows a proof of principle for automatic acquisition of emission spectra.

The control and measurement of the polarization state of photons is of central importance to quantum communication and computation, because the information encoded in the spin of an electron or hole is transferred into the photon polarization state [38]. To enable precise manipulation of the polarization state of a laser beam in experiment, a rotating waveplate polarimeter device is constructed. The device is characterized and shown to have accuracy comparable to commercially available devices. This device allows calibration of optical elements in order that the polarization of photons be matched to specific dipole transitions of the QDs, i.e. the spin of trapped electrons.

Record large AC Stark shifts in a charged QD are achieved and measured in the SQUOL lab at WVU. An outstanding problem in using self-assembled semiconductor QDs for quantum computation is the inability to perform the three necessary operations for computation [57]: initialization, manipulation, and single-shot readout of a trapped electron spin in the QD under a single geometry of magnetic field. Both initialization [58], and manipulation [42, 59] have been shown to work under a small transverse applied magnetic field, while single-shot readout remains a challenge due to the possibility of a spin flip. In principle, the spin-selective AC Stark shifts demonstrated in the WVU lab will allow for single-shot readout to be achieved under this geometry of applied magnetic field [60]. This will enable further applications of self-assembled QDs for quantum computation and communication.

This chapter has been an introduction to the general motivation for the use of self-assembled semiconductor QDs in quantum communication, computation, and networks, and contains a summary of the measurements done in this dissertation. Chapter 2 provides an overview of QDs including their optical properties and charge states, review of the Stokes vector formalism for polarized light, and a derivation of the dynamics of the AC Stark effect on a two-level quantum system. Chapter 3 describes the two experimental setups and the techniques used to conduct measurements at WVU and NIST, additionally discussing some results from the NIST work. Chapter 4 details the design, construction, and evaluation of the polarimeter device used for polarization control and measurement. Chapter 5 describes the production and measurement

of record large spin-selective AC Stark shifts in self-assembled semiconductor QDs, along with a discussion of some of the dynamics observed. Chapter 6 outlines some brief conclusions and future directions for the vein of this research on QDs and their potential applications to quantum computing, communication, and networks.



## Chapter 2

# Background Information

This chapter provides background on three topics central to the experiments and results presented in this dissertation. First a general background on self-assembled InGaAs quantum dots (QDs) including their growth, band structure, and the properties and optical selection rules of two relevant charge states. The second section details the theoretical formalism of polarized light with description of the polarization ellipse, Stokes vector, and the Poincaré sphere. Third is a derivation of the dynamics of the AC Stark effect on a two-level quantum system from first principles. Together, these elements serve to support the results and discussion presented in the later chapters.

## 2.1 Quantum Dots: Artificial Atoms

### 2.1.1 Concept and Growth

Quantum dots (QDs) are often referred to as *artificial atoms* due to their atom-like emission and absorption properties. At the most basic level QDs are nanometer sized multidimensional quantum wells. When the size of the QD/quantum potential well is comparable to the de Broglie wavelength of an electron, a hole, or their combination an exciton, the system enters the strong confinement regime and this results in atom-like discrete energy levels. Thus, QDs can be thought of as charge traps that act to localize the wave functions of electrons, holes, and excitons.

There are several different types of QDs, each having their own advantages and disadvantages. Some examples include: electrostatically defined QDs [9, 61, 62], colloidal QDs [8], QDs formed by cleaved edge overgrowth [63], and lithographically defined QDs [64]. The entirety of the experiments discussed

in this work are performed on self-assembled InGaAs QDs grown via molecular beam epitaxy (MBE) in the Stranski-Krastanov (S-K) mode of heteroepitaxial growth or layer-plus-island mode [10, 53–56]. In this growth method, a layer of a small band gap material, for example InAs, is grown on top of a substrate of a large band gap material, for example GaAs (Fig. 2.1(a-b)). This method relies on the concept of epitaxy, where deposited atoms form a crystalline structure to match that of the underlying substrate. When the lattice constant of the atoms being deposited does not match that of the substrate, this epitaxial growth cannot continue and one consequence is the formation of island structures. For the InAs on GaAs system the larger atom of InAs is compressed to accommodate the smaller lattice constant of the GaAs<sup>1</sup>. This compression of the InAs introduces extra elastic energy into the system, and at some critical level of thickness of the InAs, the formation of islands becomes energetically favorable and thereby a QD is formed (Fig. 2.1(c)) [55, 65, 66]. Full three-dimensional confinement is achieved by capping the exposed islands with additional layers of large band gap material GaAs (Fig. 2.1(d)). Thus an InGaAs (InAs embedded in GaAs) QD is formed. Fig. 2.1 shows an outline of the process of this growth method. Note that growing InAs on GaAs will inevitably lead to some alloying of GaAs in the InAs, such that the actual QD is something like  $\text{In}_{0.9}\text{Ga}_{0.1}\text{As}$ , as shown in Fig. 2.1. Note these two nomenclatures are used somewhat interchangeably to refer to InAs on GaAs dots.

In all types of QDs the specifics of the confinement and energy structure are

<sup>1</sup>In this case the lattice constant of GaAs is about 7% smaller than that of InAs.

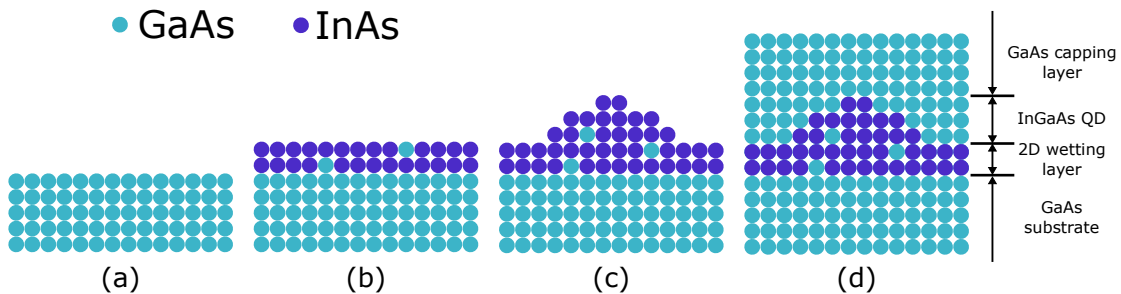


FIGURE 2.1: Molecular beam epitaxy in the Stranski-Krastanov growth mode for InGaAs QDs. A GaAs substrate is grown (a), layers of InAs are grown on top (b) until island are formed (c), and lastly the dot is capped with GaAs (d) for full three-dimensional confinement.

determined by the properties of each individual QD, namely the geometry of the structure and the depth of the potential well. The depth of the potential well is determined by the relative band gap of the materials. Due to the stochastic nature of the formation of islands in MBE growth [10, 53–56], the size, position, and location of the QDs cannot generally be controlled. Careful control of the growth parameters can result in a reduction in the distribution of these properties [14, 15], but regardless for any individual dot they will be random and unknown until spectroscopy is performed. This inhomogeneity problem is the central motivation for the automated spectroscopy work done at the National Institute of Standards and Technology (NIST) discussed in Sec. 3.2.

QDs grown in bulk emit freely in all directions as dipole sources. Unfortunately, the majority of the emitted photons will be subject to total internal reflection at the GaAs/air interface<sup>2</sup>, and thus most of the light cannot be collected by external optics. This means that the efficiency of light extraction from an individual QD to free space (air) outside of the sample is very low. This efficiency is approximately given by the relation  $\kappa_{bulk} \sim \frac{1}{4n^2}$ , which is of the order of only 2% for  $n_{GaAs@930nm}$  [67]. Therefore it is common practice to grow structures surrounding the QD layer to enhance the extraction efficiency [68]. Techniques include micropillar cavities [24, 69–72], photonic crystal cavities [73], planar distributed Bragg reflector (DBR) cavities [67, 74], along with several other engineered photonic structures [75, 76]. The automated spectroscopy work at NIST deals with QDs in bulk (Sec. 3.2), while the work at WVU deals with QDs in a planar DBR cavity (Chapter 5). Figure 2.2 shows a schematic of the WVU sample including the planar DBR cavity, and the diode structure for charge control discussed later on in this section (Sec. 2.1.3). The planar DBR is constructed by the growth of two AlGaAs/GaAs DBRs, one above and one below the QD layer. Each DBR is grown in a superlattice structure where each individual alternating sublayer of AlAs and GaAs is designed to have thickness  $\lambda_0/4n_{AlAs}$  and  $\lambda_0/4n_{GaAs}$ , respectively. The wavelength  $\lambda_0$  is chosen to be at the center of the QD distribution. The lower (upper) DBR has more (less) DBR layers leading to a larger (smaller) reflectance. In the sample used for experiments in this dissertation, the top DBR has 4-periods and the lower has 10-periods. This allows an increase in the extraction efficiency compared to the 2% of bulk GaAs, and has

---

<sup>2</sup>GaAs has a relatively large index of refraction at QD emission wavelengths  $n_{GaAs@930nm} \approx 3.55$ .



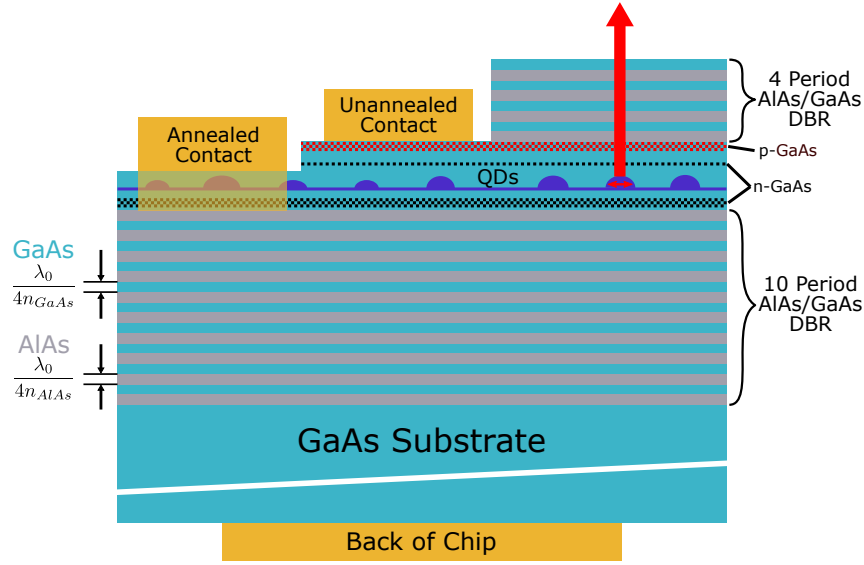


FIGURE 2.2: Sample schematic including the planer DBR cavity and diode structure. The planar DBR cavity increases the collection efficiency of photons emitted from the QDs to external collection optics. The sample is etched to two different depths creating three separate regions, allowing ohmic contact to the doped regions forming the diode structure, and application of a bias voltage to the QD layer.

been estimated to be 6% for a sample with a similar planar cavity structure [77].

As outlined above, the strong confinement regime occurs when the de Broglie wavelength of a free charge carrier is comparable to the quantum potential well dimensions of the QD. For a free charge carrier in bulk semiconductor the de Broglie wavelength is on the order of  $\lambda = 2\pi\hbar/\sqrt{2m^*E}$ , where  $m^*$  is the effective mass of the charge carrier, and  $E \approx \frac{3}{2}k_B T$  is the kinetic energy. Computing several wavelengths at 4 K<sup>3</sup>, an electron in the conduction band of GaAs (InAs) is on the order of 340 (200) nm, and a heavy hole in the valence band is on the order of 80 (70) nm. Comparatively, the confinement potential is  $\sim 20$  nm in the lateral plane of the QD, and  $\sim 5$  nm in the vertical direction. Therefore, both electron and hole interact with the QD in the strong confinement regime, which results in the atom-like discrete energy structure as shown in Fig. 2.3. The number of these discrete energy levels depends on the dimensions of the potential well. The depth of the well is almost entirely determined by the relative band gaps of the materials of choice. In this case, GaAs has a band gap of  $\sim 1.51$  eV

<sup>3</sup>The temperature to which our samples are cooled for measurements.

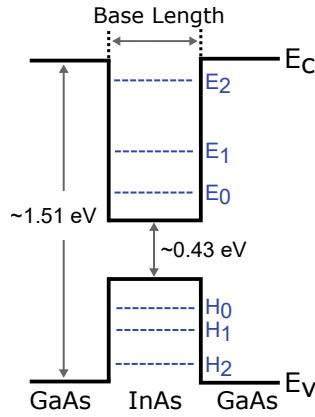


FIGURE 2.3: Band structure for an InGaAs QD. InAs, the smaller band gap material ( $\sim 0.43$  eV), is embedded in GaAs having a comparatively larger band gap ( $\sim 1.51$  eV). This results in a potential well having atom-like discrete energy states.

and InAs has  $\sim 0.43$  eV, which fixes the depth of the well. Conversely, the base length (width) of the QD is somewhat random owing to the stochastic nature of growth [10, 53–56]. Calculations by Schliwa et al. [78] show that the number of electron bound states can range from 3–12 for a 10–20 nm base length, while the hole bound states range from 5–12 over the same size range. For simplicity, I have included three bound states for electron and hole each in Fig. 2.3 and the following band diagram figures.

### 2.1.2 Optical Properties and Charge States

The optical properties of QDs are mostly determined by the electrons and holes in the lowest energy states, i.e.  $E_0$  and  $H_0$  in Fig. 2.3. Charge carriers in higher energy levels cannot efficiently recombine due to fast non-radiative decay processes ( $\sim 1$ –10 ps), such as phonon emission [79]. Charges in these higher levels will thus first decay to a lower energy state before recombining radiatively or otherwise<sup>4</sup>. Different combinations of trapped electron and holes in these lowest energy states lead to different ground and excited states connected by optically active transitions, and thus various charge states are formed [83, 84]. Due to

<sup>4</sup>One example of non-radiative recombination is Auger recombination, in which the electron-hole recombination energy is transferred to another charge carrier [80–82].

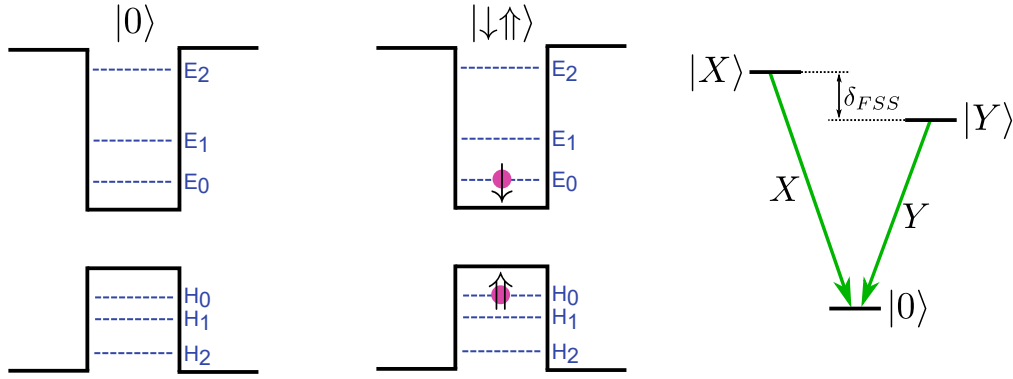


FIGURE 2.4: Neutral QD charge state  $X^0$ . The band diagrams for the ground and one excited state are shown on the left, and the energy level diagram is shown at the right.

their different energy levels, here we ignore light holes and consider only heavy holes<sup>5</sup>.

Two charge states of InGaAs QDs are relevant to this dissertation, specifically the neutral dot and the negatively charged dot. Figure 2.4 shows band diagrams and the energy level diagram for a neutral dot, which is often denoted by  $X^0$ . The ground state is a dot empty of charges labeled as  $|0\rangle$ , and the two excited states are exciton states labeled  $|\uparrow\downarrow\rangle$  and  $|\downarrow\uparrow\rangle$ . Only one of the exciton band diagrams is shown in Fig. 2.4 as the other is equivalent, with the spin of the electron and hole flipped. The ground state has spin angular momentum  $S = 0$  and the excited exciton states have  $S = 1$ , thus these pure states are connected by optically active transitions with the emitted photons being circularly polarized  $\sigma_{\pm}$  corresponding to  $m_s = \pm 1$ . However, this only holds true if the QD is circularly symmetric. During growth InGaAs QDs are commonly<sup>6</sup> elongated along the  $[110]$  or  $[\bar{1}10]$  crystallographic directions [85–89]. Thus, the symmetry is broken leading to mixing of the states, non-degenerate excited states, and linear polarization of the transitions. The new states  $|X\rangle$  and  $|Y\rangle$ <sup>7</sup> are simply a reformulation of the states into a new basis, explicitly  $|X\rangle = \frac{1}{\sqrt{2}}(|\downarrow\uparrow\rangle + |\uparrow\downarrow\rangle)$  and  $|Y\rangle = \frac{1}{\sqrt{2}}(|\downarrow\uparrow\rangle - |\uparrow\downarrow\rangle)$ . The energy splitting of the excited states induced

<sup>5</sup>The light hole states have far higher ground state energy than that of heavy holes due to their smaller effective mass (consider the ground state energy of an infinite potential well  $E \sim \frac{1}{mL^2}$ ). As stated, only the lowest few energy states of the potential well determine the optical properties, and therefore we ignore light holes.

<sup>6</sup>This is almost always the case, and it is a rarity to find a circularly symmetric dot.

<sup>7</sup>These states are also commonly labeled  $|\uparrow\downarrow\rangle_x$  and  $|\downarrow\uparrow\rangle_y$ , respectively. I have chosen just  $|X\rangle$  and  $|Y\rangle$  for simplicity.

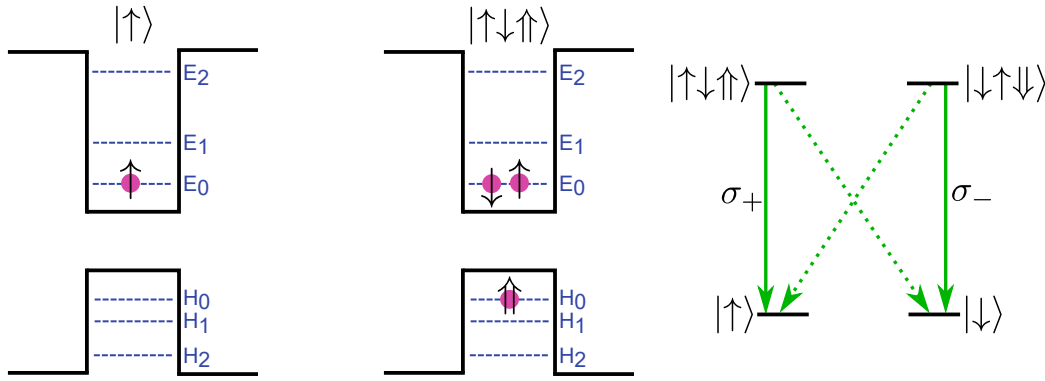


FIGURE 2.5: Negatively charged QD charge state  $X^-$ . The band diagrams for one ground and one excited state are shown on the left, and the energy level diagram is shown at the right. Solid (dashed) lines indicate dipole allowed (forbidden) transitions.

by this geometrical asymmetry  $\delta_{FSS}$  is referred to as fine structure splitting (FSS), as shown in Fig. 2.4 [83, 84, 90–94].

Figure 2.5 shows band diagrams and the energy level diagram for a negatively charged dot  $X^-$ . The ground states are a single electron trapped in the dot<sup>8</sup>, which has spin  $S = \frac{1}{2}$  and thus  $m_S = \pm\frac{1}{2}$ . The excited states once again are the ground state with the addition of an exciton<sup>9</sup>. Explicitly these excited states are an electron singlet and a heavy hole;  $|\uparrow\downarrow\uparrow\rangle$  and  $|\downarrow\uparrow\downarrow\rangle$  having spin  $S = \frac{3}{2}$  and  $m_S = \pm\frac{3}{2}$ , respectively. Thus the ground and excited states of each spin-manifold are connected by circularly polarized ( $\sigma_{\pm}$ ) optical transitions, and in no magnetic field the cross-transitions in between the spin-manifolds are dipole forbidden [83, 84]. This is indicated in Fig. 2.5 by the dashed arrows connecting the inter-manifold states.

The energy levels of a quantum system can be shifted via the Zeeman effect by the application of an external magnetic field. The optical selection rules of the system will also change depending on the orientation of the magnetic field relative to the dipole moment(s) of transition. Figure 2.6 shows the energy level diagrams of a negatively charged dot  $X^-$  in two geometries of external magnetic field. A magnetic field applied along the growth direction of the sample is

<sup>8</sup>The name "negatively charged" comes from the negative charge of the electron in this ground state.

<sup>9</sup>These excited states are made up of three charged particles, and thus termed a trion. Colloquially the overall charge state may be referred to as negatively charged, or a trion. However, to be explicitly clear the overall charge state is "a negatively charged dot", and the term trion refers only to the excited states composed of three charged particles.

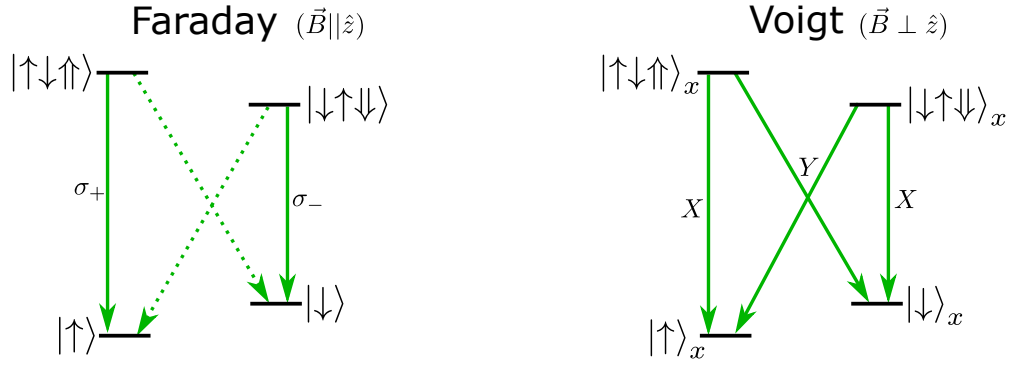


FIGURE 2.6: Negatively charged QD charge state  $X^-$  in two geometries of applied magnetic field. In the Faraday configuration on the left the magnetic field is applied along the growth direction of the sample, while in the Voigt configuration on the right the field is applied in the plane of the sample.

referred to as the Faraday configuration [83] and is shown on the left of Fig. 2.6. A magnetic field applied in the plane of the sample is called the Voigt configuration [83] and is shown on the right of Fig. 2.6. In the Faraday configuration degenerate eigenstates of the ground and excited states split via Zeeman splitting, while the optical selection rules remain the same as in no magnetic field, i.e. the cross-transitions between spin-manifolds are still dipole forbidden. The in-plane magnetic field in the Voigt configuration mixes the z-direction eigenstates and thus the states are treated as in-plane (x/y-directional) eigenstates. This is similar to the change of basis for the neutral dot excited states (Fig. 2.4) induced by the QD geometrical asymmetry. Explicitly we have that  $|\uparrow\rangle_x = \frac{1}{\sqrt{2}}(|\uparrow\rangle + |\downarrow\rangle)$  and  $|\downarrow\rangle_x = \frac{1}{\sqrt{2}}(|\uparrow\rangle - |\downarrow\rangle)$  for the ground states, and  $|\uparrow\downarrow\uparrow\rangle_x = \frac{1}{\sqrt{2}}(|\uparrow\downarrow\uparrow\rangle + |\downarrow\uparrow\downarrow\rangle)$  and  $|\downarrow\uparrow\downarrow\rangle_x = \frac{1}{\sqrt{2}}(|\uparrow\downarrow\uparrow\rangle - |\downarrow\uparrow\downarrow\rangle)$  for the excited states, as labeled in Fig. 2.6. The eigenstates are also Zeeman split in the Voigt configuration, and additionally the optical selection rules are changed due to the mixing of the states by the in-plane magnetic field. Namely, the cross-transitions between spin-manifolds are now dipole allowed and equally as probable as the intra-manifold transitions, and all transitions become linearly polarized [83, 84].

### 2.1.3 Control of Charge States with Diode Structure

In general, the charge state of an individual QD is somewhat randomly determined by the environment surrounding the dot [95]. For example, a local charge

trap near the dot might serve to shield the dot from free charges, and thus increase the likelihood of the dot being in the neutral charge state [96]. Additionally, the application of a low-power above-band-gap laser to the environment will increase the availability of free charge carriers [97, 98]. These charge carriers can serve to neutralize a charged dot, or charge a neutral dot [99]. The QD must be held stable in a single charge state while quantum computing or information protocols are performed. Therefore, this random and poorly understood mechanism of QD charging and neutralization poses a roadblock in the desire to use the energy level configuration of a single QD charge state as a platform for quantum computing and information applications. Thus, the ability to predictably control the charge state of individual dots is desirable.

To achieve control of the charge state of a dot, a diode system can be constructed during sample growth to surround the layer of QDs [100–102]. Figure 2.7(a) shows a simplified schematic of our diode sample structure used for

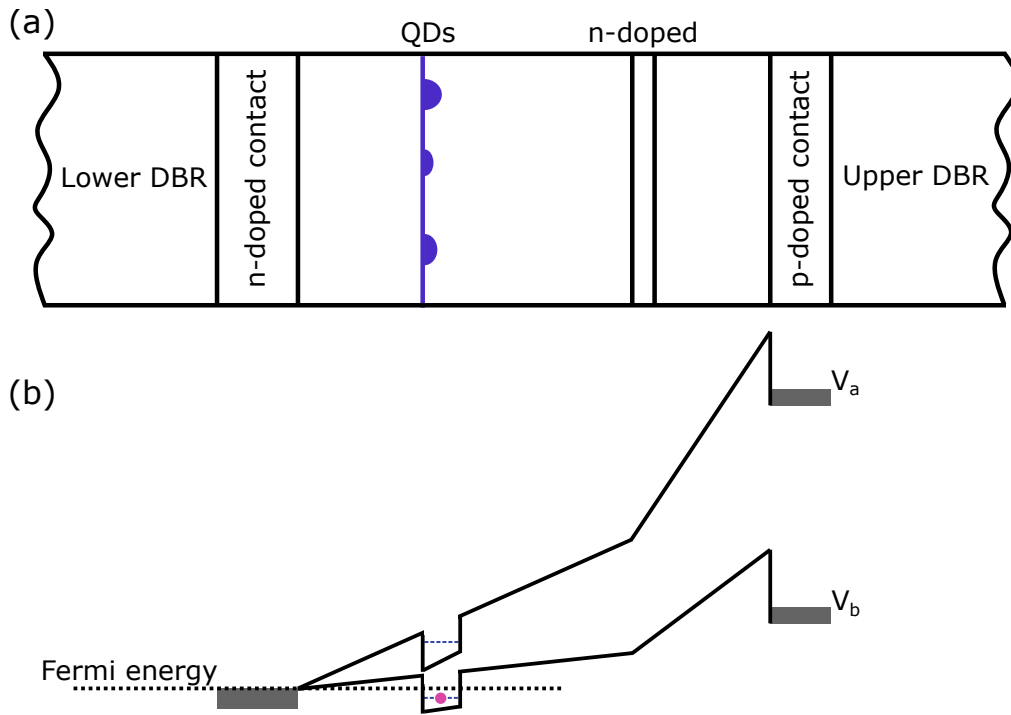


FIGURE 2.7: Diode sample structure design (a), and band diagram at two distinct bias voltages (b). Changing the bias voltage controls the relation of the QD energy levels to the Fermi energy, which in turn controls the stable charge state of the QD.

charge state control<sup>10</sup>. The three doped GaAs regions form a p-i-n-i-n diode structure [103] surrounding the QD, and ohmic contact is made to the p-doped and lower n-doped regions. Figure 2.7(b) shows the band diagram of the diode structure at two distinct bias voltages. Note the intermediate n-doped region in the diode structure causes band bending, reducing the potential between the QDs and back gate. This allows QDs to be charged at relatively low bias voltages as compared to those in a p-i-n diode [103]. Changing the bias voltage between the two electrodes bends the bands, which allows for the QD energy levels to be dipped below the Fermi energy. In this way, the tunneling coefficient of an electron from the Fermi sea into the dot can be changed, which in turn controls the stable charge state of the dot. For example, at bias voltage  $V_a$  in Fig. 2.7(b) the lowest QD energy level is well above the Fermi energy and thus the dot will be neutral (Fig 2.4). Comparatively, at  $V_b$  the QD energies have been dipped below the Fermi energy and the dot will be charged with one (Fig. 2.5) or more electrons. A photoluminescence intensity plot of light emitted from many dots under HeNe excitation as a function of bias voltage is shown in the next Chapter in Fig. 3.2. This figure shows how the stable charge state is controlled by the applied voltage.

---

<sup>10</sup>This figure is zoomed in on the diode structure around the QD layer in Fig. 2.2 to explicitly show the band behavior and outline the functionality.

## 2.2 The Stokes Vector and the Poincaré Sphere

In 1852 George Gabriel Stokes defined the Stokes vector  $\mathbf{S} = [S_0, S_1, S_2, S_3]$ , which characterizes the polarization state of light with four intensity parameters  $S_{0-3}$  [104]. This Stokes vector formalism is commonly used to describe the polarization of an optical (laser) beam [105] because the polarization ellipse, which is an amplitude description of polarized light, is not directly accessible to measurement [106]. The convenience and appeal of the Stokes vector is that its component parameters ( $S_{0-3}$ ) are directly related to the polarization ellipse and its associated orientation ( $\psi$ ) and ellipticity ( $\chi$ ) angles [104, 105, 107]. The Stokes vector formalism provides a natural framework for description of the design concept and operating theory of the polarimeter device described in Chapter 4. Thus, included here is a brief introduction to the Stokes vector, a description of its component parameters, and their relation to the polarization ellipse and Poincaré sphere.

In the simplest treatment we can formulate light as a propagating electric field composed of monochromatic plane waves. In general terms, polarization arises when there are two orthogonal oscillating components of the electric field with different amplitudes and phases<sup>11</sup>. We can select the orthogonal components to lie in the x- and y-planes, such that the wave propagates in the z-direction as

$$\vec{E}(z, t) = E_x(z, t)\hat{x} + E_y(z, t)\hat{y}, \quad (2.1)$$

where  $E_x(z, t)$  describes the electric field along the x axis, and  $E_y(z, t)$  the y axis. The equations of the components of the field can be written as

$$E_x(z, t) = E_{0x} \cos(kz - \omega t), \quad (2.2a)$$

$$E_y(z, t) = E_{0y} \cos(kz - \omega t + \eta), \quad (2.2b)$$

where  $t$  represents the time,  $E_{0x}$  and  $E_{0y}$  are the maximum amplitudes of the optical field in x and y, respectively,  $\omega = 2\pi\nu$  is the angular frequency,  $k = 2\pi/\lambda$  is the wave number, and  $\eta = \eta_y - \eta_x$  describes the phase difference between the two waves [107]. The term  $kz - \omega t$  describes the propagation of the wave through time and space, and is often referred to as the propagator [108]. At the

---

<sup>11</sup>Note that either of the amplitudes  $E_{0x}$  and  $E_{0y}$  could always be = 0, and thus linear polarization can arise from only a single non-zero field component.



frequencies of interest here (near-infrared) the period of oscillation of the field is  $\sim 10^{-15}$  s, which precludes any direct measurement.

For a formulation of the optical field that will allow measurement we search for one that depends on neither position nor time, i.e. eliminate the propagator from Eq. 2.2. First, we can isolate the propagator from the phase term in Eq. 2.2(b) with

$$\frac{E_y(z, t)}{E_{0y}} = \cos(kz - \omega t + \eta) = \cos(kz - \omega t) \cos \eta - \sin(kz - \omega t) \sin \eta. \quad (2.3)$$

Looking at this form, we can see that  $\sin(kz - \omega t)$  can be isolated by plugging in Eq. 2.2(a) for the  $\cos(kz - \omega t)$ , which yields

$$\frac{E_y(z, t)}{E_{0y}} - \frac{E_x(z, t)}{E_{0x}} \cos \eta = -\sin(kz - \omega t) \sin \eta. \quad (2.4)$$

Additionally Eq. 2.2(a) can be rewritten to read

$$\sin(kz - \omega t) = \sqrt{1 - \left( \frac{E_x(z, t)}{E_{0x}} \right)^2}. \quad (2.5)$$

And finally, combining Eqs. 2.4 and 2.5 and squaring both sides we arrive at

$$\left( \frac{E_x(z, t)}{E_{0x}} \right)^2 + \left( \frac{E_y(z, t)}{E_{0y}} \right)^2 - 2 \left( \frac{E_x(z, t)}{E_{0x}} \right) \left( \frac{E_y(z, t)}{E_{0y}} \right) \cos \eta = \sin^2 \eta, \quad (2.6)$$

which is known as the polarization ellipse because it provides a complete characterization of the polarization of a propagating plane wave (optical field) [107].

A diagram of the polarization ellipse is shown in Fig. 2.8. The orientation angle  $\psi$  describes the angle of the ellipse, and the ellipticity angle  $\chi$  describes the circularity of the ellipse<sup>12</sup>. At frequencies much lower (up to microwave) than those discussed in this dissertation (near-infrared), the polarization ellipse is traced out slowly enough by the electric field that the parameters  $E_{0x}$ ,  $E_{0y}$ , and  $\eta$  from Eq. 2.6 can be measured directly [109]. However, at the optical and near-infrared frequencies of interest here we must transform Eq. 2.6 into the intensity domain in order that measurement be performed [106]. Principally

<sup>12</sup>If  $\chi = 0$  the ellipse collapses to a line (linear polarization), and if  $\chi = \frac{\pi}{4}$  the ellipse is a perfect circle (circular polarization).

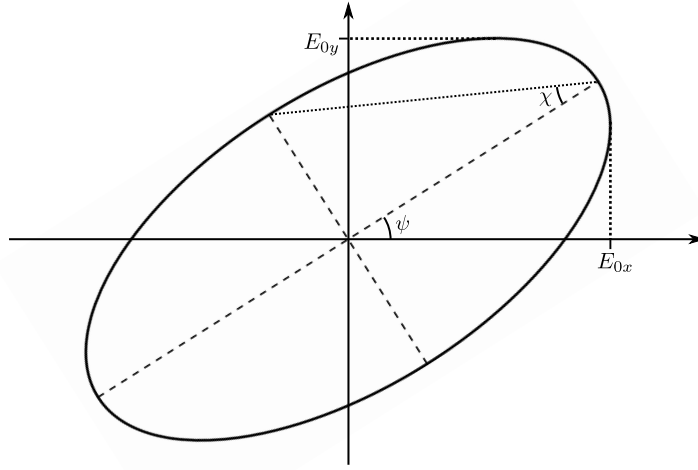


FIGURE 2.8: The polarization ellipse traced out by the electric field defined by Eq. 2.6.  $E_{0x}$  and  $E_{0y}$  are the amplitudes of the x and y components of the field, respectively.  $\psi$  is the orientation angle and  $\chi$  is the ellipticity angle.

this means taking a time average over an infinite time interval, however, due to the periodicity of  $E_x(z, t)$  and  $E_y(z, t)$  a time average over a single period  $T = 2\pi/\omega$  is sufficient [110]. This time average for the quadratic field components is defined by

$$\langle E_i(z, t)E_j(z, t) \rangle = \frac{1}{T} \int_0^T E_i(z, t)E_j(z, t)dt \quad (i, j = x, y). \quad (2.7)$$

Applying the time average and multiplying Eq. 2.6 by  $4E_{0x}^2E_{0y}^2$  yields

$$4E_{0y}^2\langle E_x(z, t)^2 \rangle + 4E_{0x}^2\langle E_y(z, t)^2 \rangle - 8E_{0x}E_{0y}\langle E_x(z, t)E_y(z, t) \rangle \cos \eta = (2E_{0x}E_{0y} \sin \eta)^2. \quad (2.8)$$

Using Eqs. 2.7 and 2.2 to calculate the time averages gives us

$$\langle E_x(z, t)^2 \rangle = \frac{E_{0x}^2}{2}, \quad (2.9a)$$

$$\langle E_y(z, t)^2 \rangle = \frac{E_{0y}^2}{2}, \quad (2.9b)$$

$$\langle E_x(z, t)E_y(z, t) \rangle = \frac{1}{2}E_{0x}E_{0y} \cos \eta. \quad (2.9c)$$

Next, substituting Eq. 2.9 into Eq. 2.8 results in

$$2E_{0x}^2 E_{0y}^2 + 2E_{0x}^2 E_{0y}^2 - (2E_{0x}E_{0y} \cos \eta)^2 = (2E_{0x}E_{0y} \sin \eta)^2. \quad (2.10)$$

Lastly, adding and subtracting the quantity  $(E_{0x}^4 + E_{0y}^4)$  to the left-hand side of Eq. 2.10 and rearranging we get

$$(E_{0x}^2 + E_{0y}^2)^2 = (E_{0x}^2 - E_{0y}^2)^2 + (2E_{0x}E_{0y} \cos \eta)^2 + (2E_{0x}E_{0y} \sin \eta)^2, \quad (2.11)$$

which can be rewritten as

$$S_0^2 = S_1^2 + S_2^2 + S_3^2, \quad (2.12)$$

with the definitions

$$S_0 = E_{0x}^2 + E_{0y}^2, \quad (2.13a)$$

$$S_1 = E_{0x}^2 - E_{0y}^2, \quad (2.13b)$$

$$S_2 = 2E_{0x}E_{0y} \cos \eta, \quad (2.13c)$$

$$S_3 = 2E_{0x}E_{0y} \sin \eta. \quad (2.13d)$$

The relations defined in Eq. 2.13 are the Stokes polarization parameters that make up the Stokes vector  $\mathbf{S} = [S_0, S_1, S_2, S_3]$  [104]. These parameters are defined in terms of intensities (amplitudes squared) in different orthogonal bases and can therefore be measured. The parameter  $S_0 = I_X + I_Y$  describes the total intensity of the optical field,  $S_1 = I_X - I_Y$  the preponderance of linearly horizontally (X) polarized light over linearly vertically (Y) polarized light,  $S_2 = I_D - I_A$  the preponderance of linearly diagonally (D or  $+45^\circ$ ) polarized light over linearly anti-diagonally (A or  $-45^\circ$ ) polarized light, and  $S_3 = I_R + I_L$  the preponderance of right circularly (R or  $\sigma_+$ ) polarized light over left circularly (L or  $\sigma_-$ ) polarized light, where  $I_\beta$  with  $\beta = \{X, Y, D, A, R, L\}$  represents the measured intensity of a given polarization [104]. In this way, the polarization state of the optical field is completely described and characterized by knowledge of the Stokes vector.

A useful and notable feature of the Stokes parameters ( $S_1, S_2, S_3$ ) is that they define a one-to-one correspondence between any state of polarization and a unique point on the surface of a sphere of radius  $S_0$  [109], as can be directly seen from Eq. 2.12. This sphere is known as the Poincaré sphere, and is shown in

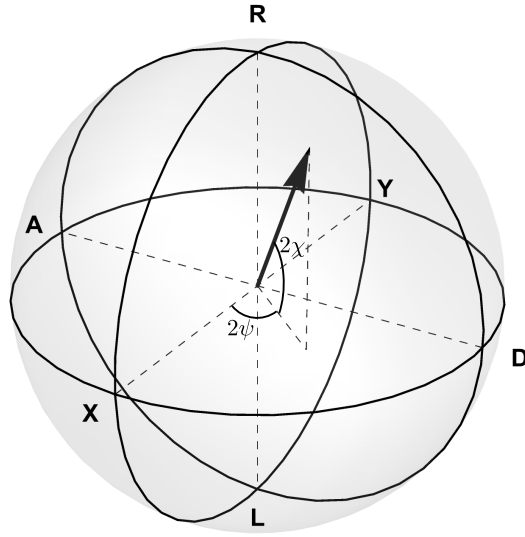


FIGURE 2.9: The Poincaré sphere, the surface of which has a one-to-one correspondence to any state of polarization described by the Stokes vector.  $2\psi$  is the longitude angle and  $2\chi$  is the elevation angle, the radius of the sphere is  $S_0$ .

Fig. 2.9. With a geometrical analysis of the Poincaré sphere we can reformulate the Stokes vector from a Cartesian description  $(S_1, S_2, S_3)$  to a spherical coordinate description with the angles  $2\psi$  and  $2\chi$ , which are called the longitude and elevation angles, respectively. Geometrical inspection of the Poincaré sphere leads to the relations

$$2\psi = \arctan\left(\frac{S_2}{S_1}\right) \quad (0 < \psi \leq \pi), \quad (2.14)$$

and

$$2\chi = \arctan\left(\frac{S_3}{S_1^2 + S_2^2}\right) \quad \left(-\frac{\pi}{4} < \chi \leq \frac{\pi}{4}\right). \quad (2.15)$$

Thus the position of the Stokes vector on the Poincaré sphere can be represented in spherical coordinates with  $(S_0, 2\psi, 2\chi)$ <sup>13</sup>. All linear polarization states (X,Y,D,A,...) lie on the equator of the sphere, while the north pole corresponds to right circularly ( $\sigma_+$ ) polarized light and the south pole to left circularly ( $\sigma_-$ ) polarized light as labeled in Fig. 2.9. The Poincaré sphere is an extremely useful

<sup>13</sup>Note that in this coordinate system the elevation angle  $2\chi$  is taken to be the inclination above (or declination below) the equatorial plane, which is different from the standard spherical coordinate formulation using the polar angle (angle away from the +z axis). See Fig. 2.9.

visualization tool, as any changes to the state of polarization can be represented by rotations about the different axes, which trace out trajectories on the surface of the sphere.

## 2.3 The AC Stark Effect

When coherent radiation (a laser beam) interacts with a quantum system many interesting dynamics arise. The AC Stark effect describes the shift induced on the energy levels of a quantum system when an oscillating electric field (radiation) interacts with an atomic or quantum system, and is simply the large-detuning limit of resonant radiation interacting with a transition dipole moment. This AC Stark effect is similar to the commonly treated DC Stark effect, where energy level shifts are induced by a constant-in-time applied electric field. The AC Stark effect is the mechanism used to coherently manipulate the energy level structure of QDs described in Chapter 5. Thus, a derivation from first principles for a two-level system is included here. This derivation mainly follows that of Scully and Zubairy [111].

Starting with the time dependent Schrodinger equation

$$i\hbar \frac{d|\Psi\rangle}{dt} = \hat{H} |\Psi\rangle, \quad (2.16)$$

we can write the Hamiltonian  $\hat{H}$  in terms of its time-independent and -dependent parts as

$$\hat{H} = \hat{H}_0 + \hat{H}_I(t), \quad (2.17)$$

where  $\hat{H}_0$  is the Hamiltonian of the unperturbed two level system, and  $\hat{H}_I(t)$  describes the interaction of the system with the oscillating electric field (radiation). For the unperturbed system we have that

$$\hat{H}_0 |n\rangle = E_n |n\rangle, \quad (2.18)$$

and we can write the state vector as

$$|\Psi\rangle = c_1 |1\rangle e^{-i\omega_1 t} + c_2 |2\rangle e^{-i\omega_2 t}, \quad (2.19)$$

where  $|n\rangle$  are the eigenstates of the unperturbed system,  $\omega_n = E_n/\hbar$ , and the explicit time dependence of the coefficients  $c_1(t)$  and  $c_2(t)$  has been dropped in favor of the simpler notation  $c_1$  and  $c_2$  where the time dependence is implicit. Normalization dictates that the relation

$$|c_1|^2 + |c_2|^2 = 1, \quad (2.20)$$

be satisfied.

Next we explicitly introduce the the time-dependent perturbation

$$\hat{H}_I(t) = e\vec{r} \cdot \vec{E}_0 \cos(\omega t), \quad (2.21)$$

where  $e$  is the charge of an electron,  $\vec{r}$  is the position of the electron,  $\vec{E}_0$  encapsulates the strength and oscillation direction of the field, and  $\omega = E/\hbar$  is the frequency of oscillation. Plugging the state vector  $|\Psi\rangle$  (Eq. 2.19) and the Hamiltonian (Eqs. 2.17 and 2.21) into the time-dependent Schrodinger equation (Eq. 2.16) yields

$$\begin{aligned} i\hbar(\dot{c}_1 |1\rangle e^{-i\omega_1 t} - i\omega_1 c_1 |1\rangle e^{-i\omega_1 t} - i\omega_2 c_2 |2\rangle e^{-i\omega_2 t} + \dot{c}_2 |2\rangle e^{-i\omega_2 t}) = \\ c_1 E_1 |1\rangle e^{-i\omega_1 t} + c_2 E_2 |2\rangle e^{-i\omega_2 t} + \\ c_1 e\vec{r} \cdot \vec{E}_0 \cos(\omega t) |1\rangle e^{-i\omega_1 t} + c_1 e\vec{r} \cdot \vec{E}_0 \cos(\omega t) |1\rangle e^{-i\omega_1 t}. \end{aligned} \quad (2.22)$$

This equation can be separated into two rate equations (one for each energy level) that form a system of coupled first-order differential equations. To arrive at this system we apply the Hermitian conjugate  $\frac{1}{\hbar}(|n\rangle e^{-i\omega_n t})^\dagger$  twice to Eq. 2.22, once for  $n = 1$  and once for  $n = 2$  which results in

$$i\dot{c}_1 = \Omega \cos(\omega t) e^{-i\omega_0 t} c_2, \quad (2.23a)$$

$$i\dot{c}_2 = \Omega^* \cos(\omega t) e^{i\omega_0 t} c_1, \quad (2.23b)$$

where  $\omega_0 = \omega_2 - \omega_1$  is the frequency of the transition, and  $\Omega$  is called the Rabi frequency and defined by

$$\Omega = \frac{e}{\hbar} \langle 1 | \vec{r} \cdot \vec{E}_0 | 2 \rangle. \quad (2.24)$$

For reference, as stated in the QD introduction section (Sec. 2.1) the typical size of the confinement potential of InGaAs QDs is  $a_{x,y} \approx 20$  nm in the lateral plane, and  $a_z \approx 5$  nm in the vertical direction. The transition wavelength for InGaAs QDs is in the range  $\lambda = 900 - 950$  nm. Therefore the electric field has an almost uniform amplitude over the electron wave function, which means that the dipole approximation can be made (i.e.  $\lambda \gg a_{x,y,z}$ ), and the amplitude  $|\vec{E}_0|$  can be taken outside the integral in Eq. 2.24. This allows the Rabi frequency to be

written in simpler form in terms of the transition dipole moment  $\vec{d}$  as

$$\Omega = \frac{\vec{d} \cdot \vec{E}_0}{\hbar}, \quad (2.25)$$

where

$$\vec{d} = e \langle 1 | \vec{r} | 2 \rangle. \quad (2.26)$$

Using Euler's formula to rewrite the  $\cos(\omega t)$  in Eq. 2.23 we can write

$$i\dot{c}_1 = \frac{\Omega}{2} \left( e^{i(\omega - \omega_0)t} + e^{-i(\omega + \omega_0)t} \right) c_2, \quad (2.27a)$$

$$i\dot{c}_2 = \frac{\Omega^*}{2} \left( e^{i(\omega + \omega_0)t} + e^{-i(\omega - \omega_0)t} \right) c_1. \quad (2.27b)$$

In each of these equations, the term with  $(\omega + \omega_0)t$  in the exponent oscillates very fast and therefore averages to 0 over any reasonable interaction time. Additionally for transitions between bound states the Rabi frequency is real, i.e.  $|\Omega|^2 = \Omega^2$  or  $\Omega = \Omega^*$ . These two points simplify the equations to

$$i\dot{c}_1 = \frac{\Omega}{2} e^{i\Delta t} c_2, \quad (2.28a)$$

$$i\dot{c}_2 = \frac{\Omega}{2} e^{-i\Delta t} c_1, \quad (2.28b)$$

where  $\Delta = \omega - \omega_0$  is defined as the detuning of the laser from resonance. This approximation involving the  $(\omega + \omega_0)t$  exponent term is known as the rotating wave approximation [111], and is a robust approximation for optical dipole interactions. This system of two first-order coupled differential equations can be combined into a single second-order differential equation for the population of the excited state  $c_2$  as

$$\ddot{c}_2 + i\Delta\dot{c}_2 + \frac{\Omega^2}{2} c_2 = 0. \quad (2.29)$$

Solving this equation with the initial conditions  $c_1(0) = 1$  and  $c_2(0) = 0$  we arrive at an equation for the population of the excited state

$$|c_2(t)|^2 = \frac{\Omega^2}{W^2} \sin^2 \left( \frac{Wt}{2} \right), \quad (2.30)$$

where  $W^2 = \Omega^2 + \Delta^2$ , and is often called the "generalized Rabi frequency". Note that when the laser is resonant with the transition frequency, i.e.  $\omega = \omega_0$ , we



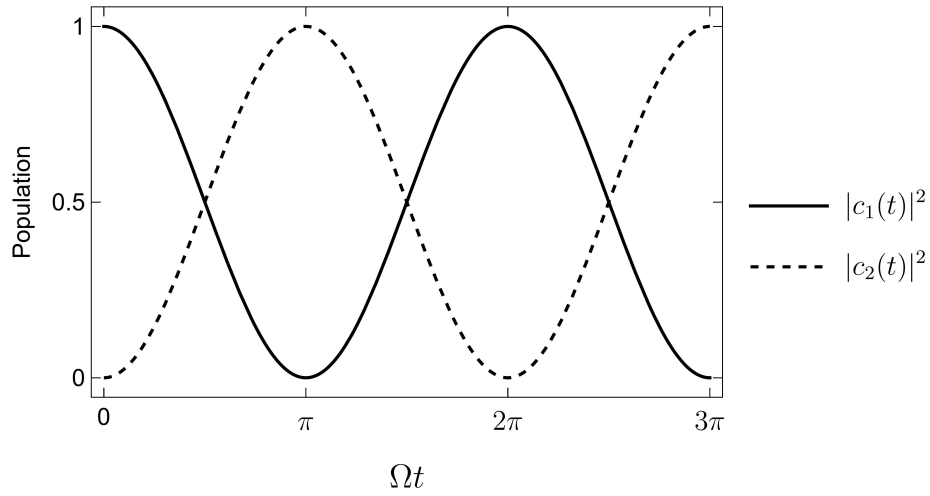


FIGURE 2.10: Plots of the rate equations for the populations of the ground state  $|c_1(t)|^2$  (solid) and the excited state  $|c_2(t)|^2$  (dashed) of a two-level quantum system under resonant excitation.

have that  $W = \Omega$  which gives the on-resonance population

$$|c_2(t)|^2 = \sin^2\left(\frac{\Omega t}{2}\right). \quad (2.31)$$

Figure 2.10 shows the evolution of the populations  $|c_1(t)|^2$  and  $|c_2(t)|^2$  of the system as time evolves<sup>14</sup>. As can be seen, on resonance the population will oscillate between the ground and excited states with periodicity in  $\Omega t$ . The population starts entirely in the ground state as dictated by the initial condition  $c_1(0) = 1$ . The population has gone entirely from the ground state to the excited state at time  $\Omega t = \pi$ , and at time  $\Omega t = 2\pi$  the system has returned to the initial state with all of the population in the ground state. These oscillations between the two states are called Rabi oscillations [111].

Applying the transformations

$$\tilde{c}_1 = c_1 e^{-i\Delta t/2}, \quad (2.32a)$$

$$\tilde{c}_2 = c_2 e^{i\Delta t/2}, \quad (2.32b)$$

<sup>14</sup> $|c_1(t)|^2$  is directly found from Eq. 2.20.

and their first derivatives to Eq. 2.28 leads to

$$i\dot{\tilde{c}}_1 = \frac{1}{2}(\Delta\tilde{c}_1 + \Omega\tilde{c}_2), \quad (2.33a)$$

$$i\dot{\tilde{c}}_2 = \frac{1}{2}(\Omega\tilde{c}_1 - \Delta\tilde{c}_2). \quad (2.33b)$$

This pair of equations can be naturally put into matrix form as

$$i\frac{d}{dt} \begin{pmatrix} \tilde{c}_1 \\ \tilde{c}_2 \end{pmatrix} = \frac{1}{2} \begin{pmatrix} \Delta & \Omega \\ \Omega & -\Delta \end{pmatrix} \begin{pmatrix} \tilde{c}_1 \\ \tilde{c}_2 \end{pmatrix}, \quad (2.34)$$

which gives defines a Hamiltonian describing the system

$$\hat{H}_{two-level} = \frac{1}{2} \begin{pmatrix} \Delta & \Omega \\ \Omega & -\Delta \end{pmatrix}. \quad (2.35)$$

The energy eigenvalues of this  $2 \times 2$  matrix are

$$\lambda_{\pm} = \pm \frac{1}{2} \sqrt{\Omega^2 + \Delta^2}. \quad (2.36)$$

The unperturbed system corresponds to  $\Omega = 0$ , and thus has  $\lambda = \pm \frac{\Delta}{2}$ , which shows that the two levels are  $\Delta$  apart, rather than  $\omega_0$  apart. This point illustrates a key nuance: this Hamiltonian  $\hat{H}_{two-level}$  describes the shifts of the excited state  $|2\rangle$  at unperturbed frequency  $\omega_2$ , and the virtual state created by the unperturbed ground state  $|1\rangle$  plus one photon of radiation field, which lies at frequency  $\omega_1 + \omega$ . This description is easily generalized to the whole "ladder" of possible states by addition and subtraction of single photons of radiation. This leads directly to the "dressed states" picture [111, 112], which is a convenient way of describing the entire atom-laser system<sup>15</sup>. Figure 2.11 shows the dressed states picture for a resonant laser ( $\omega = \omega_0$ ). Emission and absorption processes are labeled in the bare states case on the left. Stimulated emission and absorption involve addition or subtraction of one photon of laser field to or from the atom-laser system by the atom, respectively, which occurs in combination with a change in energy level of the atom. Therefore, these processes do not change the atom-laser system energy. Comparatively, spontaneous emission occurs when

<sup>15</sup>Really this can be thought of as any "quantum emitter (atom, QD, vacancy center)"-laser system. For simplicity of description here I refer to an atom-laser system.

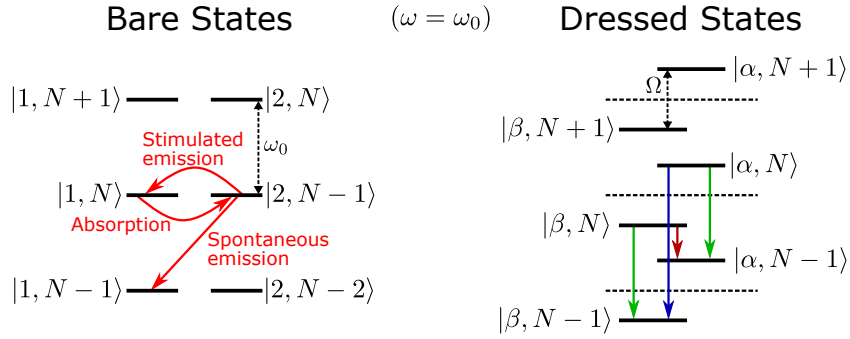


FIGURE 2.11: Dressed states picture for a resonant laser ( $\omega = \omega_0$ ). The bare states are shown on the left, with absorption and emission processes labeled. The dressed states are shown on the right, where the states  $|\alpha\rangle$  and  $|\beta\rangle$  are superpositions of the bare states  $|1\rangle$  and  $|2\rangle$ .

the atom emits a photon into a mode that is not part of the laser field, and thus the system decreases energy by one "rung" of the ladder. The dressed states on the right shows how state mixing leads to a triplet; this feature is known as the Mollow triplet [111, 113]. This dressed states picture is a powerful tool for describing the interaction of coherent radiation with a quantum system.

In practical consideration the AC Stark shift is only of interest when the detuning of the laser  $\Delta$  is large relative to the strength of the interaction of the laser with the system  $\Omega$ , i.e.  $\Delta \gg \Omega$ . Rewriting  $\lambda_{\pm}$ , and using  $\frac{\Omega}{\Delta} \ll 1$  and the binomial approximation we can write

$$\lambda_{\pm} = \pm \frac{1}{2} \left( \frac{\Delta}{2} + \frac{\Omega^2}{4\Delta} \right). \quad (2.37)$$

Thus the perturbation shifts the states by  $\delta_{AC} = \pm \frac{\Omega^2}{4\Delta}$ . The symmetry of the eigenvalues  $\lambda_{\pm}$  mean that this treatment describes the system for both negative ( $\Delta < 0$ ) and positive ( $\Delta > 0$ ) values of the frequency detuning  $\Delta$ . Based on our definition of  $\Delta = \omega - \omega_0$ , a negative (positive) detuning corresponds to a laser with frequency  $\omega$  which is less (greater) than that of the transition  $\omega_0$ . Figure 2.12 shows the frequency shifts as a function of Rabi frequency  $\Omega$  for the ground state  $|1\rangle$  at frequency  $\omega_1$ , the excited state  $|2\rangle$  at  $\omega_2$ , and the virtual state at frequency  $\omega_1 + \omega$ <sup>16</sup> for both negative (left) and positive (right) detunings. A

<sup>16</sup>Ground state plus one photon of laser field.

negative (positive) detuning shifts the excited state to higher (lower) frequencies.

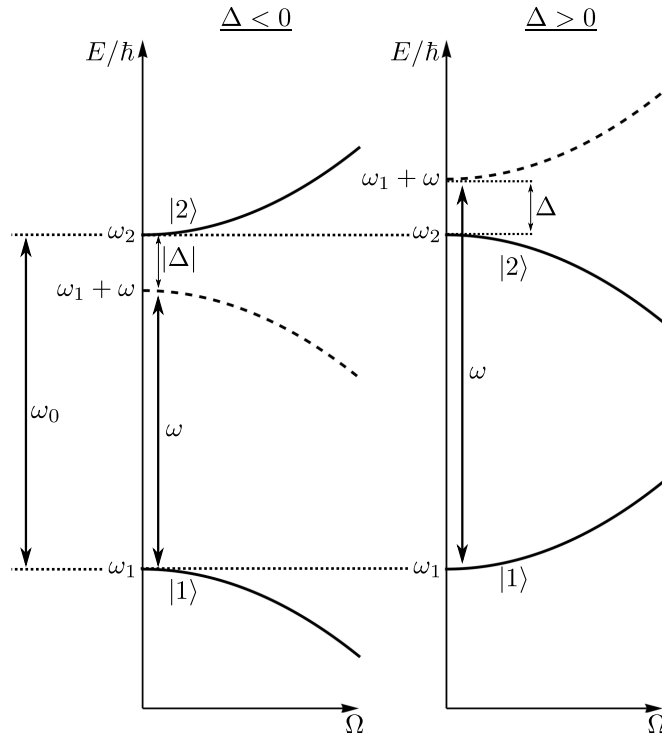


FIGURE 2.12: AC Stark frequency shifts of a two-level quantum system under the influence of a far-detuned laser for negative and positive detunings, shown on the left and right, respectively.  $\omega_1$  and  $\omega_2$  are the ground and excited state frequencies, respectively,  $\omega_0 = \omega_2 - \omega_1$  is the transition frequency, and  $\omega$  is the frequency of the radiation (laser).



## Chapter 3

# Experimental Techniques and Setup

The experiments discussed in this dissertation are carried out in two separate laboratories. The first is the Semiconductor Quantum Optics Laboratory (SQUOL) at West Virginia University (WVU), which provides resonant excitation spectroscopy for probing the QD energy level structure. The other is the Davanco lab housed at the National Institute of Standards and Technology (NIST) in Gaithersburg. This lab is part of the Single Emitters Group in the Physical Measurement Lab, and provides nanoscale optical positioning, imaging, and spectroscopy capabilities. The experiments performed at the WVU lab are centered around manipulating the energy levels of individual QDs, and measuring the energy level structure with resonant excitation spectroscopy. The experiments at NIST are designed to automate spectroscopy of many QDs at once, such that the characteristics of many QDs can be evaluated in batch for various device applications. The first section of this chapter (Sec. 3.1) covering the WVU experiments overviews resonant excitation spectroscopy and the novel optical filtering scheme that enables the production and measurement of the AC Stark shifts discussed in Chapter 5. The second section (Sec. 3.2) discusses the automated spectroscopy work at NIST, and includes some results and outlook on future directions for the work.

### 3.1 Semiconductor Quantum Optics Laboratory (SQUOL) at WVU

The resolution of a typical spectrometer with a 1200 gr/mm grating is  $\sim 35$  GHz, while the linewidth of an InGaAs QD transition is  $\sim 1$ -2 GHz. Thus, this precludes the spectrometer from resolving the energy level structure of individual QDs. In order to probe the energy structure we employ resonant photoluminescence excitation (RPLE) spectroscopy, in which the frequency of a low intensity laser is scanned over the frequency of the QD transition. As the laser frequency is scanned it will resonantly excite any transitions it crosses and the QD will emit photoluminescence (PL). This PL emitted from the dot is collected and integrated by the spectrometer. The result is an excitation spectrum that is a direct probe of the QD energy levels, with the resolution being limited only by the linewidth of the resonant excitation laser, which is  $\sim 1$  MHz. Fig 3.1 illustrates this spectroscopic technique, and shows an image of a resonantly excited QD<sup>1</sup>. In this way we directly measure the energy level structure of QDs, and can use this technique to measure any changes to this structure. To directly measure the emission spectrum of a QD, a high-resolution, stabilized scanning Fabry-Perot cavity is necessary, and one such device is currently under construction in our lab. Other optical elements such as a virtually imaged phased array (VIPA)

<sup>1</sup>The circular ring-like feature surrounding the dot is called an Airy-ring, and is an artifact of the point-spread function of the imaging system [114].

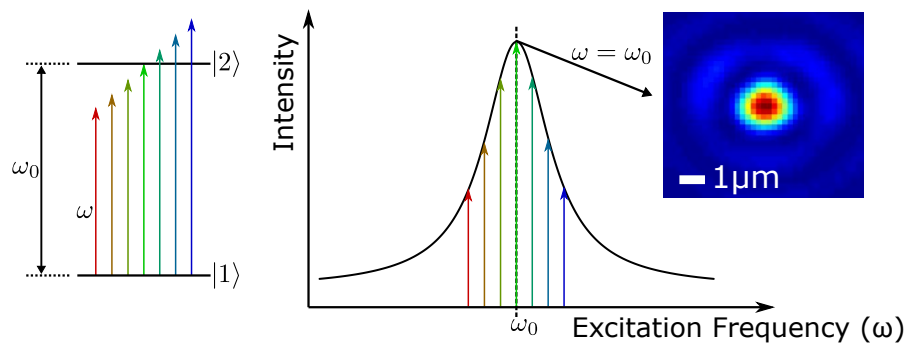


FIGURE 3.1: Resonant photoluminescence excitation (RPLE) spectroscopy. A resonant laser is scanned across the transition resonances, and emitted PL is collected and integrated by a spectrometer. The inset shows an image of resonantly excited QD captured by the spectrometer.

might also be applicable to this measurement, as discussed at the end of the NIST experimental section (Sec. 3.2).

One significant problem in resonant excitation spectroscopy in quantum optics is discriminating the scattering of the resonant excitation laser from the weak PL emitted by the single quantum emitter. One long-standing remedy to this problem is to use a cross-polarization scheme of orthogonal excitation and detection to filter the laser scattering from the detected signal [115, 116]. Unfortunately this approach necessarily limits the freedom of choice in detection polarization, which limits experimental capabilities. One interesting alternative that has been developed recently utilizes elliptical microcavities, which couple differently to the orthogonal dipoles of QD transitions [69]. As discussed in Sec. 2.1 the samples used at WVU contain QDs grown inside of planar DBR cavities [67, 74], which provide the convenient opportunity to couple the resonant light into the planar waveguide mode via side excitation [117]. In this way the resonant light is able to excite the dot, and any photons that do not interact with the dot continue propagating in the waveguide mode, while the emitted PL is collected out of plane in the Fabry-Perot mode and sent to the spectrometer [117, 118]. This is the excitation mode that is used for our RPLE scheme throughout this dissertation.

As mentioned in the charge control section (Sec. 2.1.3), the QDs in the sample used for measurements in the WVU lab are grown in a diode structure, and embedded in a  $1\text{-}\lambda$  planar microcavity formed by two AlGaAs/GaAs DBRs. Each DBR is grown in a superlattice structure where each individual alternating sublayer of AlGaAs and GaAs is designed to have thickness  $\lambda_0/4n_{\text{AlAs}}$  and  $\lambda_0/4n_{\text{GaAs}}$ , respectively. The wavelength  $\lambda_0$  is chosen to be at the center of the QD distribution, which is  $\lambda_0 \approx 927\text{ nm}$  for this sample. The upper DBR has 4 periods and the lower DBR 10 periods. The QD layer has a density of  $10^9\text{ cm}^{-2}$ , and is located in the middle of the GaAs cavity between the DBRs. The top (bottom) of the cavity is p-doped (n-doped), forming a p-i-n-i-n diode structure around the QDs (see Fig. 2.2 for reference). The sample is etched in two areas to two different depths, so that ohmic contact can be made directly to the doped regions of the cavity; for all experiments described here we probe a dot in the unetched area (right side of Fig. 2.2). As discussed, applying a bias voltage across the diode can charge the QD with a single electron that tunnels in from the n-doped region [100].



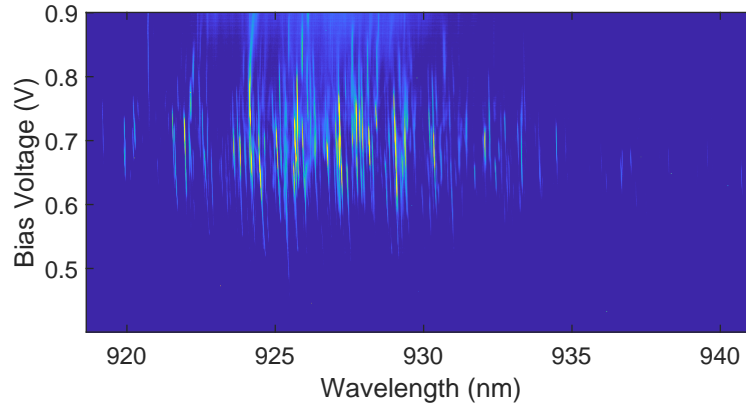


FIGURE 3.2: Bias voltage PL intensity map showing the voltage dependence of many dots. The QDs are excited by above band HeNe excitation at  $\lambda = 632.8$  nm.

We can excite many QDs in one field of view simultaneously using an above-band-gap (HeNe) laser<sup>2</sup>. With many dots constantly excited we can scan the voltage bias applied to the sample and elucidate the bias-dependence for many dots at once. Such a scan is called a voltage or bias map, and an example is shown in Fig. 3.2. These maps inform on the voltage and wavelength range in which to look for QDs, and also show which dots might be brightest for a specified voltage. From Fig. 3.2 we see that most dots lie in the range of 0.55-0.8

<sup>2</sup>Lasing at  $\lambda = 632.8$  nm the HeNe photons are at far higher energy than the QD distribution at  $\lambda = 910 - 940$  nm.

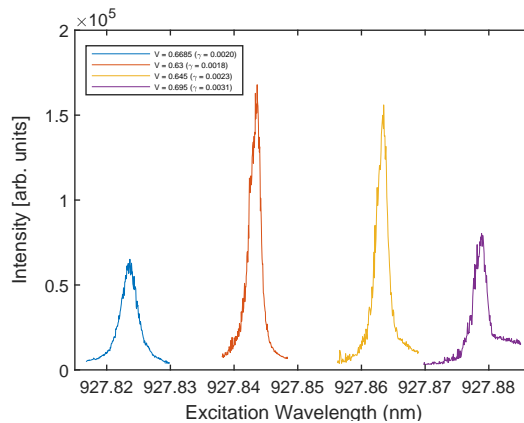


FIGURE 3.3: Excitation spectra for a single QD at four different bias voltages. Higher bias voltages corresponds to a higher transition frequency (shorter wavelength).

V, and can also see the change in stable charge state of individual dots. Additionally, we examine the voltage dependence of the excitation spectra of single QDs. Fig. 3.3 shows excitation spectra acquired using RPLE for a single QD at four different bias voltages. The frequency, linewidth, and peak intensity of the transition all have dependencies on the applied bias. Using these techniques we can select an individual QD for experiment, and select the optimal bias voltage setting for any given QD.

In order to utilize the AC Stark effect (Sec. 2.3) to manipulate the energy level structure of QDs an additional laser must be applied to the QD. The desire for the effect to selectively address only one transition, while leaving the other(s) unaffected, necessitates that the polarization of this AC Stark laser be able to match the QD transition dipole moment(s), which lie in the plane of the sample [83]. Excitation via the planar waveguide mode of the DBR cavity dictates that the excitation polarization be horizontally polarized, i.e. parallel to the sample surface (see Fig. 3.4). This limits the polarization state at the location of the dot to only one specific linear case. Thus the AC Stark laser cannot be applied via this waveguide mode because all polarization states must be accessible to this laser in order to selectively interact with individual transitions. Therefore we apply the AC Stark laser in confocal geometry<sup>3</sup>. This poses a filtering problem similar to resonant excitation, namely how to discriminate the very high power AC Stark laser from the weak QD fluorescence. While the AC Stark laser is spectrally distinct<sup>4</sup> from the QD PL, the intensity is large enough to completely

<sup>3</sup>Here confocal means applied in the same path as the PL collection path, i.e. the AC Stark laser and PL share common focal planes.

<sup>4</sup>In all cases presented here the AC Stark laser is detuned from the QD resonance by at least  $\pm 500$  GHz.

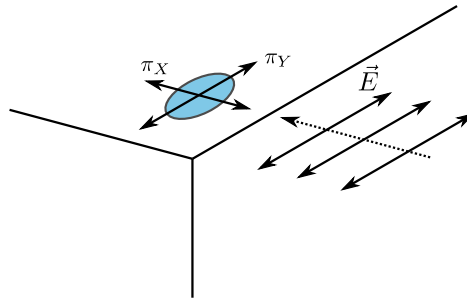


FIGURE 3.4: Geometry of side excitation via the planar waveguide mode of the DBR cavity.

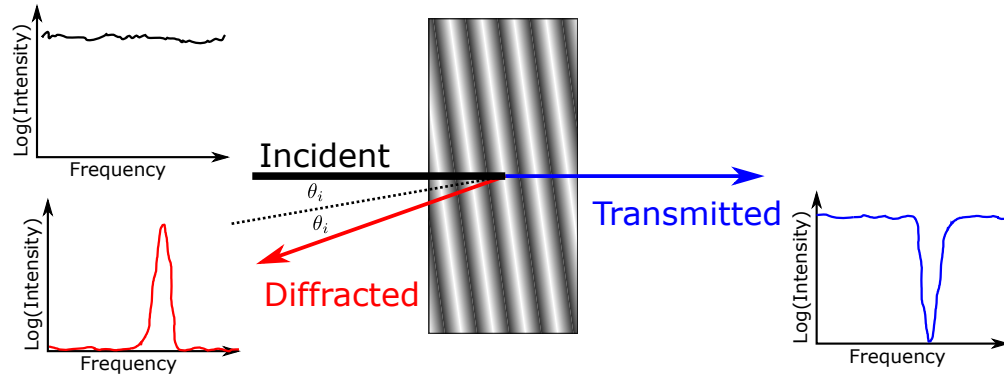


FIGURE 3.5: Schematic of reflective volume Bragg grating (VBG). The bandwidth of the diffracted peak (and correspondingly the transmitted dip) is  $\sim 50$  GHz.

saturate the CCD camera of the spectrometer even at the QD's wavelength when no filtering is used. To solve this problem we developed a novel optical filtering scheme using volume Bragg gratings (VBGs) [119] to sufficiently attenuate the AC Stark laser line such that the weak QD fluorescence is not overwhelmed on the CCD camera.

VBGs are volume holographic elements created by a system of planar layers with differing refractive index. They serve to act as narrow bandwidth optical notch filters, which refract a specific narrow-band of wavelengths at an angle from the incident light. The VBGs employed here are reflecting Bragg gratings,

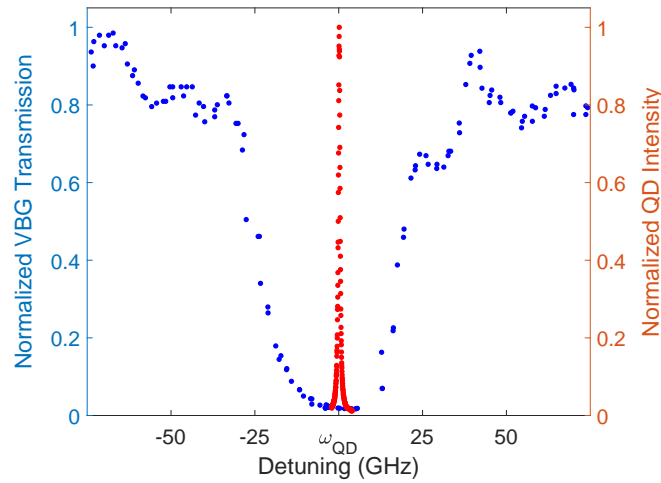


FIGURE 3.6: QD PL overlain with VBG transmission.

as the diffracted beam crosses the front surface of the grating<sup>5</sup>. Figure 3.5 shows the operating principle of these reflecting VBGs. The majority of wavelengths are transmitted through the grating unaffected, while a narrow bandwidth of light meets the Bragg condition and is diffracted by the planar refractive index variation inside the grating [119, 120]. For the VBGs used here the bandwidth of the diffracted light is  $\sim 50$  GHz, which is large compared to the typical  $\sim 1$ -2 GHz linewidth of an individual InGaAs QD, but small relative to the detuning of 500-1500 GHz for the AC Stark laser. Figure 3.6 shows an excitation spectrum of a single QD overlain with the measured transmission dip of one of our VBGs. This shows explicitly how nearly all of the QD light will be reflected by the VBG, while only a tiny fraction of the AC Stark laser light will be present in the reflected beam. Therefore, these gratings provide an effective means to discriminate the light of the weak QD PL from the strong AC Stark laser.

As discussed and seen in Fig. 3.2 the wavelength distribution of QDs in our sample spans a range of  $\sim 915$ -935 nm. The central wavelength of the light diffracted by the VBG shown in Figs. 3.5 and 3.6 can be shifted by changing the relative angle of the incident light and the internal structure of grating pattern,

<sup>5</sup>There are also transmitting VBGs where the diffracted beam crosses the back surface of the grating [120].

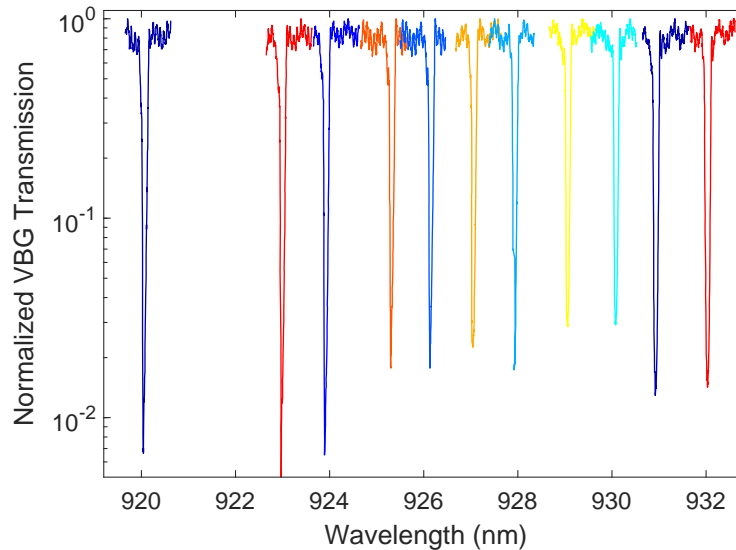


FIGURE 3.7: Transmission data for VBG at varying angles. The VBG is aligned at an arbitrary angle and a laser scanned over the reflection wavelength, while the transmitted power is measured by a photodiode.

i.e. rotating the grating. In order to evaluate the extent of this wavelength tunability we took transmission spectra with the grating at various angles. These data are shown in Fig. 3.7, and indicate an effective diffraction/transmission ratio of at least 97% and up to above 99% over the wavelength range of interest. Thus, the VBGs can be used as narrow bandwidth notch filters at the wavelength of any QD in our sample.

The filtering scheme developed to discriminate the AC Stark laser from the weak QD PL is shown in Fig. 3.8. The inset plots show the VBG transmission and the AC Stark laser spectrum to detail the filtering role of each grating<sup>6</sup>. VBG 1 cleans the spectrum of the laser by reflecting only the strong laser line, thereby

<sup>6</sup>The bandwidth of the VBG diffraction is exaggerated in the diagram as it is only  $\sim 50$  GHz and the detuning  $\Delta = \omega_{AC} - \omega_{QD} = 500$ -1500 GHz, as stated previously.

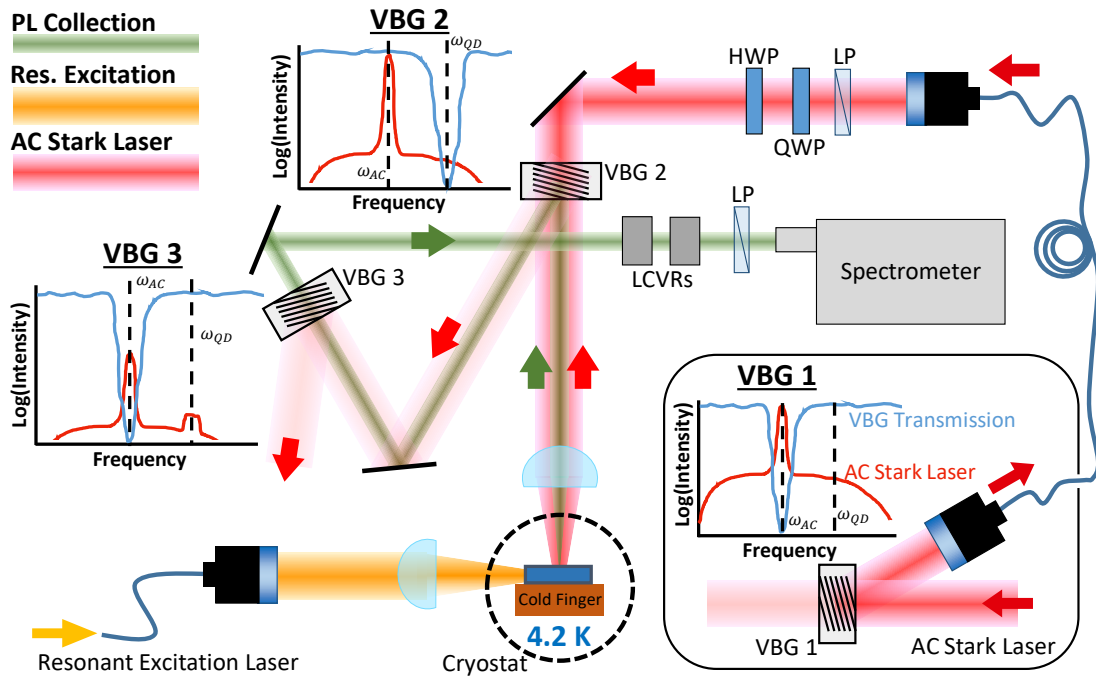


FIGURE 3.8: Schematic of the optical setup for AC Stark measurements. Inset plots show the filtering and attenuation of the AC Stark laser spectrum by the VBGs. Different optical paths are shown with different colors and propagation directions are indicated by colored arrows. VBG volume Bragg grating, LP linear polarizer, QWP quarter wave plate, HWP half wave plate, LCVRs liquid crystal variable retarders.

reducing the intensity of the amplified spontaneous emission (ASE) at the frequency of the QD transitions ( $\omega_{\text{QD}}$ ). VBG 2 is aligned to reflect the QD fluorescence ( $\omega_{\text{QD}}$ ) and transmit the AC Stark laser ( $\omega_{\text{AC}}$ ), which serves two purposes. The first is to inject the AC Stark laser into the collection path. The second is to attenuate scattering from the sample that would otherwise overwhelm the weak QD fluorescence on the detector of the spectrometer. VBG 3 transmits the fluorescence and reflects the AC Stark laser line, further attenuating it. The result is that the laser scattering that reaches the spectrometer's CCD detector is attenuated enough that it can be spectrally discriminated from the QD fluorescence without requiring polarization discrimination. The ASE at the frequency of the QD is also attenuated sufficiently enough that even though it is not spectrally distinct from the fluorescence, it is still orders of magnitude weaker.

To selectively address a single QD transition the polarization state of the AC Stark laser must be controlled. As shown in Fig. 3.8, the combination of a polarizer, a quarter-wave plate (QWP), and half-wave plate (HWP) in series provide this control. Due to the rotation of the Stokes vector by the different optical elements in the collection path, producing a known polarization directly downstream of the HWP will result in an unknown elliptical polarization at the sample surface. To compensate for this effect it is necessary to calibrate the polarizer and waveplate settings using the polarimeter device described in Chapter 4. The procedure is rather straightforward: placing the polarimeter directly in front of the sample and sending the AC Stark laser through the path, the Stokes vector at the sample can be measured. Setting the polarizer and waveplates to produce the desired polarization calibrates these elements, and thereby any desired polarization can be produced at the sample surface.

In order to apply consistent AC Stark laser powers to the dot for various polarizations and wavelengths, two more effects must be taken into consideration: polarization dependent reflection/absorption of the collection path, and wavelength dependent coupling into the DBR planar microcavity. The first effect is easily measured with an input/output power measurement for each polarization of interest. To account for the latter effect a reflection spectrum of the sample is taken. Figure 3.9 shows the reflection spectrum over the range of QD wavelengths for our sample. The vertical lines indicate the wavelength of the QD used for these experiments (green), an AC Stark laser blue-detuned by  $\Delta = 1000$  GHz (blue), and an AC Stark laser red-detuned by  $\Delta = -500, 1000, 1500$  GHz

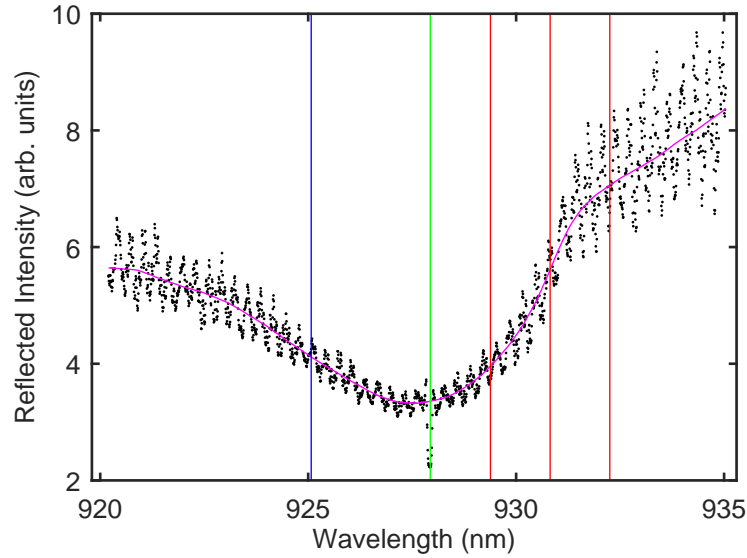


FIGURE 3.9: Sample reflection spectrum. Vertical lines indicate the wavelengths of QD light (green), a blue-detuned AC Stark laser (blue), and three different red-detuned AC Stark lasers (red). The magenta line is a local regression smoothing of the data.

(red). The filtering of VBG 2 in Fig. 3.8 can be seen in this spectrum at the wavelength of the QD, as expected. VBG 3 is not in the path for this measurement. The magenta line is a local regression using weighted linear least squares and a 1st order polynomial (lowess method). Evidently each of these wavelengths couples to the DBR cavity of the sample, and thus the QD, with different efficiencies. The measurement of these efficiencies shown in Fig. 3.9 allows application of consistent AC Stark laser powers at different wavelengths. Note that this reflection spectrum shows in principle a quality factor  $Q = \lambda/\Delta\lambda$  [67] of  $\sim 100$ , however this is likely larger than actual due to losses in collection of the reflected light.

We employ a pair of liquid crystal variable retarders (LCVRs) for detection polarization. The two LCVRs are placed directly upstream of a horizontally aligned linear polarizer in front of the spectrometer (see Fig. 3.8). Orienting the fast axes of the two LCVRs at  $45^\circ$  relative to each other<sup>7</sup> corresponds to two orthogonal rotation axes in the linear plane of the Poincaré sphere (Fig. 2.9). This enables any input polarization (Stokes vector) to be rotated to match the horizontal linear polarizer in front of the spectrometer by consecutive rotations

<sup>7</sup>Specifically in our setup these angles are vertical (Y) and diagonal (D).

about these two axes. The rotation angles are determined by the retardance of the crystal which is controlled by the voltages applied. As with the polarization elements for AC Stark laser control, the LCVRs must be calibrated to account for the polarization rotation induced by the optical elements comprising the collection path. The polarimeter device described in Chapter 4 again provides a convenient means for performing this calibration, and a description of this calibration is presented in Appendix B.

This section has been an overview of the experimental setup and techniques used for experiments in the SQUOL lab at WVU. The diode structure design of the sample allows charge state control of individual QDs, and tuning the bias voltage over the stable plateau changes the spectral properties. VBGs enable the development of a novel optical filtering scheme to discriminate the high-power, far-detuned, AC Stark laser from the weak QD fluorescence. This scheme is used in Chapter 5 to perform the AC Stark shift measurements described therein. A sample reflection spectrum is taken to account for the wavelength dependence of cavity coupling efficiency. Lastly, the polarimeter described in Chapter 4 provides a simple means to calibrate the various polarization optical elements employed here.



## 3.2 Automated Quantum Dot Spectroscopy at NIST

Large advancement has been made over the last twenty years in the design and fabrication of quantum devices based on self-assembled QDs. However, one significant limiting factor to the scalability of these devices is the inhomogeneous distribution of individual QD spectral properties due to the stochastic nature of the growth process [10, 53–56]. Many inventive methods have been developed in the realm of post-growth tuning of the emission wavelengths of multiple QDs into resonance, including using the Stark effect via electrical bias [121], temperature [122, 123], the AC Stark shift [37], Raman emission [124, 125], the application of strain using piezo-electric actuators [50, 126, 127], and several others [128, 129]. Unfortunately, these methods still necessitate that initial spectroscopy of many QDs be performed manually in order to determine dot positions and spectral properties. This poses an inconvenient and annoying hurdle in scaling up the production of QD-based devices: even if the growth and fabrication can be automated, spectroscopy will still need to be performed by a human.

The purpose of the laboratory work described in this section is to develop a method for performing automated high-resolution spectroscopy on many QDs to determine their spectral characteristics, and thereby their viability for use in device fabrication. The measurements are done on individual self-assembled InAs QDs in bulk GaAs, such that structures can be etched on top of them after characterization is complete. We use a photoluminescence imaging setup combined with image analysis algorithms to implement machine vision to track the positions of the individual QDs. Single QD light is automatically coupled into a single-mode fiber, sent through a scanning Fabry-Perot (SFP), and then to a spectrometer to acquire an emission spectrum. This measures the brightness, linewidth, and charge state of the QD. To perform these measurements we use the fiber-based nanoscale imaging, positioning, and spectroscopy setup [130–133] in the Davanco lab at NIST in Gaithersburg.

As discussed in Sec. 2.1 InGaAs QDs are grown via molecular beam epitaxy (MBE) in bulk GaAs. As mentioned, growth in bulk limits the PL collection efficiency from the QDs, as only a small percentage of emitted light can be collected as compared to dots in a DBR cavity, or other structure [67]. However, characterization in bulk affords freedom and flexibility in device fabrication after spectroscopy has been performed. The sample is placed on a stack of

piezo-electric inertial walkers which allows motion along three orthogonal directions ( $x,y,z$ ) inside a cryogen-free cryostat that reaches temperatures below 2K. The imaging and spectroscopy uses the nanoscale optical imaging system developed by the Single Emitters Group at NIST [130–133] combined with some additional elements, and shown in Fig. 3.10. The QDs are excited by a 630-nm above-band light emitting diode (LED), which is injected into the collection path via a 50:50 (reflection:transmission) beamsplitter. This light is focused onto the sample by a  $100\times$  infinity-corrected (0.9 numerical aperture) microscope objective lens which produces a  $\sim 100\text{ }\mu\text{m}$  diameter spot on the sample. This enables

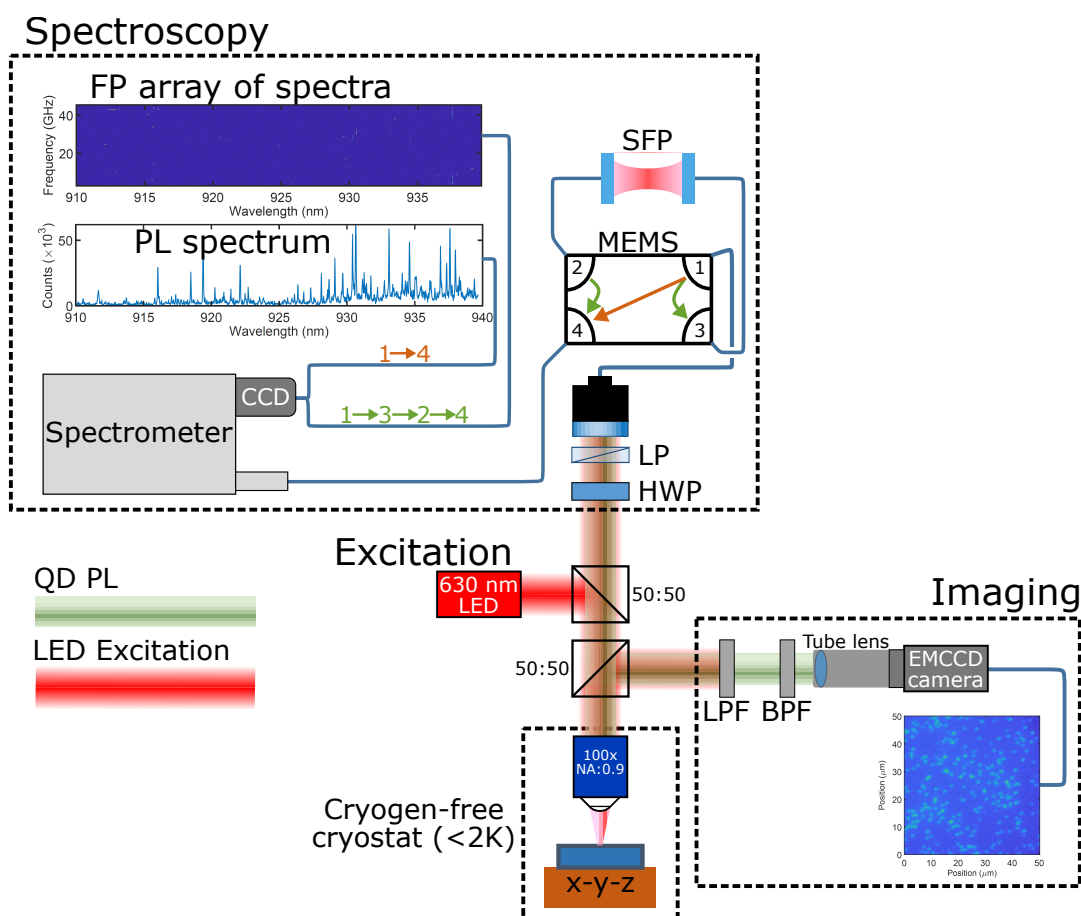


FIGURE 3.10: Schematic of imaging and spectroscopic setup used in the Davanco lab at NIST. The micro-electromechanical system (MEMS) switch allows automatic changing of the spectroscopy path. LED light-emitting diode, LPF long-pass filter, BPF band-pass filter, EMCCD electron multiplying charge coupled device, HWP half-wave plate, LP linear polarizer, SFP scanning Fabry-Perot.

wide-field excitation of all of the QDs in a single field of view of the imaging setup, which is approximately  $50\ \mu\text{m} \times 50\ \mu\text{m}$ . Fluorescence from the sample goes back through the 50:50 beamsplitter and is directed onto an electron multiplied charge coupled device (EMCCD) for imaging. A 900-nm long-pass filter (LPF) and a 930 10-nm band-pass filter (BPF) are inserted in front of the EMCCD camera to remove reflected 630 nm light and narrow the wavelength distribution of the observed dots, respectively.

In order to survey many QDs, the sample is automatically moved using the 3 axis piezo-electric inertial walkers to couple individual QD PL into a single-mode optical fiber. To achieve this a maximum-likelihood estimator is used to identify the centroid positions of QD emission in acquired images. Once an image is taken and the centroids found, the most efficient path for sampling the 10-30 brightest dots in a single field of view is determined. The problem of minimizing the distance of travel to each point in a two-dimensional plane is exactly the classic traveling salesman problem. This is an NP-hard problem, and becomes intractable to solve exactly once the number of points to visit reaches more than 8 or so<sup>8</sup>. Thus we employ a genetic algorithm [134, 135] to reach a good solution, if not the optimal one<sup>9</sup>. Figure 3.11(a) shows an example of the traveling salesman implementation in our system, and an example of the

<sup>8</sup>In this context intractable means requiring upwards of 10 minutes of computation time to solve.

<sup>9</sup>The traveling salesman genetic algorithm used here can be found on the MATLAB Central File Exchange: Joseph Kirk (2021). Traveling Salesman Problem - Genetic Algorithm, MATLAB Central File Exchange. Retrieved June 13, 2021.

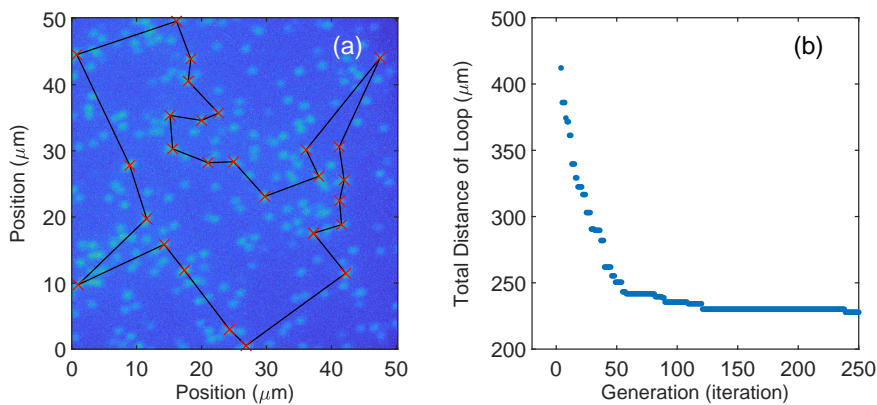


FIGURE 3.11: (a) Path determined by the traveling salesman genetic algorithm to sample the target dots in the most efficient manner, i.e. least distance traveled, and (b) best solution history.

generational-based evolution of the solution is shown in Fig. 3.11(b). As with every solution of the traveling salesman problem the ideal path is found to be a loop. Evolving the system for 2000 generations takes  $\sim 10$  seconds of computation time, and reliably arrives at a minimum solution for the number of emitters sampled here<sup>10</sup>. By minimizing the total distance to be traveled by the system this method greatly increases the efficiency of the sampling method.

Positioning a single QD beneath the collection fiber is achieved by calculating the vector between the dot and the fiber collection spot. Due to the somewhat unpredictable movement of the piezo stages multiple iterations of image acquisition and sample movement are needed to position the dot at the correct pixel<sup>11</sup>; typically the number of iterations does not exceed four. A vector comparison based image analysis approach is used to distinguish dots from one another and to track the same dot in subsequent images. This method is illustrated in Fig. 3.12. An initial image of the field of view is taken and analyzed to find the centroid positions of the  $\geq 7$  brightest QDs by a decreasing-threshold approach. A matrix  $A$  of QD vectors in the initial image is computed and stored for comparison. This matrix  $A$  is composed of all the possible vectors between all dots identified in the image. This QD vectors matrix  $A$  has dimensions  $N \times N$  for  $N$  dots found in the image<sup>12</sup>. In each subsequent image after the sample is

<sup>10</sup>Typically in the range of 7-30 in one field of view. Note that for the example shown, the curve decays to the asymptote of a minimum solution in only  $\sim 250$  generations.

<sup>11</sup>To within a tolerance of 2 pixels.

<sup>12</sup>The vector from a dot to itself is still computed, but will always be trivially  $= 0$ .

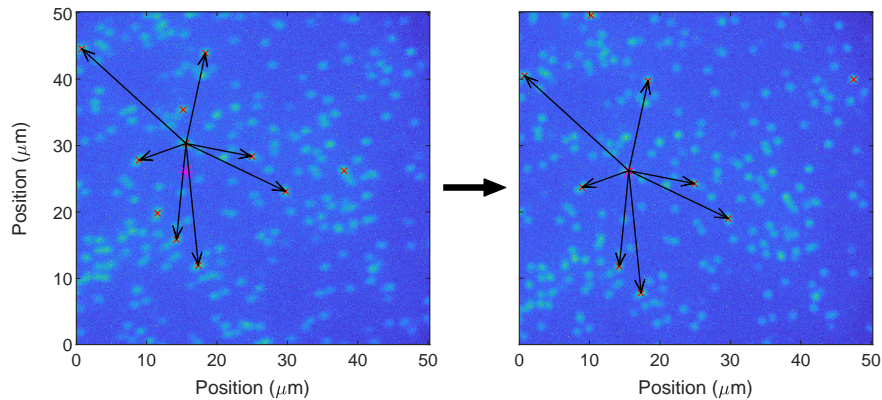


FIGURE 3.12: Illustration of machine vision vector comparison based approach to tracking individual QDs over many images taken at different sample locations.

moved a new matrix of QD vectors  $A_{\text{new}}$  is calculated and compared to the original matrix  $A$ . Because the number of dots found in each subsequent image may be different from the number found in the original image, the matrix  $A_{\text{new}}$  will have a different dimensionality of  $M \times M$ . To determine which dots are the same in different images the vectors for a given dot in  $A$  must be compared to all vectors found for each dot in  $A_{\text{new}}$ . If more than three of these vectors are found to be the same<sup>13</sup>, then two dots are found to be the same. To store the comparison information another matrix  $A_{\text{logic}}$  with dimensions  $N \times M$  is constructed. This logical matrix contains all 0s, except for in the cases where the  $i^{\text{th}}$  dot in the first image ( $A$ ) is found to match the  $j^{\text{th}}$  dot in the new image ( $A_{\text{new}}$ )<sup>14</sup>, in which case a 1 is entered. This method allows tracking individual dots over any number of images and sample movement. Using this method enables individual QD PL to be coupled into the collection fiber and the QD positions to be tracked such that they can be returned to if desired after spectroscopy is complete.

With PL from a single QD aligned into the collection fiber, we automatically perform two spectroscopic measurements. First a spectrum with a spectrometer is taken, which gives a measurement of the emission wavelength. Next a micro-electromechanical system (MEMS) switch is used to introduce the SFP into the path, which is then followed by the spectrometer, as shown in Fig 3.10. With this setup an array of spectra can be collected, which enables extraction of a high-resolution emission spectrum. Due to the unstable nature of the SFP the range of voltages over which to scan must be determined uniquely for each dot. Initially an entire free spectral range (FSR) must be scanned to ensure that the dot can be found. The SFP used here has a FSR of  $\sim 40$  GHz. The position of the QD peak in SFP voltage space is extracted from the emission spectra, and then a finer scan of only  $\sim 20$  GHz is taken in order to improve the resolution.

Figure 3.13 shows an overview of the array of spectra method used to obtain emission spectra for individual QDs. The coarse-resolution spectrum taken from the spectrometer alone is shown in Fig. 3.13(a). As discussed in the WVU experimental section (Sec. 3.1) the  $\sim 35$  GHz resolution of the spectrometer precludes obtaining any information about the relatively narrow  $\sim 1$ -2 GHz QD linewidth. However, this spectrum is still useful as it shows coarsely the wavelength relative to that of the overall QD ensemble. Fig. 3.13(b) shows a subset of the array

<sup>13</sup>To within a tolerance of 3 pixels.

<sup>14</sup> $i \in [1, N]$  and  $j \in [1, M]$ .

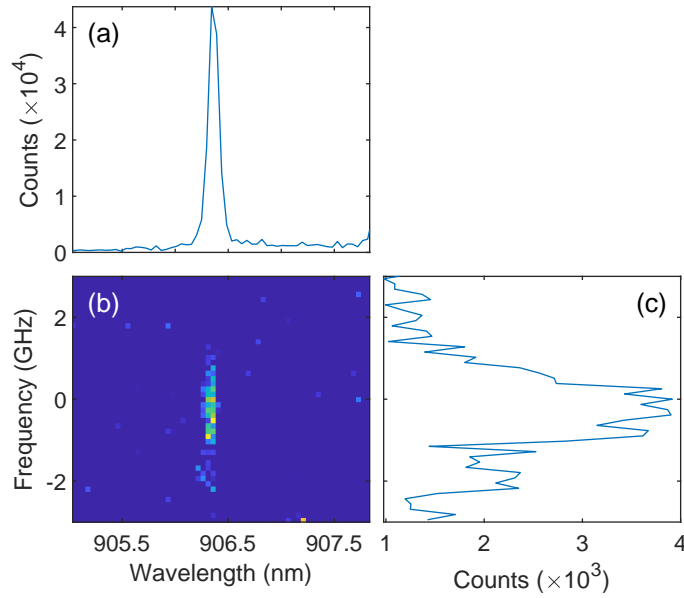


FIGURE 3.13: Emission spectrum method using the combination of a spectrometer and a SFP. (a) coarse spectrum from the spectrometer, (b) array of spectra from the SFP, and (c) the extracted emission spectrum.

of spectra collected by scanning the FP and acquiring spectra on the spectrometer. One horizontal row of this array corresponds to a single spectrum acquired on the spectrometer while the SFP is held at a steady voltage. The voltage is then changed and another spectra acquired, and the array is filled out in this fashion. Fig. 3.13(c) shows the emission spectrum extracted from Fig. 3.13(b) by binning five columns (two on each side) around the central wavelength of the QD extracted from the coarse spectrum in Fig. 3.13(a). We see that this reveals the narrow linewidth of this QD.

We acquired many emission spectra for QDs in bulk using this method. Figure 3.14 shows four emission spectra representative of the best results acquired thus far. The detection polarization for these measurements was linear. Note the spectra displayed here are extracted from the second array of spectra taken after the position of the peak in SFP voltage space is determined, which is why the frequency range covered by each spectrum is different. The spectra in Fig. 3.14(a-b) show single peaks or singlets, while Fig. 3.14(d) shows clearly a double peak or doublet. Recall from the QD charge state Sec. 2.1.2 that a QD in the neutral charge state generally has two non-degenerate excited states denoted  $|X\rangle$  and



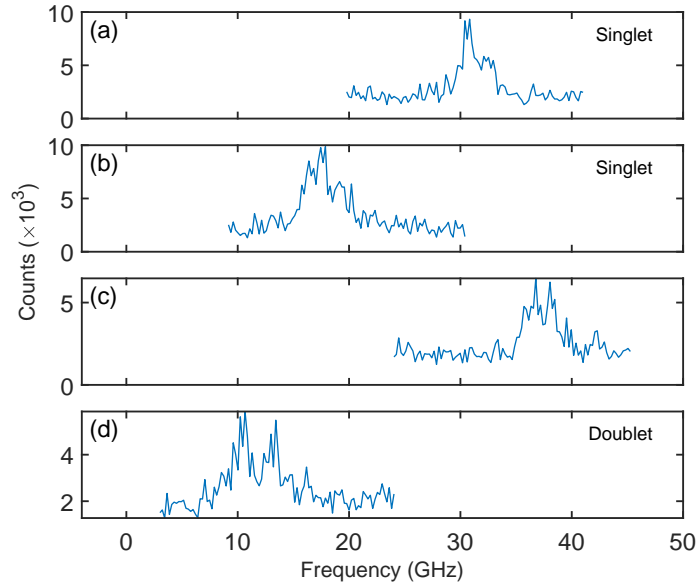


FIGURE 3.14: Emission spectra from QDs in bulk using the array of spectra method outlined in Fig. 3.13. The detection polarization was linear for these measurements. (a-b) are likely singlets, while (d) presents a doublet, and (c) is somewhat in between and unclear.

$|Y\rangle$  (Fig. 2.4), which are split by  $\delta_{\text{FSS}}$  due to the fine structure splitting (FSS) induced by the QD structural asymmetry. Comparatively a negatively charged QD in no magnetic field has two allowed transitions which are degenerate (see Fig. 2.5) [83, 84]. This distinct difference provides two separate expectations for the emission spectra of these two charge states: a neutral dot should show a doublet, and a charged dot a singlet. Using this key distinction, we can determine from emission spectra such as those shown in Fig. 3.14 the likely charge state of individual dots, as well as the linewidths, peak brightness, and FSS. For example, fits of Fig. 3.14(a-c) with a single lorentzian function give linewidths of  $\gamma = 2.31 \pm 0.36$ ,  $3.47 \pm 0.45$ , and  $2.78 \pm 0.74$  GHz, respectively. A fit of Fig. 3.14(d) with a two-peak lorentzian reveals linewidths of  $\gamma_1 = 1.50 \pm 0.59$  and  $\gamma_2 = 1.54 \pm 0.46$  GHz, with a FSS of  $\delta_{\text{FSS}} = 2.81 \pm 0.23$  GHz. This shows explicitly how this method can be used to determine spectral properties of individual QDs.

None of the spectra shown in Fig. 3.14 have a good signal to noise ratio (SNR). This is mainly due to the very low transmission efficiency of the SFP cavity that filters the light to acquire the high-resolution emission spectrum. This is evident in the relatively large uncertainty of the fit parameters noted in the

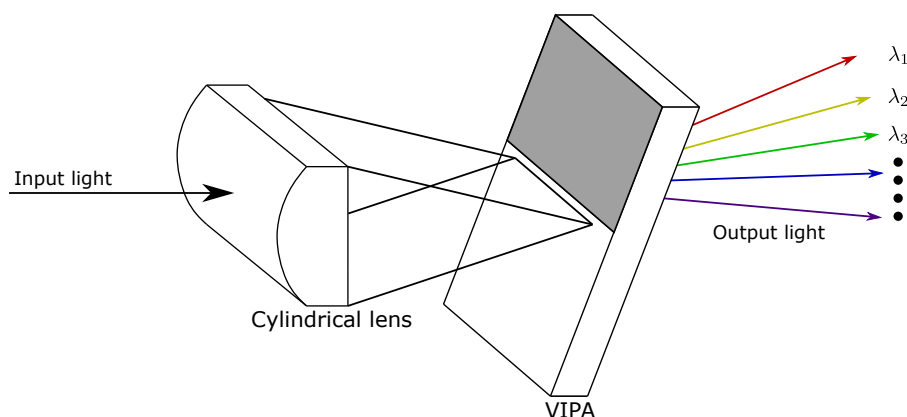


FIGURE 3.15: Schematic operation of a virtually imaged phased array (VIPA). The cylindrical lens focuses the light to a line focus, and the VIPA spreads wavelengths in the vertical direction while leaving the horizontal dimension unaffected.

previous paragraph. To maximize the SNR the exposure time for a single spectrum on the spectrometer must be rather long<sup>15</sup>. Thus the time to take an entire spectrum is rather long, and can be upwards of 30 minutes depending on the number of points taken in FPI voltage/frequency space. Attempts to increase the SNR by optimizing coupling of fibers and coupling to the SFP cavity have yielded minor improvements at best; unfortunately a simple SFP inherently has low transmission efficiency<sup>16</sup>. The low efficiency of the SFP combined with the low collection efficiency of QDs in bulk as discussed in Sec. 2.1 mean that an alternative method may be necessary to obtain emission spectra with better SNR.

One potential solution to this problem is to employ a virtually imaged phased array (VIPA) [137] in place of the SFP for acquisition of the high-resolution emission spectra. In simplest terms a VIPA is an optical element which induces large<sup>17</sup> angular dispersion based on wavelength. Figure 3.15 shows a schematic of the basic optical setup for a VIPA. The light is focused to a line focus by a cylindrical lens in front of the VIPA, and light at the output is then angularly dispersed in the vertical direction based on wavelength. The

<sup>15</sup>For the spectra shown in Fig. 3.14 the exposure time was in the range of 3-10 seconds/data point.

<sup>16</sup>This low transmission efficiency is partially by design: the function of the SFP is to serve as a narrow-band filter, so it purposely only transmits wavelengths in a narrow range. Additionally, SFPs will be subject to other sources of loss like scattering due to nanoscopic surface roughness, which reduces their efficiency from the ideal case [136].

<sup>17</sup>In this context large means large compared to the angular dispersion induced by a diffraction grating.



VIPA itself is simply a thin plate of glass made up of two regions with different reflection coatings. Of important significance and note here is that the VIPA only affects the vertical angle of the light, while the horizontal angle remains unaffected [137, 138]. This convenient feature allows a VIPA to be used in tandem with the diffraction grating of a spectrometer to produce a two-dimensional hyper-spectral image on the detector (CCD camera). The angular spread in the horizontal axis from the diffraction grating remains, while the VIPA spreads the light in the vertical axis with high resolution. In principle this technique with a VIPA will enable the acquisition of high-resolution emission spectra from single QDs, as the VIPA has  $\sim 50\times$  the transmission efficiency over that of a simple Fabry-Perot.

In the conclusion, automated spectroscopy of single quantum dots has been shown to work at a proof-of-principle level. The sample can be automatically driven to couple individual QD PL into a single mode fiber, and thereby to a spectrometer or SFP for analysis. The optimal path of travel between all emitters is calculated by a traveling salesman genetic algorithm. Emission spectra acquired using the SFP show a poor SNR due to the low transmission efficiency of the Fabry-Perot. In principle the use of a VIPA should allow for acquisition of high-resolution emission spectra with far better SNR, and work is underway to realize this scheme. Lastly, Appendix A discusses implementation of an automatic image focusing routine to enable sampling of dots over many fields of views (FOVs). This will be used in combination with feature recognition to sample upwards of 80 FOVs worth of QDs automatically.

## Chapter 4

# Polarimetry

This chapter describes the design, construction, and evaluation of a rotating waveplate polarimeter device to measure the Stokes parameters. Description of the production, control, and measurement of polarized light in the context of the experiments performed is also included. The work presented in this chapter describing the polarimeter device was published by Wilkinson et al. in Review of Scientific Instruments in 2021 [139].

### 4.1 Motivation

The polarization state of light, described by the Stokes vector  $\mathbf{S} = [S_0, S_1, S_2, S_3]$  [104], is of critical importance in a broad range of optical experiments [140]. Coupling light to a polarization maintaining fiber requires that the polarization of the input beam be matched to the polarization axis of the fiber [141]. Calibration of liquid crystal variable retarders (LCVRs), a common polarization manipulation component, requires precise knowledge of both the reference and output polarizations [142]. Additionally, the polarization state of a coherent laser beam plays a pivotal role in selectively addressing transition dipole moments. As outlined in the AC Stark theory section (Sec. 2.3), the strength of interaction between an optically active transition and an incident laser beam is determined by the Rabi frequency of the interaction  $\Omega = \vec{d} \cdot \vec{E}$ , where  $\vec{d}$  is the electric dipole moment of the transition and  $\vec{E}$  is the electric field of the laser (Eq. 2.25). In experimental situations the direction of oscillation of the electric field vector  $\vec{E}$  determines the relative strength of the interaction, because the fixed orientation of the QD (and sample at large) means the direction of the dipole moment  $\vec{d}$  will be constant. From Sec. 2.2 we can recognize that the direction of oscillation of the electric field vector  $\vec{E}$  is exactly the polarization of light. These are a few of the

many experimental situations that need highly accurate knowledge of the polarization state of light. Therefore, the complete measurement and characterization of the polarization of light is of widespread interest and importance.

Here we describe a self-contained, portable, inexpensive polarimeter capable of complete Stokes vector characterization of any input polarization. It can be constructed by combining optical and optomechanical elements common in any optics lab with a few additional inexpensive mechanical and electronic components. The implementation presented here combines aspects seen separately in previous realizations [143–148] and adds an Arduino microcontroller for data analysis, display, and recording.

The polarimeter is based on a rotating quarter-wave ( $\lambda/4$ ) plate (QWP), a polarizer (called the analyzer), and a photodiode in series [149]. In general, linearly polarized light can be distinguished from circularly polarized light by analyzing the fluctuating light intensity signal incident on the photodiode. This approach relies on measuring the relative amplitudes of the  $2\omega$  and  $4\omega$  Fourier components of the signal, where  $\omega$  is the angular frequency of the rotating QWP in front of the analyzer [144, 150]. However, to fully measure the Stokes vector, the relative angle between the QWP fast axis (FA) and the analyzer transmission axis (TA) must be known for each period of rotation [143, 145, 147]. Williams [143] uses a phase-sensitive lock-in amplifier, and Arnoldt [147] an encoder wheel to measure this phase. We use a photo-interrupter and a timing disk attached to the rotating QWP. An Arduino microcontroller is used to perform the analysis, eliminating the need for expensive analysis devices as in Williams [143] (lock-in amplifier and digital voltmeter) and Arnoldt [147] (digital oscilloscope). The Arduino controller can also be interfaced with a computer via USB Serial connection to store time series of Stokes vectors.

The polarimeter presented here provides advantages in ease of use, functionality, portability, and cost over previous realizations [143–148]. Specifically, we combine the compact, hollow axle model airplane motor design of Bobach et al. [144] with a phase-sensitive measurement as in Williams [143] and Arnoldt [147]. These aspects, combined with the Arduino microcontroller to perform analysis, result in a device that is compact and rests on a single standard optical post, can completely measure the Stokes vector of any input polarization, and can communicate measurements to a computer. This chapter and the accompanying appendices describe the operating principles, construction, calibration,

and measurement accuracy and precision of the polarimeter.

## 4.2 Operating Theory

As described in Sec. 2.2, the polarization state of a beam of light can be formally described by the Stokes vector  $\mathbf{S} = [S_0, S_1, S_2, S_3]$ , where  $S_0 = I_X + I_Y$  is the Stokes parameter describing the total intensity,  $S_1 = I_X - I_Y$  the linear component,  $S_2 = I_D - I_A$  the diagonal component, and  $S_3 = I_R - I_L$  the circular component, where  $I_\beta$  with  $\beta = \{X, Y, D, A, R, L\}$  denotes the measured intensity of a given polarization [104]. The manipulation of the polarization by a series of optical elements can be described by the appropriate (4x4) Mueller matrices [107, 151, 152]. Figure 4.1(a) shows the elements of our system, namely a rotating waveplate of retardance  $\delta \approx \pi/2$  at angle  $\theta$ , followed by a stationary linear polarizer (the analyzer) at angle  $\alpha$  before the detector. The Mueller matrices for a linear polarizer at angle  $\alpha$  and a linear retarder (waveplate) of retardance  $\delta$  at angle  $\theta$  are given by [146, 148]

$$LP(\alpha) = \frac{1}{2} \begin{pmatrix} 1 & \cos(2\alpha) & \sin(2\alpha) & 0 \\ \cos(2\alpha) & \cos^2(2\alpha) & \cos(2\alpha) \sin(2\alpha) & 0 \\ \sin(2\alpha) & \cos(2\alpha) \sin(2\alpha) & \sin^2(2\alpha) & 0 \\ 0 & 0 & 0 & 0 \end{pmatrix}, \quad (4.1)$$

and

$$LR(\theta, \delta) = \begin{pmatrix} 1 & 0 & 0 & 0 \\ 0 & \cos^2(2\theta) \sin^2(2\theta) \cos(\delta) & \cos(2\theta) \sin(2\theta) (1 - \cos(\delta)) & \sin(2\theta) \sin(\delta) \\ 0 & \cos(2\theta) \cos(2\theta) (1 - \cos(\delta)) & \cos^2(2\theta) \sin^2(2\theta) \cos(\delta) & -\cos(2\theta) \sin(\delta) \\ 0 & -\sin(2\theta) \sin(\delta) & \cos(2\theta) \sin(\delta) & \cos(\delta) \end{pmatrix}, \quad (4.2)$$

respectively.

Operating these Mueller matrices representing the optical components on an arbitrary input Stokes vector  $\mathbf{S}_{in}$  as

$$\mathbf{S}_{out} = LP(\alpha) \cdot LR(\theta, \delta) \cdot \mathbf{S}_{in}, \quad (4.3)$$

one arrives at a general expression for the intensity signal detected by the photodiode given by [108, 143, 144, 149]<sup>1</sup>

$$I(\theta) = \frac{1}{2} [A + B \sin(2\theta) + C \cos(4\theta) + D \sin(4\theta)], \quad (4.4)$$

where  $\theta = \omega t + \phi$  is the orientation angle of the waveplate, with  $t$  representing time,  $\omega$  the angular frequency of rotation and  $\phi$  describing the phase offset. Allowing for an imperfect retardance of the waveplate ( $\delta \neq \pi/2$ ), the coefficients of the frequency components of Eq. 4.4 give the input Stokes parameters by the relations [143, 146–148]

$$S_0 = A - C / \tan^2(\delta/2), \quad (4.5a)$$

$$S_1 = C / \sin^2(\delta/2), \quad (4.5b)$$

$$S_2 = D / \sin^2(\delta/2), \quad (4.5c)$$

$$S_3 = B / \sin(\delta). \quad (4.5d)$$

The relationships of the coefficients in Eq. 4.4 to different frequency sinusoids means the Fourier transform provides a natural tool for determination of the Stokes vector. The linear components of the Stokes vector ( $S_1, S_2$ ) depend only on the  $4\omega$  part of the signal, while the circular component ( $S_3$ ) depends only on

<sup>1</sup>This intensity is exactly the first element  $S_0$  of the output Stokes vector  $\mathbf{S}_{out}$ .

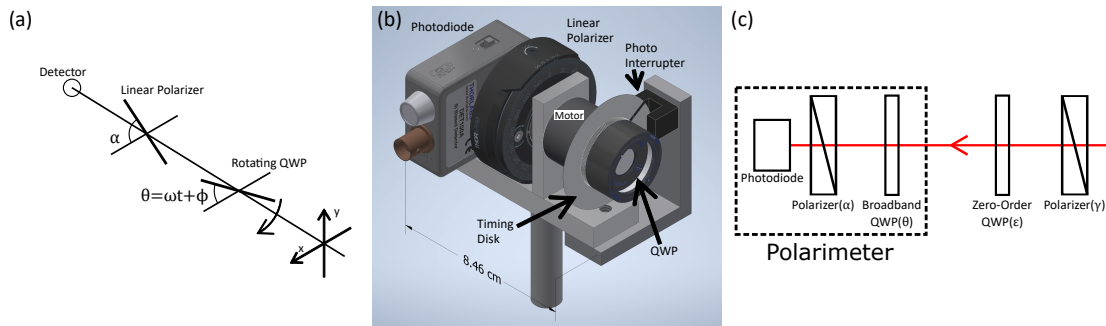


FIGURE 4.1: Measurement part of the polarimeter shown (a) schematically, and (b) as a 3-D image of the physical device. The QWP is mounted on a hollow axle motor with azimuth  $\theta = \omega t + \phi$ , where  $\omega$  is the angular frequency of rotation and  $\phi$  the phase offset, and  $\alpha$  is the azimuth of the linear polarizer (the analyzer). (c) The optical setup for calibration and characterization of the device. The upstream polarizer has azimuth  $\gamma$ , and the upstream QWP has azimuth  $\epsilon$ .

the  $2\omega$  part. Using this fact, one can easily determine the degree of linear or circular polarization of the light without knowing the phase of the signal, as in the implementation by Bobach et al. [144]. However, to measure the complete Stokes vector of the light, the components  $C$  and  $D$  must be separated, and thus the phase offset of the signal ( $\phi$ ) must be known [143, 145, 147].

The angle  $\phi$  determines the position of the FA of the QWP at the beginning of each period of rotation. In principal, the signal may be analyzed and the Stokes vector determined for any choice of analyzer angle  $\alpha$  and phase angle  $\phi$  [145]. However, situations where the analyzer does not lie in the desired measurement basis ( $\alpha \neq 0, \pi/2$ ), or the QWP FA is not parallel or perpendicular to the analyzer at the start of a new period ( $|\alpha - \phi| \neq 0, \pi/2$ ), lead to unnecessary complications in Eq. (4.4) and the subsequent Fourier analysis. Thus, we will limit ourselves to cases where  $\alpha = 0, \pi/2$  and  $|\alpha - \phi| = 0, \pi/2$ . The remaining choices of analyzer angle  $\alpha$  and QWP trigger angle  $\phi$ , of which there are four, affect the signs in Eq. (4.4). For  $\alpha = \phi = 0$ , Eq. 4.4 is the result, while for the choice  $\alpha = 0, \phi = \pi/2$  the second term becomes negative and the equation matches those found in [147] and [148]. In our current implementation we chose the case of Eq. (4.4) where  $\alpha = \phi = 0$ .

### 4.3 Device Description

Figure 4.1(b) shows a 3-D image of our experimental measurement apparatus (see Sec. D.1 for details about construction). As in the previous implementation by Bobach et al. [144] we mount the QWP on a model airplane motor with a hollow axle, which allows light to pass through the axle to the analyzer and detector. The device constructed by Bobach et al. [144] is only able to measure the degree of linearity vs. circularity of the light. To improve the functionality of our device we construct a trigger system similar to the encoder wheel system used by Arnoldt [147]. Attached to the rotating part of the motor we place a thin, circular metal timing disk with a slit cut out near the edge and a hole in the center. A photo-interrupter is positioned around the timing disk and produces a high signal each time the small slit passes through. The combination of the timing disk and the photo-interrupter serves as a trigger for the start of each period of rotation of the QWP.

Achieving the desired angle of the QWP FA when the trigger fires ( $\phi = 0$ ) requires a small amount of calibration of the device. For a known X-polarized input ( $\mathbf{S} = [1, 1, 0, 0]$ ), the longitude angle of the Stokes vector on the Poincaré sphere,  $2\psi = \arctan(S_2/S_1)$ , should be zero. We use the measured longitude as feedback for the calibration. The photo-interrupter is attached to a small piece of breadboard, which is secured to the vertical arm of the mount with two rubber bands. This arrangement allows for the photo-interrupter to move up and down. Shifting the position of the photo-interrupter up and down is analogous to changing the phase offset  $\phi$ , as the position of the photo-interrupter determines when the signal from the photo-interrupter will be high (i.e. the trigger fires). For X-polarized input light, setting the angle  $2\psi = (0 \pm 1)^\circ$  by changing the position of the photo-interrupter thus calibrates the device to the desired case of  $\phi = 0$  (see Sec. D.2 for procedure details).

The voltage signals from the photodiode and the photo-interrupter are sent to a small circuit board containing an Arduino Pro microcontroller for signal processing and analysis. The Arduino performs the fast Fourier transform (FFT), calculates the Stokes vector components, and displays the results on a small liquid crystal display (LCD). The Arduino can be connected to a computer via a USB Serial connection to store time series of Stokes vectors, which allows expanded functionality for various applications. For example, we use the device to calibrate a sequential pair of LCVRs. The circuit diagram, the Arduino code, and an example of LCVR calibration are included in the appendix Secs. B and D. The circuit diagram includes connections to power the motor with an electronic speed controller (ESC) and servo tester. The Arduino eliminates the need for expensive analysis components such as a lock-in amplifier [143] or digital oscilloscope [147].

The measurement head of the polarimeter shown in Fig. 4.1(b) measures about  $7 \times 9 \times 7$  cm, and is conveniently mounted on a single standard optical post. The analysis part of the device containing the Arduino controller and circuit are housed in a small plastic box measuring  $16 \times 16 \times 4$  cm. The two parts are connected by a single D-sub cable  $\sim 3$  m in length. Note that due to the pulse-width modulated current in the motor signal, it is necessary to isolate the motor wires from the rest of the wires in the cable to prevent electromagnetic interference. The setup is compact and can be easily placed anywhere on an optical table using a standard post holder.

## 4.4 Discussion

Accurate calibration and characterization of the device necessitates the production of known polarizations. To produce known polarization requires calibrated optics, which we obtain using a simplified version of the RLB method [145, 153], which uses rotation about the vertical axis of a mounting post for alignment of the azimuth of an optic to the vertical or horizontal axis. A  $180^\circ$  rotation of an optic around the vertical axis has no effect on the transmitted light intensity if the axis (FA or TA) is aligned either horizontally or vertical. Therefore, iterated vertical rotations combined with rotation of the optic in its mount lead to calibration of either the transmission axis of a polarizer or the fast axis of a wave plate. This method has the benefit of not relying on an already calibrated polarization optic as reference. An explicit description can be found in Appendix. C.

In principle, circularly polarized light can be produced with a polarizer and a QWP. In practice, however, the retardance  $\delta$  of a QWP depends on the wavelength  $\lambda$  of the light. Thus, we measure the retardance as a function of wavelength using the method of Wang et al. [154, 155] for two QWPs: one zero-order wave plate with nominal retardance  $\lambda/4$  at 915 nm, and one broadband wave plate with a specified operating range of 600-1200 nm. These data are shown in Fig. 4.2. The retardance of the zero-order wave plate has a linear dependence near  $\lambda = 915$  nm, and is measured to be truly quarter-wave ( $\delta = \pi/2$ ) at  $\lambda = 912.9340$  nm. This enables production of circularly polarized light at

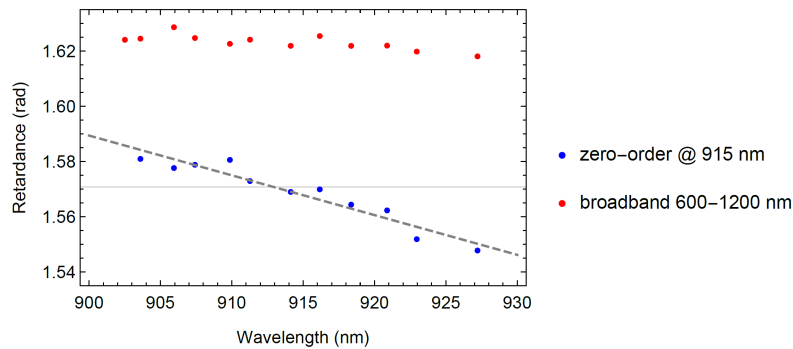


FIGURE 4.2: Quarter-wave plate (QWP) retardance measurements in a range around 915 nm for two QWPs: zero-order at 915 nm (blue), and broadband 600-1200 nm (red). The horizontal gray line represents the retardance value for an ideal QWP of  $\delta = \pi/2 \approx 1.57$  rad.



this wavelength. The retardance of the broadband wave plate has little dependence on wavelength over a 30 nm range around 915 nm, and we measure  $\delta = (0.5167 \pm 0.0008)\pi$  over that range. We use the broadband QWP in the polarimeter and use Eq. 4.5 to compensate for the imperfect retardance. This enables accurate measurements over a range of wavelengths fully covering our specific experimental application. This range could be expanded by measuring the retardance of the broadband QWP over a larger range and implementing wavelength selection within the Arduino software.

Figure 4.1(c) shows the optical setup used to evaluate the performance of the polarimeter. A calibrated linear polarizer at angle  $\gamma$  and the calibrated zero-order QWP at angle  $\varepsilon$  are placed upstream of the polarimeter to produce varying input polarizations. For all measurements described below, the wavelength of the input laser light was 912.9340 nm, corresponding to the measured  $\lambda/4$  value of the zero-order QWP. Figure 4.3(a) shows the voltage signal output by the photodiode and the trigger signal generated by the photo-interrupter for four input polarizations. Each case is labeled with the input polarization and the angles  $\gamma$  and  $\varepsilon$  used to produce it. For the X and Y inputs, the QWP was not in the

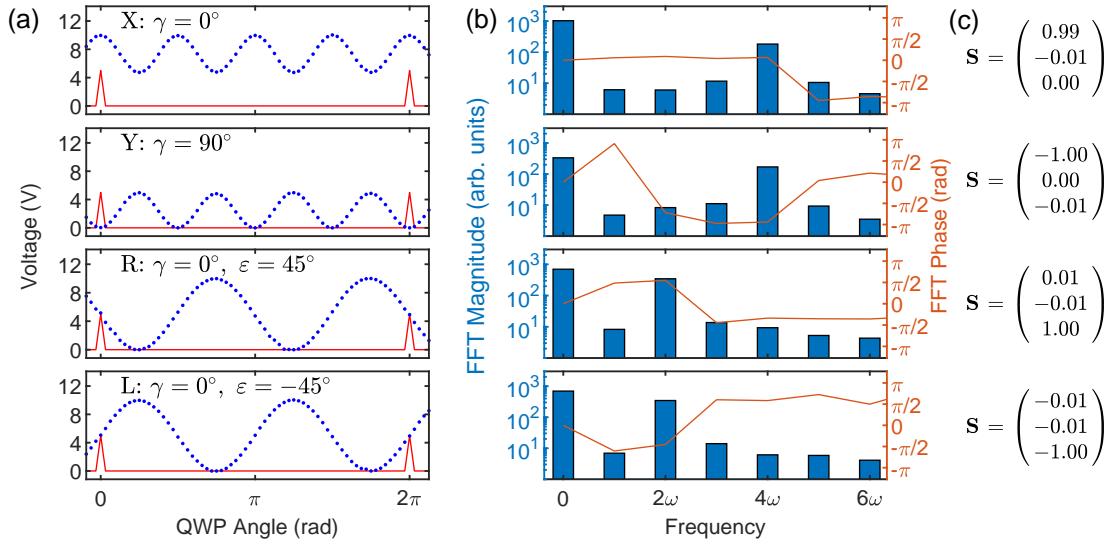


FIGURE 4.3: (a) Measured photodiode voltage (points) and trigger signal (line), (b) FFT magnitude and phase, and (c) calculated Stokes vectors for four input polarizations: X, Y, R, and L. The angular orientations of the upstream optics are noted in (a), with  $\gamma$  the angle of the polarizer and  $\varepsilon$  the angle of the zero-order QWP. These data were taken at a wavelength of 912.9340 nm, the measured  $\lambda/4$  value of the upstream QWP.

optical path. Figure 4.3(b) shows the calculated FFT magnitude and phase for the photodiode signal; note that the magnitude is plotted on a logarithmic scale. The linear cases (X, Y) show large  $4\omega$  components and the circular cases (R, L) show large  $2\omega$  components, both as expected. The phase of the  $4\omega$  component for X is near 0, while for Y it is near  $-\pi$ . The same  $\pi$  phase difference can be seen between the  $2\omega$  components of the circular cases (R, L). This shows explicitly how these polarizations are indistinguishable from each other without access to the phase information supplied by the photo-interrupter. Figure 4.3(c) shows the calculated Stokes vector for each polarization. Note that we omit  $S_0$  in the vector here as it is simply used to normalize the other components. The values are rounded in congruence with their appearance on our LCD. In each case, every component of the measured Stokes vector is within 1% of the expected value.

The Stokes vectors measured and reported in Fig. 4.3(c) show that the device is working properly for those specific input polarizations. To fully evaluate the device for all input polarizations we rotate the angles of our upstream optics (see Fig. 4.1(c)) and compare the measured angles of the Stokes vector on the Poincaré sphere with those expected. To evaluate linear polarizations we omit the zero-order QWP and rotate the polarizer angle  $\gamma$  while measuring the deviation from the expected value of the longitude angle  $2\psi$  defined previously. These data are shown in Fig. 4.4(a) with the mean of the data shown as a dashed red line and  $\pm 1$  standard deviation from the mean shown as a shaded

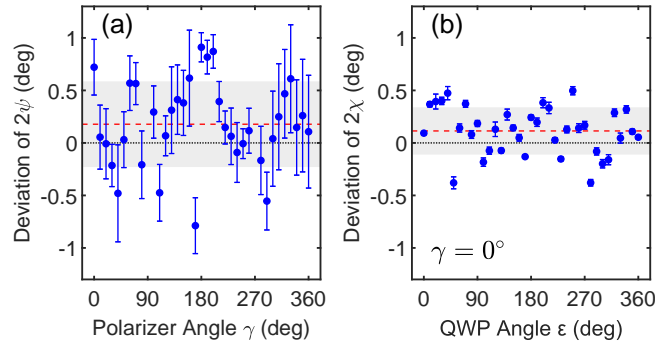


FIGURE 4.4: Deviation from expected value for (a) the longitude angle  $2\psi$  and (b) the elevation angle  $2\chi$  of the Stokes vector, when the upstream optics are rotated. In (a) the polarizer angle  $\gamma$  is rotated; in (b) the zero-order QWP angle  $\varepsilon$  is rotated. The dashed red line is the mean of the data, and the shaded region is  $\pm 1$  standard deviation from the mean.

region. The standard deviation is  $0.41^\circ$  and the mean is  $0.18^\circ$ , which is within half a standard deviation from zero. To evaluate linear, circular, and elliptical polarizations all in tandem we leave the polarizer at  $\gamma = 0^\circ$  while rotating the zero-order QWP angle  $\varepsilon$  and measuring the deviation from the expected value of the elevation angle  $2\chi = \arctan\left(S_3/\sqrt{S_1^2 + S_2^2}\right)$ . These data are shown in Fig. 4.4(b), with the same representation of the mean and standard deviation. Here we obtain a standard deviation of  $0.23^\circ$  and a mean of  $0.11^\circ$ , again within half a standard deviation from zero. Note the difference in the uncertainties of the individual measurements of the two angles (i.e., the error bars in Fig. 4.4). We attribute this difference to the differing dependencies of the angles on the frequency components of the intensity signal defined in Eqs. 4.4 and 4.5. Specifically, the longitude angle  $2\psi$  depends on the complex phase of the  $4\omega$  component, while the elevation angle  $2\chi$  depends on the relative magnitudes of the  $2\omega$  and  $4\omega$  components, which is more stable. The mean and standard deviation values measured here show quantitatively that the accuracy of the polarimeter is near that of commercially available devices. For example, the PAX1000 series of polarimeter from Thorlabs has a specified accuracy of  $\pm 0.25^\circ$ .

## 4.5 Conclusions

We report a self-contained polarimeter capable of fully characterizing the Stokes vector to within one degree on the Poincaré sphere. Our device provides accuracy comparable to the leading commercial devices for a fraction of the cost with smaller size and greater ease of use compared to previous non-commercial realizations [143–148]. By using a photo-interrupter as a trigger and an Arduino microcontroller to perform the analysis, we provide a compact, user-friendly, and cost effective way to quickly and accurately measure and record the polarization of collimated light.

In the context of the dissertation as a whole, this device provides the necessary capabilities in measurement of the polarization state of a laser beam. This allows production of known polarizations and calibration of polarization optical elements, as discussed in Sec. 3.1. The device also enables a quick and almost entirely automated way of calibrating a pair of LCVRs for detection polarization control, as outlined in Appendix B.

## Chapter 5

# Spin-selective AC Stark shifts on Charged Quantum Dots

This chapter describes the measurements performed demonstrating record large AC Stark shifts in a single negatively charged QD. These experiments use the techniques and setup described in Sec. 3.1. This includes extensive use of resonant photoluminescence excitation (RPLE) spectroscopy, along with the optical filtering scheme using volume Bragg gratings (VBGs) which is employed for all measurements. Several phenomena that emerge from the presence of the high-power AC Stark laser in the system are investigated, including dynamic nuclear polarization (DNP). The AC Stark shifts measured here have many promising applications in quantum computing, communication, and network protocols. The work detailing record large AC Stark shifts was published by Wilkinson et al. in Applied Physics Letters in 2019 [156], and the followup investigation into some of the emergent dynamics was published by Wilkinson et al. in proceedings of the SPIE Quantum Nanophotonic Materials, Devices, and Systems in 2019 [157].

### 5.1 Motivation

Quantum confined spins are regarded as potential candidates for quantum information applications [38, 158, 159]. The spin eigenstates could act as the two states of a qubit, and they can be manipulated and measured by magnetic and optical fields. In an epitaxially grown quantum dot (QD), the Zeeman splitting due to an external magnetic field is commonly used to control the selection rules of the optical transitions, and lasers can then control the spin in a variety of ways [43]. Depending on the magnetic field orientation the spin can be initialized

[44, 58], coherently manipulated [42, 45, 59], or measured via fluorescence [160]. Unfortunately, the magnetic field orientations necessary for coherent manipulation and measurement are orthogonal. Coherent manipulation requires a field transverse to the growth direction (Voigt configuration), while fluorescent measurement requires a field along the growth direction (Faraday configuration). The Voigt configuration lacks cycling transitions that preserve the spin [43, 58], which makes single-shot measurement of the spin state nearly impossible. The Faraday configuration lacks allowed optical transitions that link the spin manifolds [43], which precludes universal coherent optical manipulation of the spin orientation.

A potential solution for this impasse is to use the AC Stark effect to adjust the energy levels of the QD [37]. A strong, circularly polarized, far-detuned laser could apply a spin-selective energy shift. If this shift is significantly larger than the Zeeman splitting in a Voigt configuration, the system will convert to a pseudo-Faraday configuration [60], where the energy structure, eigenstates, and polarization selection rules are similar to those caused by a longitudinal magnetic field. The same reconfiguration could be accomplished in the field due to the local nuclear spins in the QD [45]. The reconfiguration depends on the power of the laser field, so it is reversible and it can be applied or removed rapidly over a few nanoseconds. That would allow switching between manipulation and measurement of an electron spin.

Here we experimentally demonstrate spin-selective AC Stark shifts applied to a charged QD in zero magnetic field. The transition frequency of one spin manifold shifts by more than 20 GHz, which is much larger than the 0.5 GHz linewidth, while the other transition is not shifted by the AC Stark effect. The polarization, power, and detuning of the laser causing the AC Stark effect determine the shifts of the transitions. Linear polarization shifts both transitions equally, while circular polarization shifts only one of them. Red-detuning of the laser causes a blue-shift of the transition, while blue-detuning causes a red-shift. In addition to the AC Stark shift, we observe another energy shift caused by dynamic polarization of the nuclear spins of the atoms comprising the QD. The direction of the nuclear polarization is determined by the polarization of the AC Stark laser.

Sec. 3.1 overviews the experimental setup and techniques used in these experiments.

## 5.2 Background and Theory

As outlined in Sec. 2.1, the energy structure of a negatively charged QD has four energy levels as shown in Fig. 5.1(a). The two lower levels are the spin projection eigenstates of a single trapped electron. The two upper states are the spin eigenstates of a negative trion: two electrons in a singlet state and one heavy hole [43]. Without an external magnetic field, there are two transitions allowed by conservation of angular momentum: one between the spin-up states, which form the spin-up manifold; and one between the spin-down states, which form the spin-down manifold. These are spin-preserving cycling transitions in that a cycle of excitation and spontaneous emission returns the system to the same spin state in which it started. The cycling transitions are labeled  $\sigma_+$  or  $\sigma_-$  by the angular momentum gained by the QD during excitation:  $\pm 1$ , measured along the growth direction. They correspond to circular polarization of the light.

As discussed in Sec. 2.3, the AC Stark shift occurs when a far off-resonant laser is applied to a transition in the regime where the magnitude of the detuning,  $\Delta = \omega_{\text{laser}} - \omega_{\text{QD}}$ , is much greater than the Rabi frequency of the interaction,  $\Omega = \vec{d} \cdot \vec{E}$  [60], where  $\vec{d}$  is the electric dipole moment of the transition and  $\vec{E}$  is the electric field of the laser. In that case, the excited states are only weakly populated to a degree  $\frac{\Omega}{2\Delta}$ <sup>1</sup>, and both the ground and excited states involved in the transition are shifted in opposite directions by  $\frac{\Omega^2}{4\Delta}$ . The different power dependencies of the excited state population and the resonance shift mean that if  $\Omega$  is

<sup>1</sup>Explicitly  $\frac{\Omega}{2\Delta}$  is the quantum probability amplitude of the excited state in the eigenstate  $|\uparrow\rangle = |\uparrow\rangle + \frac{\Omega}{2\Delta} |\uparrow\downarrow\uparrow\rangle$  induced by the AC Stark laser. Thus, the population is actually  $|\frac{\Omega}{2\Delta}|^2$ .

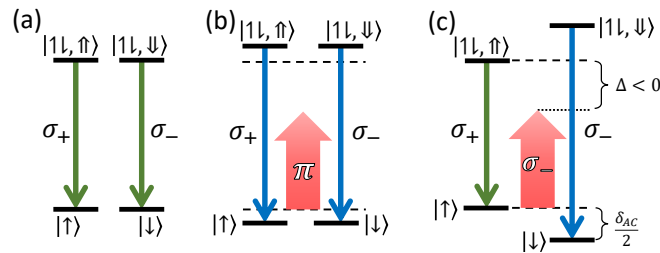


FIGURE 5.1: Charged quantum dot energy levels and allowed transitions for zero magnetic field and (a) no AC Stark laser, (b) a red-detuned, linearly polarized AC Stark laser, and (c) a red-detuned,  $\sigma_-$  polarized AC Stark laser.  $\Delta$  is the detuning of the AC Stark laser from the QD resonance, and  $\delta_{\text{AC}}$  is the induced AC Stark shift of the  $\sigma_-$  transition.

large and  $\Delta \gg \Omega$ , then the shift can be large even while the excited population is small. The shifts of both states move the resonance frequency by  $\delta_{\text{AC}} = \frac{-\Omega^2}{2\Delta}$ , which is the AC Stark shift we measure in the excitation spectra below. When the laser is red-detuned ( $\Delta < 0$ ) the AC Stark effect causes a blue-shift; when the laser is blue-detuned ( $\Delta > 0$ ) it causes a red-shift. Figure 5.1(b) shows the expected AC Stark shifts for a red-detuned, linearly polarized laser. Both spin manifolds are affected because linear polarization is a superposition of  $\sigma_+$  and  $\sigma_-$  light. Figure 5.1(c) shows the expected AC Stark shifts for a red-detuned,  $\sigma_-$  polarized laser. Only the co-polarized ( $\sigma_-$ ) spin manifold is shifted by the AC Stark effect, as the transition dipole of the other ( $\sigma_+$ ) spin manifold is orthogonal to the incident laser light, i.e.  $\Omega_+ = \vec{d}_+ \cdot \vec{E} = 0$ . Thus for equivalent laser detuning and power, the shift for circular light is twice the magnitude of that for linear.

## 5.3 Results and Discussion

### 5.3.1 Excitation Spectra

We measured the resonant excitation spectrum of the QD in zero external magnetic field without the AC Stark laser to obtain a reference against which to compare the spectra under the influence of the AC Stark laser. The reference spectrum is shown in Fig. 5.2(a) and zero detuning of the resonant laser ( $\delta = 0$ ) is defined as 323076 GHz, which is the center frequency of the emission peak. There are two degenerate transitions with linewidths of 0.48 GHz in the reference spectrum, one for each spin manifold. We then measured excitation spectra while applying a linearly or circularly polarized AC Stark laser with a red-detuning of  $\Delta/2\pi = -1000$  GHz and a power density of 77.3 kW/cm<sup>2</sup> (total power 2.38 mW). The linear polarization shifts both transitions equally so they remain degenerate, as shown in Fig. 5.2(b). The circular polarization shifts one transition to higher energy by a large amount while the other transition remains near the reference frequency, as shown in Fig. 5.2(c). The lower-energy transition is actually red-shifted and broadened slightly due to interactions with the partially polarized nuclear spin ensemble of the atoms comprising the QD. This is called the Overhauser shift and is explained in greater detail below. Note that

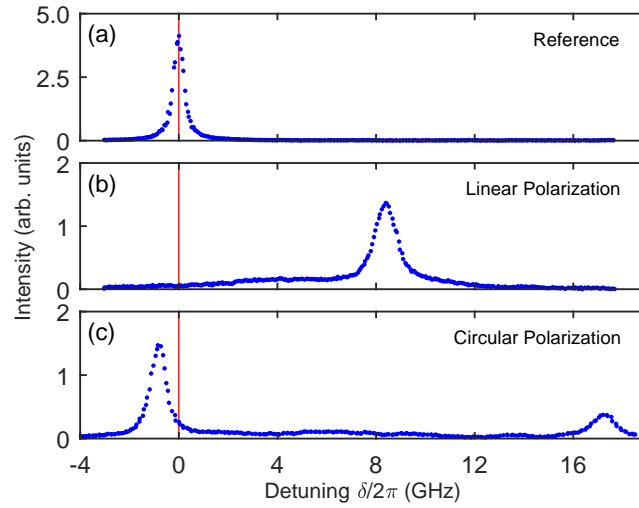


FIGURE 5.2: Excitation spectra as functions of the resonant laser detuning,  $\delta$ . (a) Reference spectrum with no AC Stark laser. (b) Spectrum with linearly polarized ( $\pi_y$ ) AC Stark laser. (c) Spectrum with circularly polarized ( $\sigma_-$ ) AC Stark laser. For these measurements, the detection polarization was linear ( $\pi_x$ ), the detuning of the AC Stark laser was  $\Delta/2\pi = -1000$  GHz, and the power density was  $77.3 \text{ kW/cm}^2$  (2.38 mW).

the non-constant background seen in Figs. 5.2(b,c) is due to a small amount of fluorescence from a different nearby QD.

### 5.3.2 Red- and Blue-Detunings

Figure 5.3 shows the center frequencies of the peaks in the excitation spectra as functions of the AC Stark laser power density. The power densities were calculated by dividing the power applied to the sample by the area of the focused beam on the sample surface. The frequency shifts for both linear and circular polarization can be seen for both red- and blue-detuning of the AC Stark laser. All the shifts are linear in the power density of the AC Stark laser, as expected, because  $\Omega^2 \propto \text{power}$ . For linear polarization and red-detuning of the AC Stark laser, both transitions are shifted to higher frequency by the same amount; for blue-detuning both are shifted to lower frequency. For circular polarization and red-detuning, one transition is shifted to higher frequency by the combination of AC Stark effect and Overhauser field, while the other is shifted to lower frequency by the Overhauser field alone. For blue-detuning, both transitions are shifted to lower frequency, one by just the Overhauser field (as with



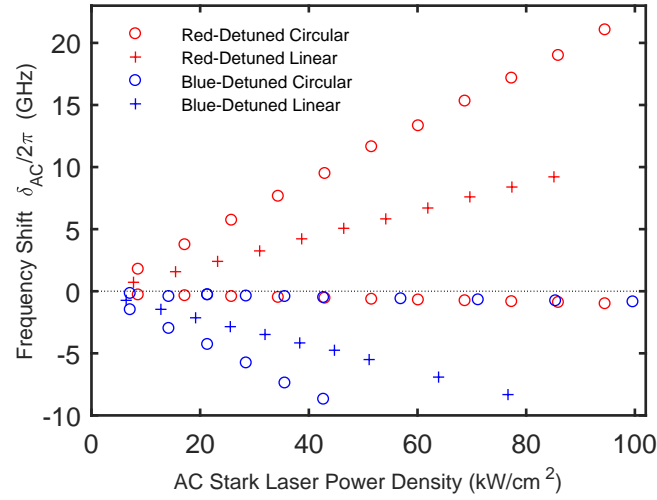


FIGURE 5.3: Frequency shifts of excitation spectra peaks as functions of the AC Stark laser power for red- or blue-detuning ( $\Delta/2\pi = \pm 1000$  GHz), and linear or circular polarization.

red-detuning) and one by the combination of the AC Stark effect and the Overhauser field whose shifts are in opposition. Thus a blue-detuned AC Stark laser does not shift the affected spin manifold by as much as a red-detuned AC Stark laser. Regardless of the sign of the detuning of the AC Stark laser, the Overhauser shifts are in the same direction by the same amount. That is conclusive evidence that the observed shift is not due directly to the AC Stark effect, whose polarity would change sign with the detuning. The direction of the shift is consistent with the Overhauser effect expected due to dynamic nuclear polarization caused by electron spin pumping. However, we cannot rule out the possibility of other mechanisms, such as absorption by the tail of the wetting layer and subsequent trapping of spin-polarized carriers by the QD.

### 5.3.3 Dynamic Nuclear Polarization

Figure 5.2(c) shows the excitation spectrum with a  $\sigma_-$  AC Stark laser applied. In this case the  $\sigma_-$  ( $\sigma_+$ ) transition is blue- (red-) shifted from the reference frequency. The difference in the peak heights seen here means that the trapped electron has a non-zero time-averaged spin polarization, which increases fluorescence from the  $\sigma_+$  transition. This implies that the electron spin is being pumped into the spin-up manifold. The exact mechanism of this spin pumping is not known at this time, but will be the subject of future investigations. We note

that it is likely not due to the forbidden transition downward from the  $|\uparrow\downarrow, \downarrow\rangle$  trion state being weakly populated by the AC Stark laser, as the magnitude of the Overhauser shift seen in Fig. 5.3 is the same for both red- and blue-detuning. If this forbidden transition were the source of spin pumping we would expect to see a larger Overhauser shift with blue-detuning due to the incoherent excitation of the trion state via phonon coupling, as mentioned earlier. One possibility for the spin pumping mechanism is a process similar to that in Ref. [161] where excitation of a forbidden transition is accompanied by a simultaneous spin flip of the electron and one of the nuclear spins. In this case the forbidden transition might be off-resonantly excited by the strong AC Stark laser. This process would result in the trapped electron spin being pumped into the spin-up manifold, consistent with the difference in the peak heights of Fig. 5.2(c).

Figure 5.4(a) shows a spatial diagram of a QD including the trapped electron and some nuclear spins. The time-averaged electron spin polarization is transferred to the nuclear spins by the contact hyperfine interaction [162]. The

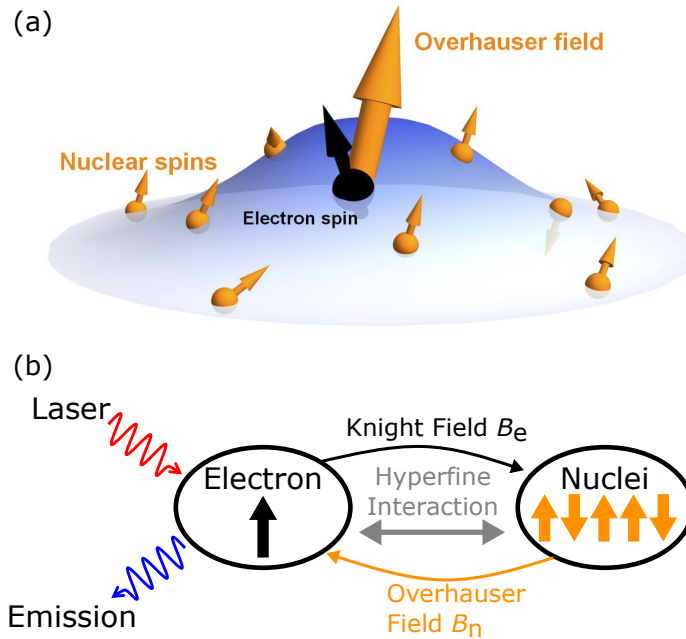


FIGURE 5.4: (a) Spatial diagram of a QD showing nuclear spins and the trapped electron spin. The small orange arrows represent nuclear spins, the central black arrow represents the spin of a trapped electron, and the large orange arrow the Overhauser field induced by the polarized nuclear spins. (b) Process of dynamic nuclear polarization (DNP).

result is that the nuclear spin ensemble acquires a non-zero time- and ensemble-averaged polarization in the +z direction:  $\langle I_z \rangle > 0$ . This average polarization leads to an overall magnetic field known as the Overhauser field, and represented in Fig. 5.4(a) by the large orange arrow. The polarization of the nuclear spins causes an Overhauser shift of the electron spin-states, which shifts the frequencies of the two optical transitions. This process is referred to as dynamic nuclear polarization, and an overview is shown in Fig. 5.4. The spin-down (-up) electron state  $|\downarrow\rangle$  ( $|\uparrow\rangle$ ) is shifted to lower (higher) energies, leading to an overall blue- (red-) shift of the  $\sigma_-$  ( $\sigma_+$ ) transition. The hole states remain un-shifted, as the hyperfine interaction is suppressed due to the  $p$  orbital symmetry of the top of the valence band [44]. Note that the directions of the Overhauser shifts depend only on the polarization of the AC Stark laser—not its detuning—whereas the AC Stark shifts depend on both the detuning and polarization of the laser. With a red-detuned, circularly polarized AC Stark laser, the Overhauser shift of the higher-frequency transition is in the same direction as the AC Stark shift, while the lower-frequency transition is shifted to lower frequency. With a blue-detuned AC Stark laser of the same polarization, the Overhauser shift is in the opposite direction from the AC Stark shift. In both cases, the transition unaffected by the AC Stark shift is shifted to lower frequency by the Overhauser shift. The magnitude of the Overhauser shifts observed here in the range of 0.1–0.5 GHz are comparable to those previously seen in the literature [161, 163–167], and likely correspond to a degree of nuclear polarization of  $\sim 1 - 10\%$  [163–165].

### 5.3.4 Spin-Selective Polarization Control

We can change the degree to which each transition shifts by changing the polarization of the AC Stark laser. Figure 5.5 shows the peak center frequencies as a function of the polarization of the AC Stark laser. For these measurements the laser power density was  $84.4 \text{ kW/cm}^2$  and it was red-detuned with  $\Delta/2\pi = -1000 \text{ GHz}$ . For each AC Stark laser polarization, two excitation spectra were recorded, one with  $\sigma_-$  detection and one with  $\sigma_+$  detection. The detection polarization in turn determines which transition energy was measured. For linear laser polarization the transitions are nearly degenerate and blue-shifted

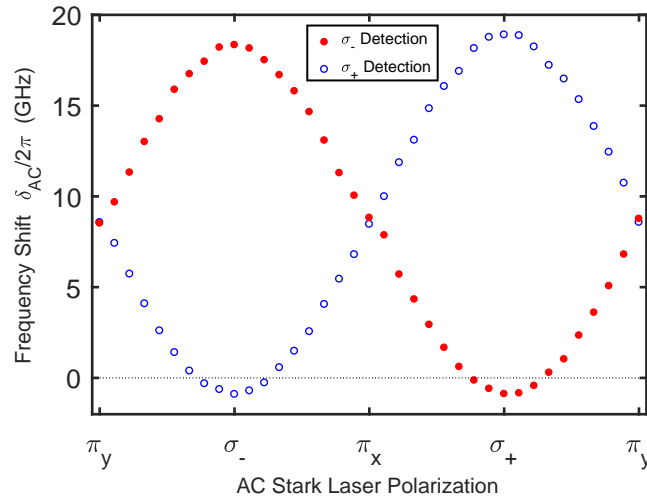


FIGURE 5.5: Frequency shifts of excitation spectra peaks as a function of AC Stark laser polarization using orthogonal circular detection polarizations. The detuning of the AC Stark laser was  $\Delta/2\pi = -1000$  GHz and the power density was  $84.4 \text{ kW/cm}^2$  for these measurements.

from the reference frequency, as expected. As the laser becomes elliptically polarized the transitions split because the AC Stark effect influences them differently (recall that  $\Omega_{\pm} = \vec{d}_{\pm} \cdot \vec{E}$ ), which also causes electron spin pumping. The polarization of the electron spin causes dynamic nuclear polarization, and the Overhauser shift occurs. This is most obvious for circular polarization where the splitting is largest. In this case the lower-frequency transition is red-shifted by the Overhauser effect to below the reference frequency. The occurrence of the maximum splitting under circular polarization implies that the transition dipoles are highly circularly polarized. We have confirmed this with a calculation for the degree of circular polarization for the  $\sigma_-$  ( $\sigma_+$ ) transition of 0.963 (0.955).

### 5.3.5 Low-Power AC Stark Regime

Lines of best fit for the data shown in Fig. 5.3 do not intersect zero AC Stark shift at zero applied AC Stark laser power. This indicates that the observed behavior is not well characterized by a linear relationship for all powers, i.e. there are two regimes: high power where the shift dependence on power is linear as expected, and low power where multiple processes may be competing to cause non-linear

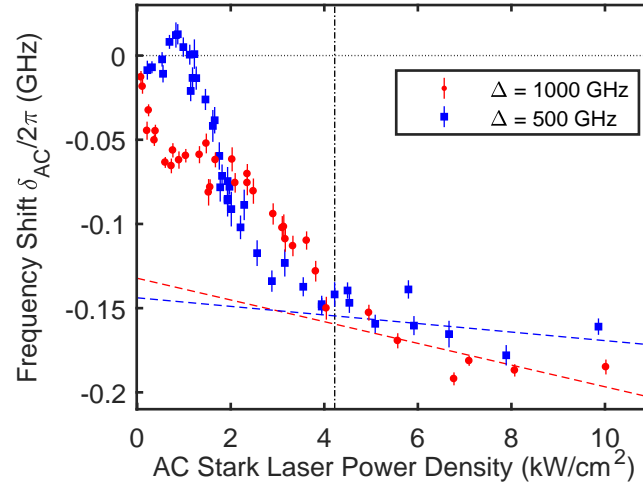


FIGURE 5.6: Low power frequency shifts of the Overhauser shifted ( $\sigma_+$ ) peak as a function of AC Stark laser power density. The red circles (blue squares) are for detuning  $\Delta/2\pi = 1000$  ( $\Delta/2\pi = 500$ ) GHz, and a circularly ( $\sigma_-$ ) polarized AC Stark laser.

dependence. All previous data and discussion has been concerning the linear high power regime. In this section we will discuss the low power regime.

Figure 5.6 shows the center frequencies of only the Overhauser-shifted ( $\sigma_+$ ) peak as a function of the AC Stark laser power density for two values of detuning  $\Delta$ , and a single circular ( $\sigma_-$ ) polarization (of the AC Stark laser). The Overhauser-shifted peak provides a means to isolate the Overhauser shift from the AC Stark shift as the AC Stark laser has no direct interaction with this transition. Note that the AC Stark laser power densities used here are approximately an order of magnitude less than those in Fig. 5.3. The black dashed-dotted line indicates the qualitative (defined simply by inspection) cutoff for where the behavior is no longer linear ( $P_{\text{cutoff}} = 4.2 \text{ kW/cm}^2$ ). The red (blue) dashed lines are linear fits for all data points to the right of the defined cutoff power with a detuning of  $\Delta/2\pi = 1000$  ( $\Delta/2\pi = 500$ ) GHz. These fits show explicitly how the trend from the linear (high power) regime does not intersect zero shift at zero applied power. At power densities lower than the cutoff an oscillatory behavior between the two different detunings can be seen. This implies that the Overhauser shift, and therefore the electron spin pumping caused by the AC Stark laser has dependence on detuning, which is to be expected. Further investigations into the low power regime (more detunings and powers) will provide more insight into the nature of the mechanism causing the observed DNP.

### 5.3.6 Linewidth Analysis

The full-width half-max linewidth (FWHM) of an optically active atomic or QD transition provides information about any processes that broaden the line from its transform-limited value. Thus to further characterize the nature of the Overhauser shift induced by DNP we perform an analysis on the linewidths of the QD transitions. In this case rather than comparing against the transform limited value, we compare AC Stark scans to reference scans where there is no AC Stark laser present. We perform this analysis for a red-detuned ( $\Delta/2\pi = 1000$  GHz) AC Stark laser, i.e. all of the peaks represented by the red points in Fig. 5.3. Figures 5.7(a) and 5.7(b) show these linewidths for a circularly ( $\sigma_-$ ) polarized, and linearly ( $\pi_y$ ) polarized AC Stark laser, respectively. The black dotted line shows the mean of the linewidths for all reference scans, while the gray shaded area indicates  $\pm 1$  standard deviation from the mean. There are two sets of data points when the AC Stark laser is circularly polarized because the two transitions are split, with one blue-shifted by the AC Stark laser and the other red-shifted by the Overhauser effect. There is only one set for the linear case as the transitions remain degenerate, and both are blue-shifted (Figs. 5.1 and 5.2). The color of the data points corresponds to the direction in which the transition is shifted.

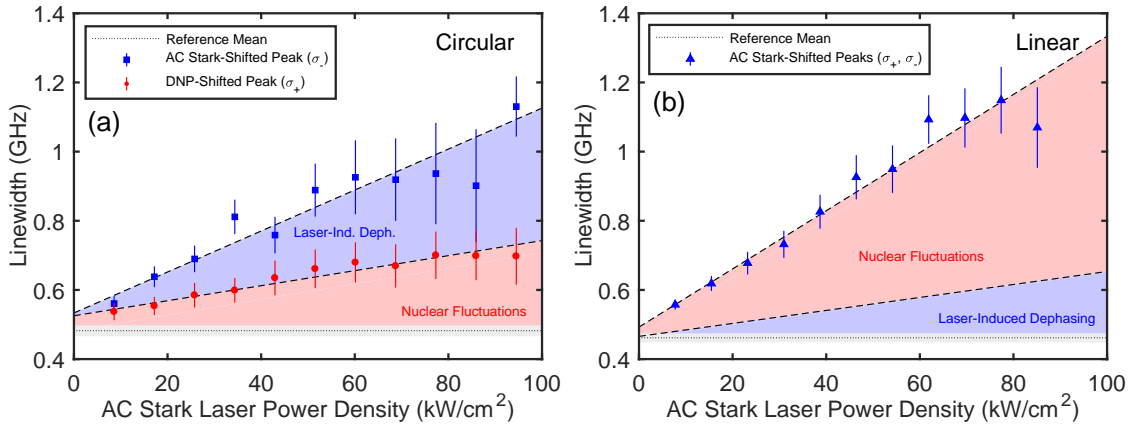


FIGURE 5.7: QD transition linewidths as functions of AC Stark laser power density for red-detuning ( $\Delta/2\pi = 1000$  GHz), with (a)  $\sigma_-$  and (b)  $\pi_y$  polarizations. Contributions to the line broadening for laser-induced dephasing and nuclear spin fluctuations are indicated by the blue and red shaded regions, respectively. Blue points represent a blue-shifted transition, and red points represent a red-shift.

In general, there are many processes that may change the linewidth of the transition from the reference value when the AC Stark laser is applied. This high-power AC Stark laser introduces a strong oscillating electric field to the local environment surrounding the QD, which likely changes the effective local charge density in a time-dependent manner. This time-dependent charge density may induce spectral diffusion and broaden the line by changing the occupation of defects that act as charge traps [96, 168–170], or by affecting charge buildup at material interfaces [109], as two possible examples. However, these processes likely result in effects that are small compared to those resulting from laser-induced dephasing<sup>2</sup> and changes in nuclear spin bath fluctuations. Therefore, we consider here only laser-induced dephasing and nuclear spin noise induced by the application of the AC Stark laser.

Laser-induced dephasing is a coherent effect caused by the AC Stark laser that broadens the linewidth [172, 174]. The presence of the AC Stark laser can also affect the nuclear spin environment of the atoms that make up the QD, which in turn affects the linewidth of the transition. Nuclear spin noise is akin to spectral diffusion and is therefore a stochastic process, whereas laser-induced dephasing is a coherent effect. This key difference between the two processes allows us to isolate the effect of each on the transition linewidths. As a coherent effect, laser-induced dephasing depends directly on the Rabi frequency of the interaction,  $\Omega_{\pm} = \vec{d}_{\pm} \cdot \vec{E}$ . In the case of the DNP-shifted peak ( $\sigma_{+}$ ) under an oppositely ( $\sigma_{-}$ ) polarized AC Stark laser the Rabi frequency is exactly zero as the dipole moment of the transition and the electric field polarization are orthogonal, explicitly this reads  $\Omega_{+} = \vec{d}_{+} \cdot \vec{E}_{-} = 0$ . Thus the red dots in Fig. 5.7(a) can only be influenced by a change in nuclear spin fluctuations, as indicated on the plot by the red shaded region below the linear fit of the points. Subtracting the nuclear spin noise from the AC Stark shifted peak ( $\sigma_{-}$ ) reveals the portion of line broadening induced by the laser-induced dephasing. Because linear polarization is a superposition of equal parts  $\sigma_{+}$  and  $\sigma_{-}$  light, the Rabi frequency for each transition under linear AC Stark should be half as much as that for the circularly polarized case. Other than this key difference the effect is exactly equivalent to the circular. Therefore we plot in Fig. 5.7(b) half the measured laser-induced dephasing from the circular case. Subtraction yields the

---

<sup>2</sup>This effect is often referred to as excitation induced dephasing (EID) [171–173]. However, the AC Stark laser only excites the states to a small degree  $\frac{\Omega}{2\Delta}$ , so we replace "excitation" with "laser" for this specific context.

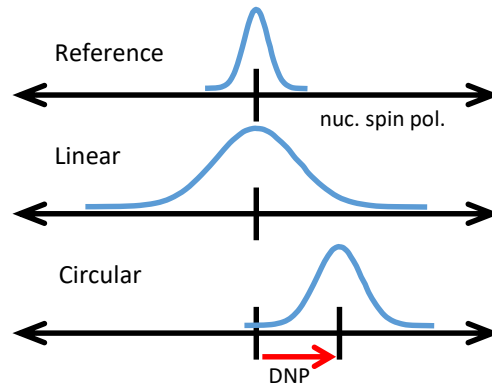


FIGURE 5.8: Schematic illustrating the difference in nuclear spin noise for the reference, linear, and circular.

corresponding nuclear spin fluctuations for a linear AC Stark laser.

Figure 5.7 shows that the nuclear spin fluctuations are much larger under a linearly ( $\pi_y$ ) polarized AC Stark laser than for a circularly ( $\sigma_-$ ) polarized laser, and in both cases the fluctuations are larger than for the reference when no AC Stark laser is applied. Figure 5.8 illustrates these differences on a nuclear spin polarization axis. The reference scan has the narrowest distribution, and is centered at zero nuclear spin polarization. The polarization remains centered around zero for a linear AC Stark laser, however the distribution of the ensemble is significantly broadened from the reference. Under circular polarization the distribution is no longer centered at zero because the nuclear spin bath becomes partially polarized via DNP, as indicated on the schematic by the red arrow labeled DNP. In this case the width of the distribution is less than the linear case, but still larger than for the reference spectrum. It is also possible that this distribution is asymmetric. This implies that polarizing the nuclear spin ensemble via a circularly polarized AC Stark laser reduces fluctuations in comparison to a linearly polarized laser.

## 5.4 Conclusions

We have demonstrated that spin-selective AC Stark shifts can be induced in a charged quantum dot using a strong, circularly polarized, far-detuned laser. We achieved a maximum splitting of approximately 20 GHz between the two spin-preserving transitions, which is large compared to the optical linewidth of about 0.5 GHz. The magnitude of the shift is in practice limited only by the amount of



laser power that can be delivered to the QD while still discriminating the scattering from the fluorescence. We have optimized the efficiency of the optical path and the focus of the laser beam to maximize the shift achieved in this particular realization. The laser causing the shifts is red-detuned far enough that on its own it does not produce sufficient fluorescence to be measured above the noise background. However, the observed difference in peak heights implies that the AC Stark laser causes pumping of the electron spin. The electron spin polarization in turn causes nuclear polarization and an Overhauser field along the growth direction. Low power scans show that the shift dependence on AC Stark power is not linear for all powers and depends on the detuning. Analysis of the transition linewidths reveals larger nuclear spin noise for a linearly polarized AC Stark laser than for a circularly polarized AC Stark laser.

The AC Stark shift achieved here is in principle sufficient to change the selection rules from the Voigt configuration of a small in-plane magnetic field to a pseudo-Faraday configuration with spin-preserving cycling transitions [60]. The capability to rapidly and coherently reconfigure the energy structure and polarization selection rules of a charged QD enables a number of innovative measurements. For example, it would allow measurements of electron and nuclear spin properties in zero magnetic field. It is also possible that the enhanced spin state splitting caused by the effect could protect the electron spin from magnetically induced dephasing [175]. In a larger context, the capability of switching between Voigt and Faraday configurations will allow the quantum optics research community to investigate more complex control and manipulation sequences for single-qubit operations. Some potential applications for this have already been proposed and include generation of a cluster state [176], quantum repeaters [177], and control of the dark exciton occupation [178].

## Chapter 6

# Summary and Outlook

In this dissertation, I have presented several accomplishments in characterizing and coherently manipulating the energy level structure of self-assembled semiconductor QDs. Demonstration of record large AC Stark shifts to the energy level structure of a single negatively charged InGaAs QD was presented. Some of the dynamics that emerged from application of the high-power AC Stark laser to the system such as dynamic nuclear polarization, and low-power behavior were investigated as well. This work was facilitated by the construction of a rotating-waveplate polarimeter device to accurately measure the polarization state of a laser beam, along with the design of a novel optical filtering scheme using volume Bragg gratings (VBGs). Additionally, a method of automated spectroscopy of single QDs has been shown to work at a proof-of-concept level. These achievements will enable useful future applications in the long-term dream of using QDs as a node in real-world quantum networks.

In Sec. 3.2 I overviewed the development of an automated spectroscopy program to characterize the properties of many individual QDs. Photoluminescence (PL) from single QDs can be automatically coupled into a single mode fiber for spectroscopy. The most efficient sampling path between all dots of interest is calculated using a traveling salesman genetic algorithm. High-resolution emission spectra are acquired using a scanning Fabry-Perot (SFP) in tandem with a spectrometer. The signal to noise ration (SNR) of the emission spectra is poor due to the low transmission efficiency of the SFP. Use of a virtually imaged phased array [137, 138] in combination with a spectrometer should enable acquisition of emission spectra with a far superior SNR. Overall, this work shows at a proof-of-principle level that high-resolution emission spectra can be automatically measured for many QDs in one field of view (FOV). Appendix A describes an automatic image focusing method that will be used

in combination with feature recognition to expand the sampling area to many FOVs.

In chapter 4 I described the operating principle, design, construction, and evaluation of a rotating-waveplate polarimeter device to measure the polarization state of a laser beam. The device employs an Arduino microcontroller to perform the Fourier transform of the detected intensity signal from a photodiode after a rotating quarter-wave plate in front of a linear polarizer. The device measures the Stokes vector and Poincaré sphere angles with accuracy comparable to that of commercially available devices. This device has large applicability in any optics lab and has seen widespread use in our lab, as outlined throughout the dissertation.

In Sec. 3.1 I overviewed the novel filtering scheme used to discriminate the strong AC Stark laser from the weak QD PL. This scheme utilized VBGs and enabled the experiments I presented in chapter 5 showing record large AC Stark shifts in a charged QD. The induced AC Stark shifts allow for a spin-selective and rapid reconfiguration of the energy level structure of a QD. In principle, this reconfiguration allows for a single-shot readout of a single electron spin trapped in a QD under a small applied transverse magnetic field [60]. The technique of manipulating the energy levels of a QD with the AC Stark shift can also potentially make feasible many of other useful protocols including generation of a cluster state [176], quantum repeaters [177], and control of the dark exciton occupation [178].

The work presented here on characterization and manipulation of the energy level structure of single semiconductor QDs serves as the first step on the way towards many potentially fruitful long term goals. Automatic spectroscopic characterization of many QDs will increase the efficiency and throughput of device fabrication. Rapid energy level reconfiguration via spin-selective AC Stark shifts applied to a QD can enable a multitude of schema relevant to quantum communication, computing, and networking.

## Appendix A

# Automatic Focusing of Imaging System

The stack of piezo-actuated inertial translation stages used for movement of the sample beneath the imaging system (Fig. 3.10) ideally provides independent movement in each axis  $x$ ,  $y$ ,  $z$ . However, in practice a small amount is moved in each of the two nominally "stationary" axes each time the third axis is targeted to move. While this amount is small<sup>1</sup> and insignificant over any single movement, many movements and movements larger than one field of view (FOV) to other regions of the sample will affect the  $z$ -axis position enough to defocus the image. Left uncompensated, this effect would make sampling QDs from more than one field of view intractable, and thus largely limit the amount of QDs that could be sampled automatically. To remedy this effect an automatic-focusing routine was developed based on image gradients. Figure A.1 shows the methodology of this approach. Images are taken over a range of  $z$ -positions covering close to double the depth of focus. For each image the QD positions are found and the gradient of the fluorescence intensity in a  $20 \times 20$  pixel grid around each dot is calculated. The magnitude of the gradient is taken and then summed over the  $20 \times 20$  grid to compute a "QD gradient sum". For each QD, the QD gradient sum is plotted against the  $z$ -position of the image. An example of these data for a subset of the QDs in the images are shown in the lower portion of Fig. A.1. The gradient is indicative of the slope, or more colloquially the "sharpness", of the image, and therefore a maximum of the gradient indicates the position of optimal focus. The  $z$ -position of maximum gradient for each dot is found, and averaging these together results in the focus position indicated by the red dotted vertical line in the plot. This method allows for the automatic focusing of

---

<sup>1</sup><1% of the specified movement of the targeted axis.

the image field assuming that the z-position starts reasonably close to the focus. This method combined with feature recognition will expand the automatic spectroscopy capabilities outlined in Sec. 3.2 to upwards of 80 FOVs.

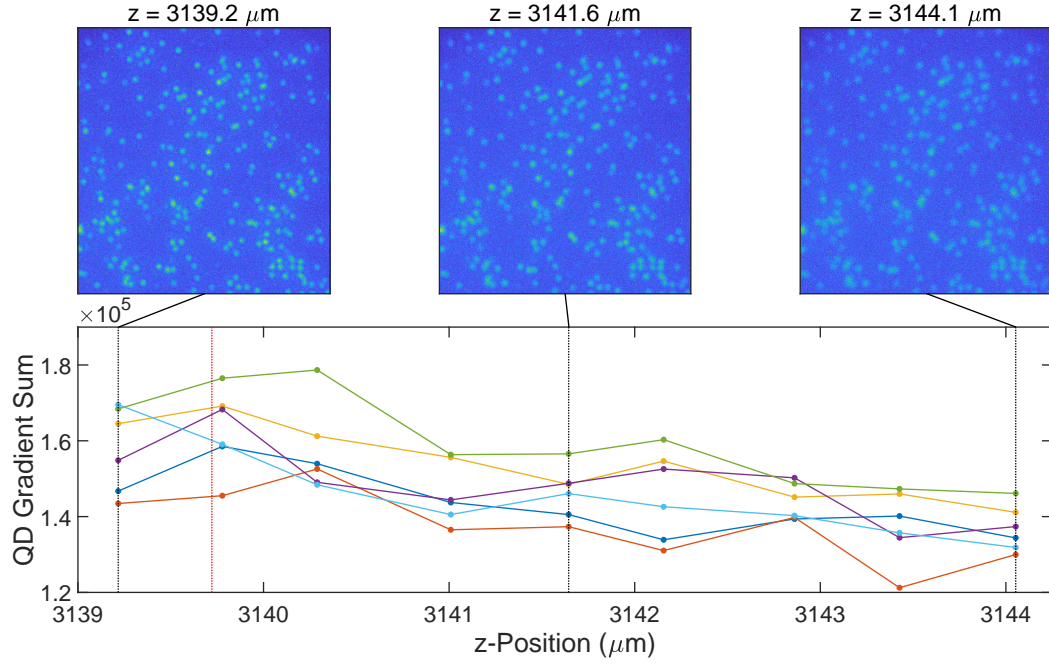


FIGURE A.1: Automatic focusing of image system methodology. Each point-line color corresponds to an individual dot. Six QD gradients sums are show here, however more (usually around 15-20) are used to compute the focus. For this example the focus is determined to be at  $z = 3139.70 \pm 0.73 \mu\text{m}$ .

## Appendix B

# Calibration of Liquid Crystal Variable Retarders (LCVRs)

We use the computer interface enabled by the Arduino board of the polarimeter device described in Chap. 4 to calibrate a pair of sequential LCVRs. As described in Sec. 3.1 we use the LCVRs to make polarization-sensitive measurements of fluorescence emitted by QDs. In the collection path between the sample and the LCVRs there are many optical elements like mirrors and lenses that have unintentional effects on the polarization. The result is that emission of a certain polarization ends up with a different polarization when it reaches the LCVRs. The purpose of this calibration procedure is to find settings of the LCVRs that enable measurements equivalent to measuring the polarization at the location of the sample. The optical setup for this calibration procedure is shown in Fig. B.1.

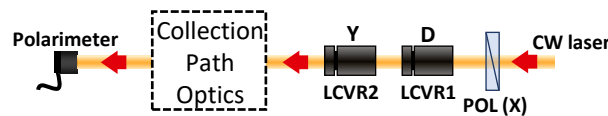


FIGURE B.1: Setup for calibration of the LCVRs using the polarimeter.

We direct a collimated beam backwards through our collection path to the polarimeter, which is placed directly in front of the sample. The reversibility of the effect of the polarization changes allows us to calibrate the LCVRs by setting the LCVR voltage values such that the polarimeter measures the desired polarization (X, Y, D, etc.). The desired polarizations can be specified by different combinations of only two parameters of the Stokes vector in the Poincaré sphere:

the longitude angle  $2\psi$  and the elevation angle  $2\chi$ . These values are shown in the Table B.1.

Polarization	Longitude Angle ( $2\psi$ )	Elevation Angle ( $2\chi$ )
X	0	0
Y	$\pm\pi$	0
D	$\pi/2$	0
A	$-\pi/2$	0
R		$\pi/2$
L		$-\pi/2$

TABLE B.1: Poincaré sphere angles for the 6 polarizations used to calibrate the LCVRs.

The circular polarizations (R, L) can be fully specified by the elevation angle alone, while the linear polarizations each require a certain value of longitude angle and 0 elevation angle. To begin, we take an automated scan of the entire voltage range of both LCVRs while recording the Stokes parameters via USB serial interface between the polarimeter and a computer. Shown in Fig. B.2 are intensity plots for both the longitude angle ( $2\psi$ ) and elevation angle ( $2\chi$ ) for all LCVR voltage space.

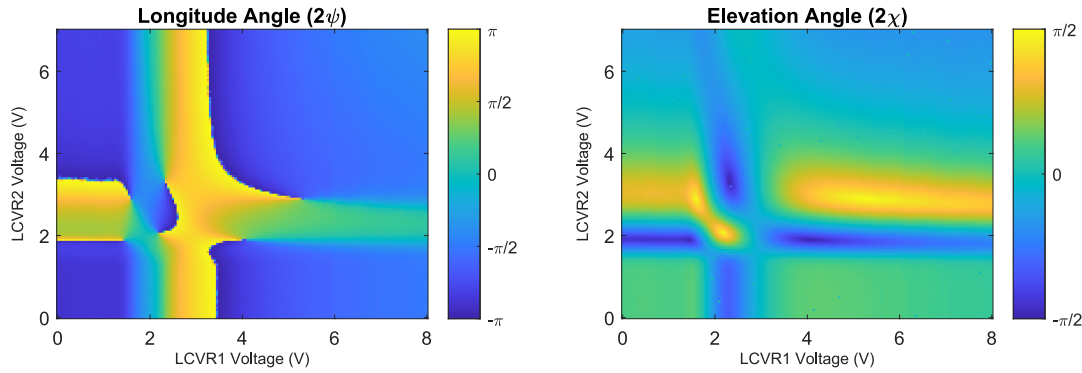


FIGURE B.2: Intensity plots for the longitude ( $2\psi$ ) and elevation ( $2\chi$ ) angles.

To find the voltage values corresponding to each polarization, we plot five maps contour (Fig. B.3): one for each linear polarization and one for both circular polarizations. The linear polarizations have contours corresponding to the longitude angle ( $2\psi$ ) in Table B.1<sup>1</sup> and 0 elevation angle ( $2\chi$ ). While the circular case requires only the elevation contours. To choose the voltages values for each polarization the measured angles need to match those found in Table B.1. For example, X polarization requires both angles be = 0, and we can see that there is only one region where the blue dotted  $2\chi = 0$  contour crosses through a shaded red region of  $2\psi = 0$ . The chosen voltage values are marked on each plot as dots (crosses) for the linear (circular) cases. These values are chosen after a small bit of manual optimization.

<sup>1</sup>For these cases we actually plot regions around the specified values as the phase flip at  $\pm\pi$  leads to erroneous contours.



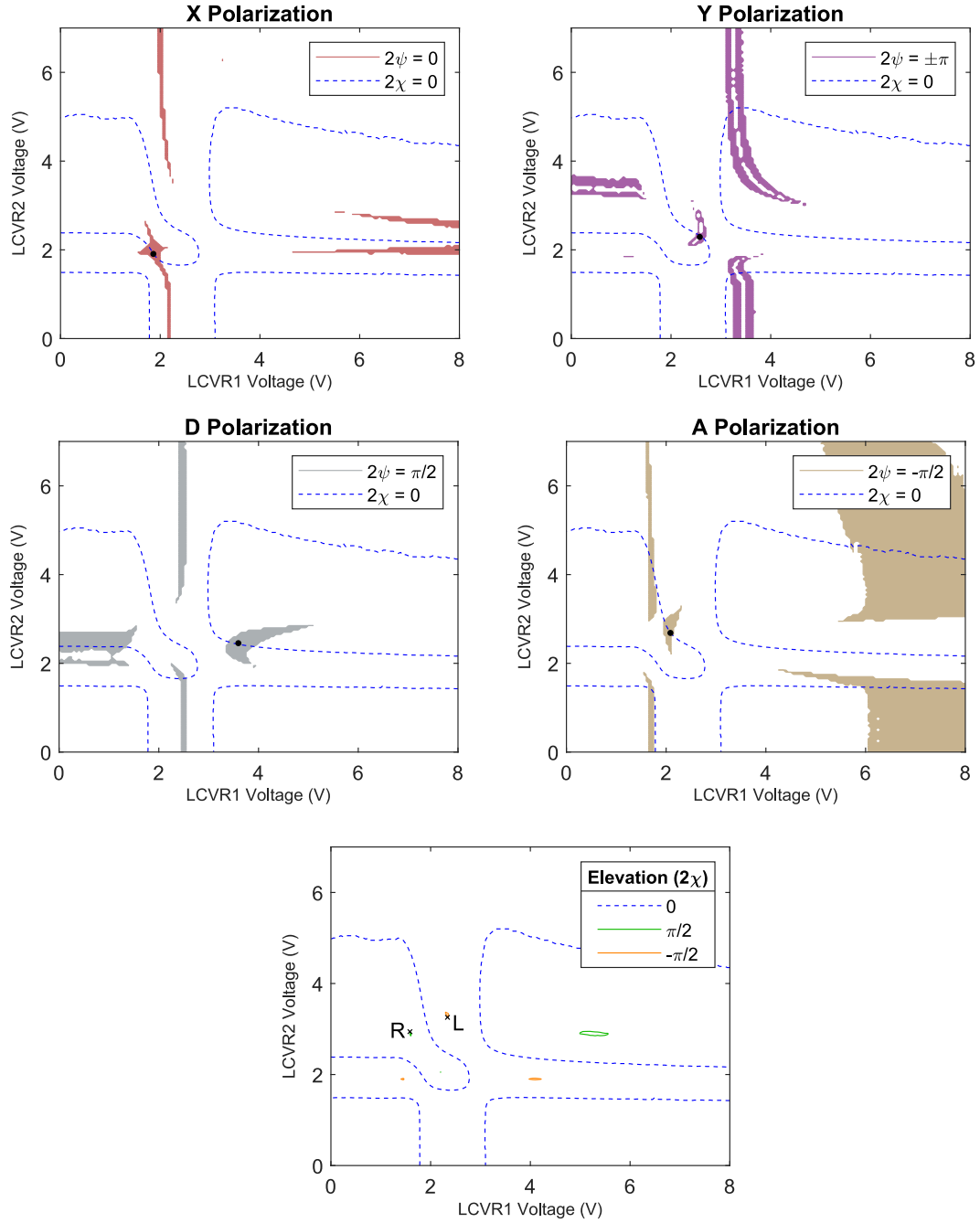


FIGURE B.3: LCVR contour calibration maps.

## Appendix C

# Calibrating the Azimuth of an Optic to a Rotation Mount

### Polarizer Calibration

Set up the optics in the following order:

- 1) Laser
- 2) Polarizer  $P_1$  (does not need to be calibrated; oriented at approximated 45 degrees)
- 3) Polarizer  $P_2$  to calibrate, held in a rotation mount (e.g., Thorlabs RSPD1)
- 4) Power meter or photodiode to measure the signal

To calibrate the polarizer  $P_2$ :

- 1) Record the intensity using the power meter or photodiode ( $I_1$ ).
- 2) Rotate the polarizer  $P_2$  180° about the *vertical* axis (i.e., rotate it on its optical post).
- 3) Record the intensity again ( $I_2$ ).
- 4) Rotate the polarizer  $P_2$  in its mount (i.e., rotate it about the horizontal axis) so the intensity is halfway between  $I_1$  and  $I_2$ .
- 5) Repeat steps 1-4 until  $I_1$  and  $I_2$  are equal.

Notes: The method will work for any choice of angle for the polarizer  $P_1$  excepting 0° or 90° (X or Y), however it is most easily done with the angle at  $\pm 45^\circ$  (D or A).

**Quarter-wave plate (QWP) Calibration**

This method works best with two already calibrated polarizers. The above method can be used to calibrate these polarizers.

Set up the optics in the following order:

- 1) Laser
- 2) Calibrated polarizer  $P_1$  in a rotation mount
- 3) QWP to calibrate, held in a rotation mount
- 4) Calibrated polarizer  $P_2$  in a rotation mount
- 5) Power meter or photodiode to measure the signal

To Calibrate the QWP:

- 1) Set the angles of both  $P_1$  and  $P_2$  to be  $45^\circ$  (D).
- 2) Minimize the measured intensity by rotating the QWP azimuth.
- 3) Set the angle of  $P_2$  to be  $0^\circ$  (X).
- 4) Record the intensity ( $I_1$ ).
- 5) Rotate the QWP  $180^\circ$  about the *vertical* axis (rotate its optical post in the post holder).
- 6) Record the intensity again ( $I_2$ ).
- 7) Rotate the QWP in its mount (i.e., rotate it about the horizontal axis) so the intensity is halfway between  $I_1$  and  $I_2$ .
- 8) Repeat steps 4-7 until  $I_1$  and  $I_2$  are equal.

Notes: Depending on the initial orientation of the QWP, steps alone 4-7 may align the fast or slow axis to be  $45^\circ$ ; steps 1-2 ensure that this does not occur.

## Appendix D

# Polarimeter Device Construction

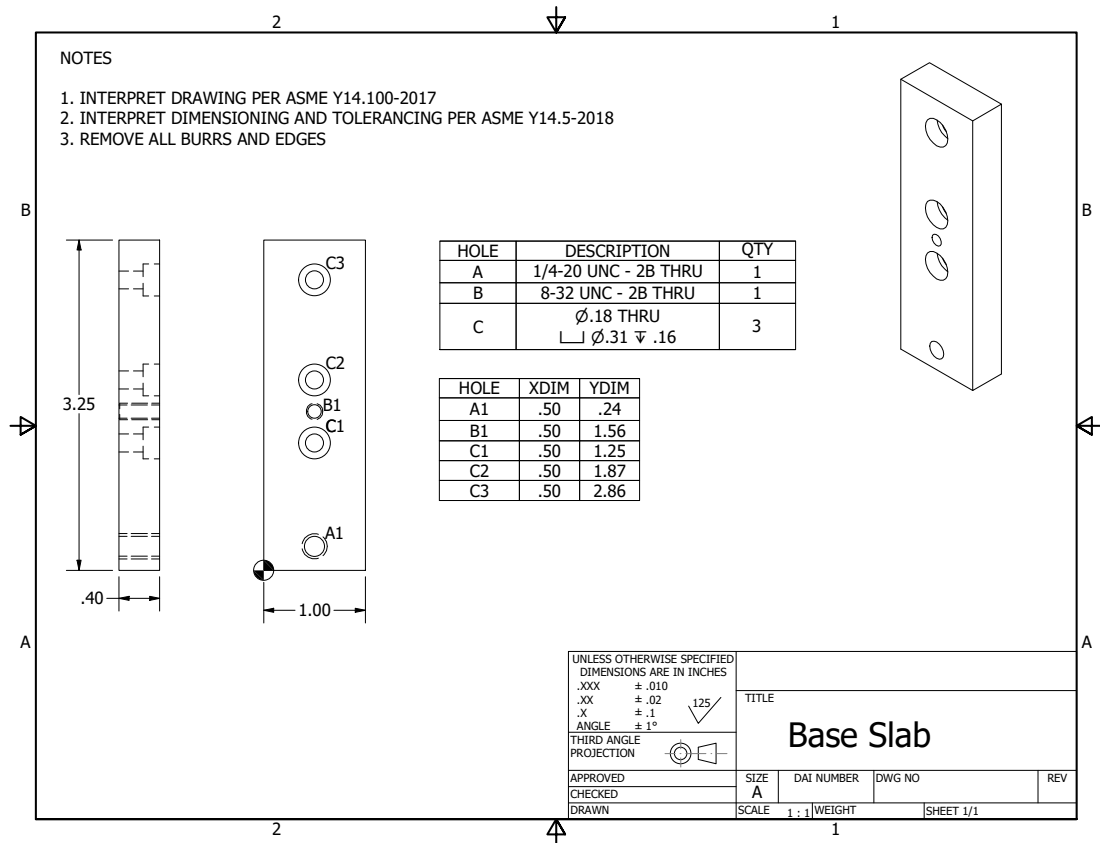
This appendix provides details on the construction of the polarimeter device described in Chapter 4. Section D.1 outlines the construction of the physical measurement part of the device (Fig. 4.1), Sec. D.2 describes the procedure to calibrate the angle  $\phi = 0$ , and Sec. D.3 shows the electrical circuit and printed circuit board design.

### D.1 Drawings of Mechanical System

Included here are drawings for each of the mechanical parts necessary to construct the measurement part of the polarimeter device, as seen in Fig. 4.1. The final drawing is an exploded view of the entire device, which shows explicitly how to assemble the device.

## Base Slab

All components of the measurement device are mounted on this piece. The three counterbored 8-32 holes (C1-C3) are for the motor holder, the analyzer, and the photodiode. A standard optical post mounts to the central threaded 8-32 hole (B1). The threaded 1/4-20 hole (A1) on the end mounts the photo-interrupter holder.



Motor Holder

This piece mounts to the base slab directly in front of the analyzer. The hollow axle motor (Tiger GB2208-80) is secured via the 4 counterbored holes for M3 screws (B1-B4).

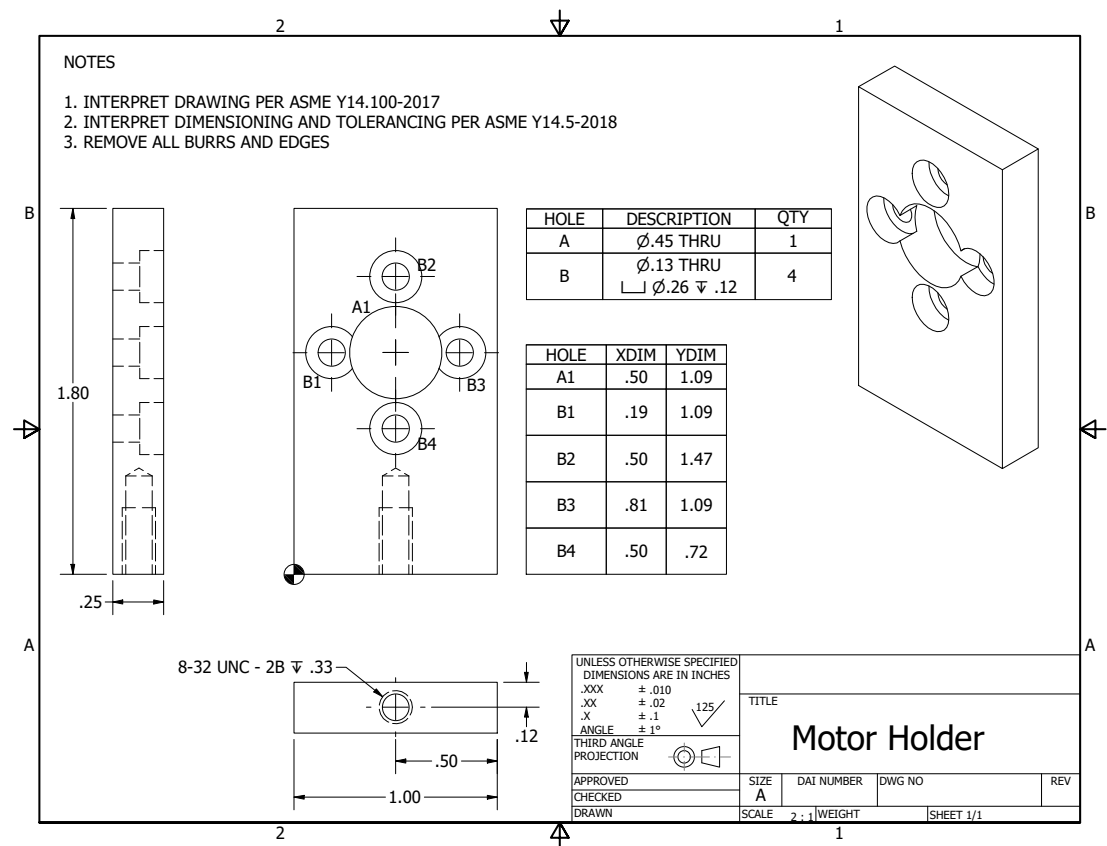
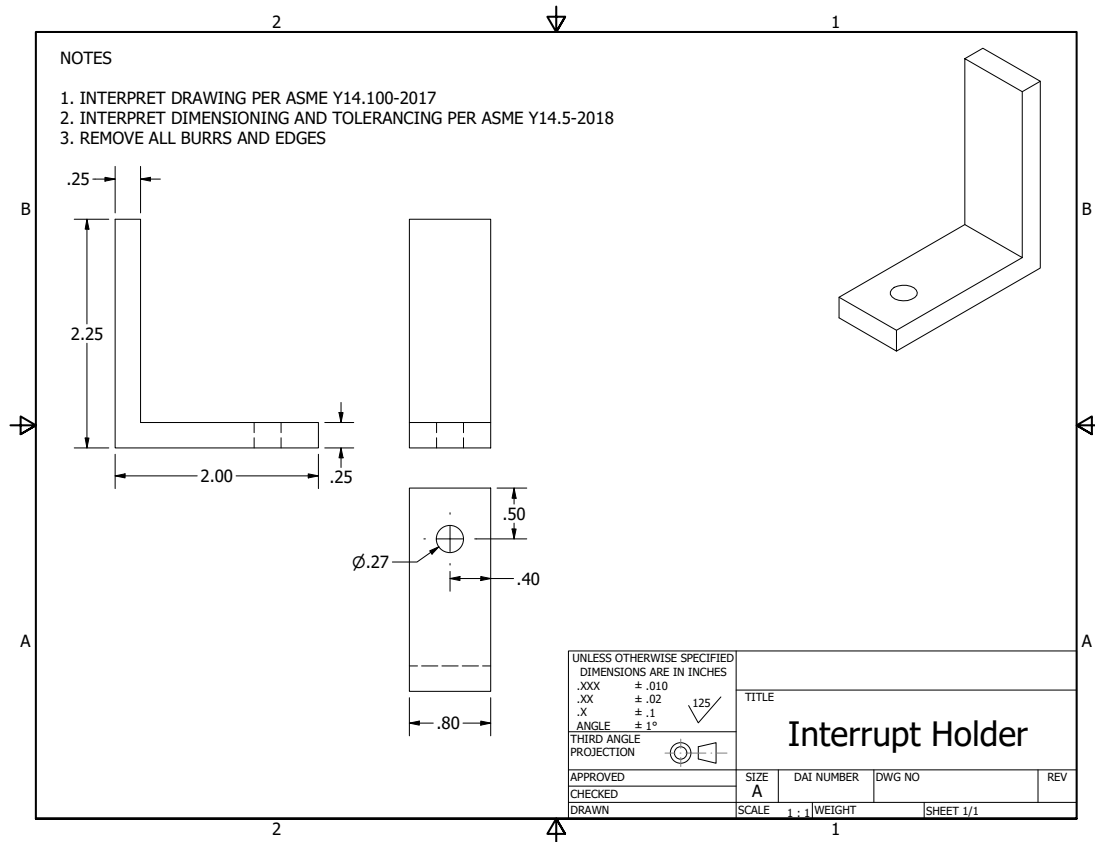


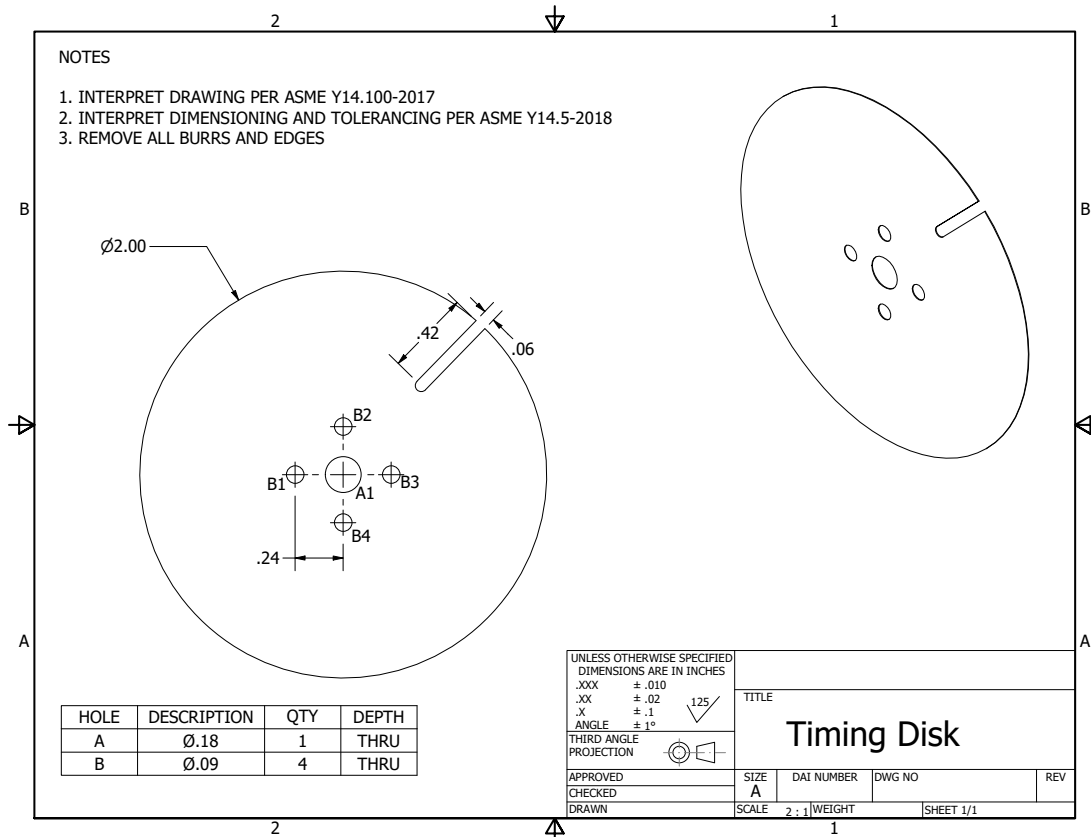
## Photo-Interrupter Mount

This piece mounts to the base slab via the threaded  $\frac{1}{4}$ -20 hole near the end (A1). The photo-interrupter is attached to a small piece of PCB that is secured to the vertical arm of the mount using rubber bands, which allows a firm hold while also allowing small movements for calibration.



## Timing Disk

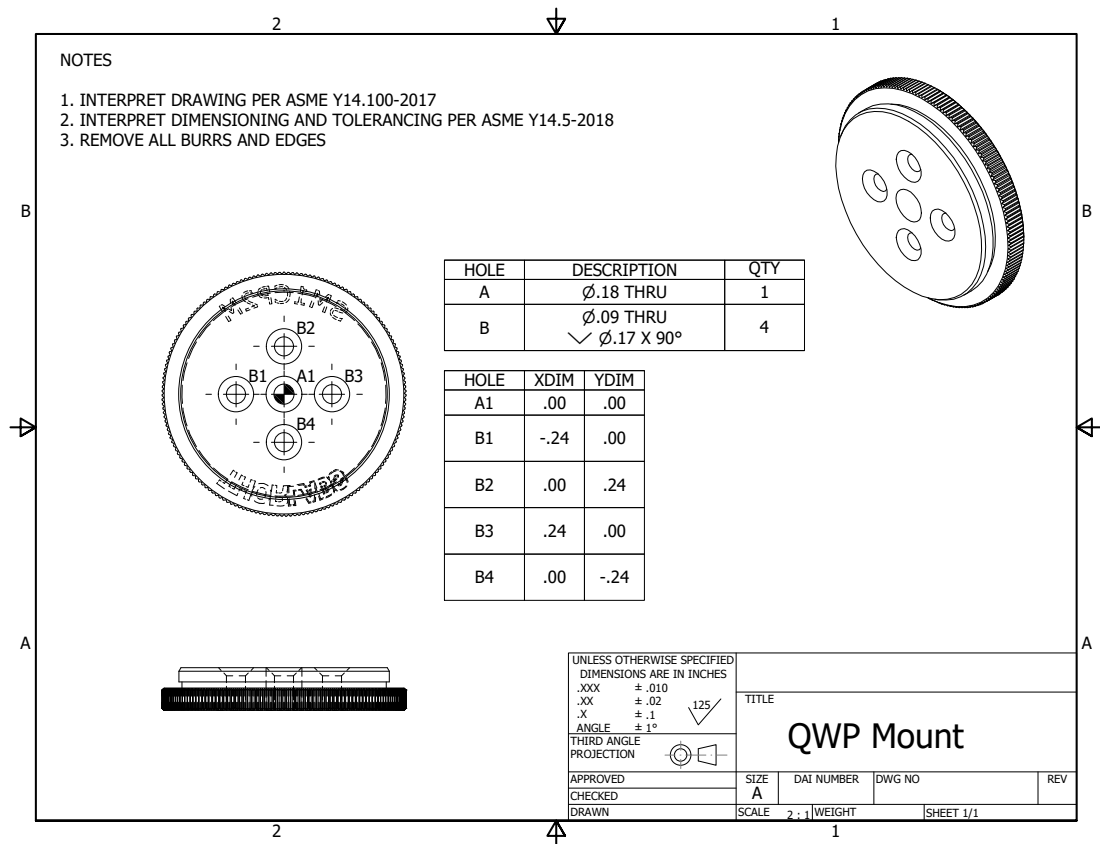
The timing disk is secured between the custom QWP mount and the motor.



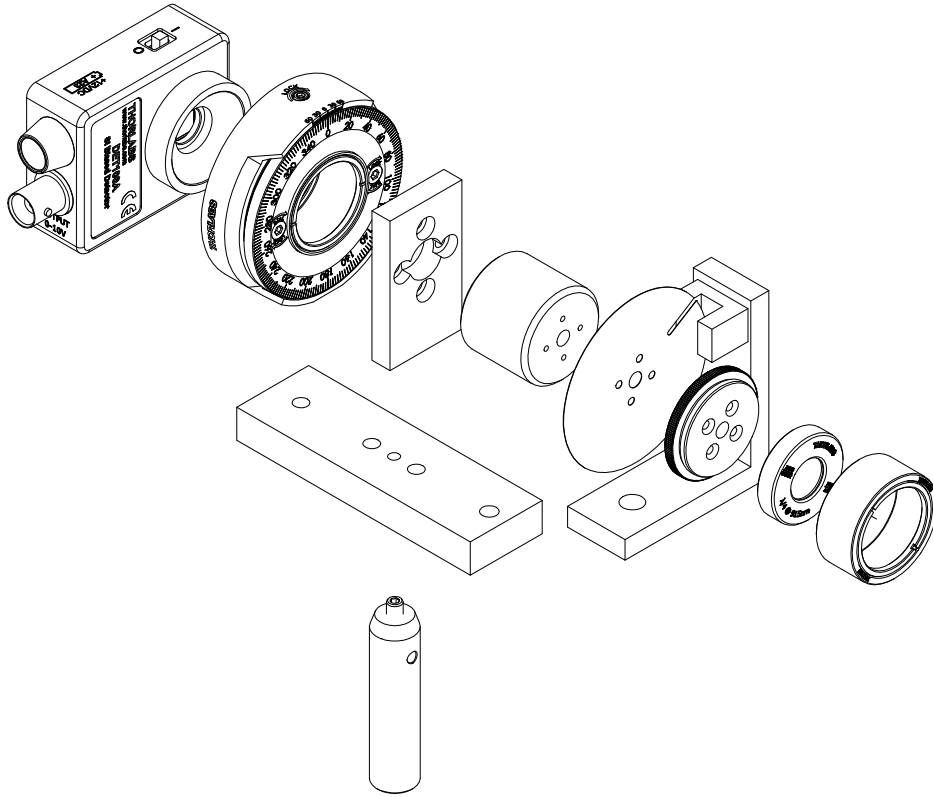


## Custom Quarter-wave Plate Mount

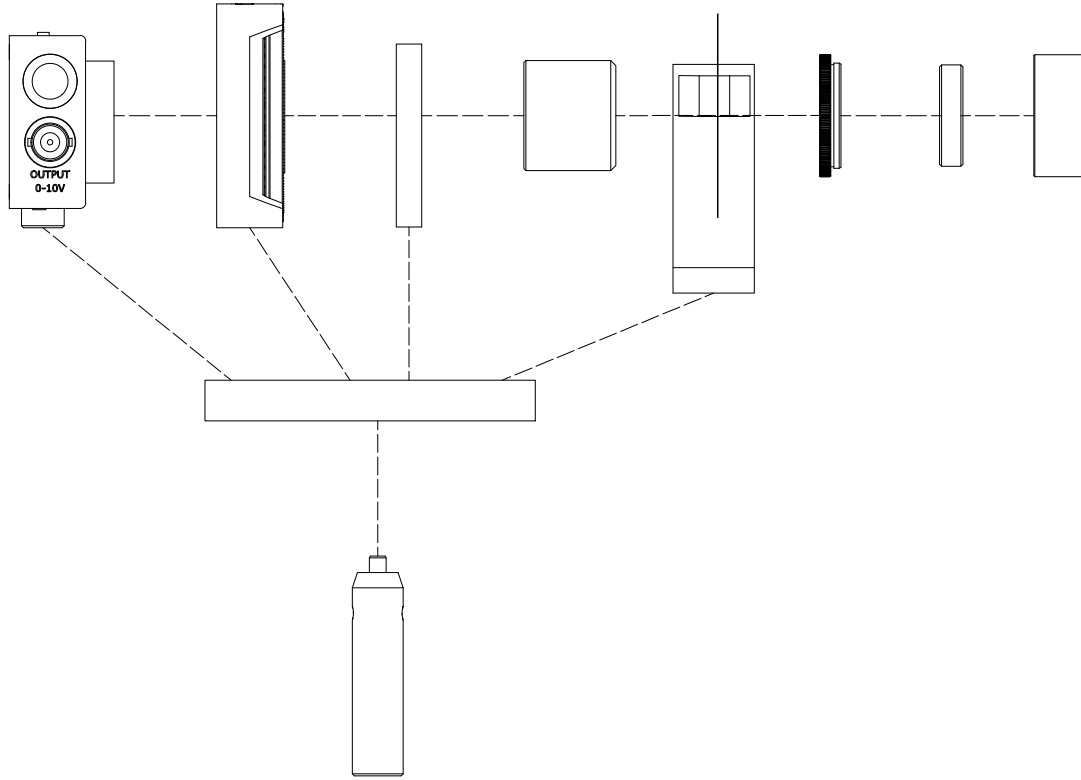
These modifications are made to the Thorlabs part SM1CP2M to match the hollow axle motor (Tiger GB2208-80) used in this work. The assembled mount is shown in the exploded views on the following page. It uses an SM1 lens tube and retaining ring from Thorlabs.



## Exploded Orthographic View of Device



## Side View

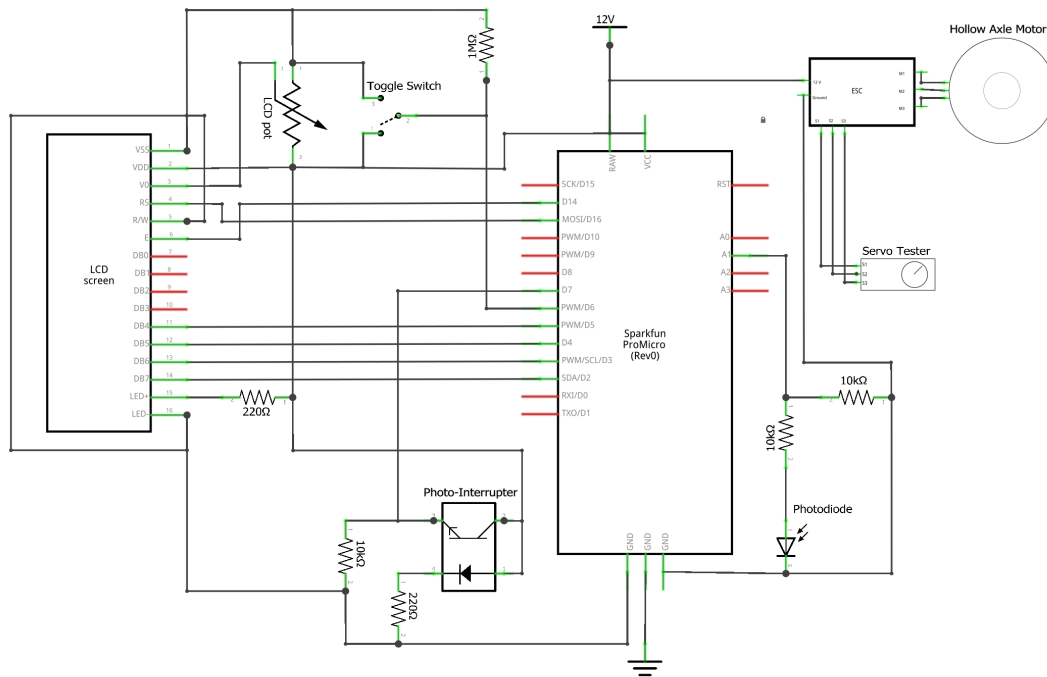


## D.2 Calibrating the Polarimeter

This calibration procedure is done entirely with X-polarized light from a calibrated polarizer upstream of the polarimeter.

- 1) Align the fast axis (FA) of the quarter-wave plate (QWP) to be roughly horizontally oriented (X) when the trigger will fire.
- 2) Set the toggle switch so that the Poincaré sphere angles are visible on the LCD screen. Physically move the position of the photo-interrupter up and down on its mount until the longitude angle is  $(0 \pm 1)^\circ$ .

## D.3 Circuit Diagram and Printed Circuit Board (PCB)

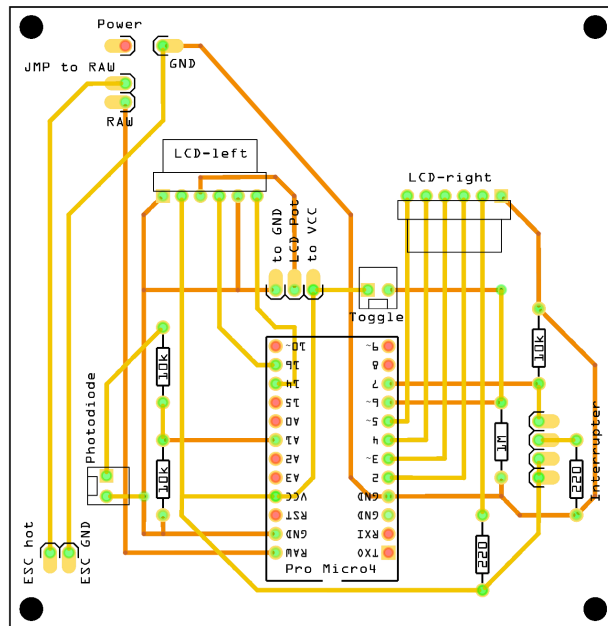


## D.4 Arduino Code

```

1 // Polarimeter_final.ino
2 // This code processes the voltage signals from the photodiode and
3 // the photo-interrupter with a fast Fourier transform (FFT), calculates
4 // the Stokes vectors, and outputs the results to the LCD screen.
5 //
6 // INPUTS
7 // photodiode signal:      adcPin = A1
8 // photo-interrupter signal: interruptPin = 7
9 // toggle switch:          switchPin = 6
10 //
11 // The toggle switch controls whether the Stokes vector parameters
12 // or angles are shown on the LCD.
13 //
14 // OUTPUTS
15 // S0 Stokes:              avg_Stokes[0]
16 // S1 Stokes:              avg_Stokes[1]
17 // S2 Stokes:              avg_Stokes[2]
18 // S3 Stokes:              avg_Stokes[3]
19 // longitude angle (2*psi): avg_longitude
20 // elevation angle (2*chi): avg_elevation
21 //
22 // The outputs are displayed on the LCD screen and sent via Serial output
23 // to a connected computer.
24
25 /*
26 * Library sources
27 * AnalogReadFast.h  http://www.avdweb.nl/arduino/libraries/fast-10-bit-adc.html

```



```

28 * TimerOne.h           https://www.pjrc.com/teensy/td\_libs\_TimerOne.html
29 * arduinoFFT.h         https://github.com/kosme/arduinoFFT (loaded via Library
    manager)
30 */
31
32 #include <avdweb_AnalogReadFast.h> // Allows using a faster analog read function
33 #include <TimerOne.h> // Allows using the built-in timers to throw interrupts
34 #include <LiquidCrystal.h> // Allows displaying to an LCD screen
35 #include "arduinoFFT.h" // Allows Fast Fourier Transform
36
37 // These factors are used to average the rotation period,
38 // where N is the number of cycles to average over. (Here N=10)
39 #define OLDFACTOR 0.9 // = (N - 1) / N
40 #define NEWFACTOR 0.1 // = 1/N
41
42 // For use in changing radians to degrees
43 #define DEGREES 57.2957795 // = 180 / pi
44
45 // Number of points to sample in one trigger cycle
46 // Should be a power of 2 that is >= 32
47 #define NPTS 64
48
49 // For output of the Fourier transform.
50 #define M_PI 3.141592653589793238462643
51
52 // For the number of measurement cycles to average (N=10)
53 #define arraySetNumber 10
54
55
56 //***** DECLARE VARIABLES *****
57
58 int interruptPin = 7; // Attach the trigger output to this pin.
59
60 volatile unsigned long prev_trigger = 0; // previous trigger, in microseconds
61 volatile unsigned long curr_trigger = 0; // current trigger, in microseconds
62 volatile unsigned long rotation_period = 0; // rotation period, in microseconds
63
64 // Flags to control program flow
65 volatile boolean startMeasuring = false; // Whether to start measuring the
    photodiode signal
66 volatile boolean processing = true; // Whether the loop is processing the
    photodiode signal data
67                                     // Starts true so no measurement until setup()
    is done
68 volatile boolean updateLCD = false; // Whether to update the LCD display
69
70 // For storing and FFT'ing data
71 volatile double vReal[NPTS]; // Array for actual photodiode data and real part of
    FFT
72 volatile double vImag[NPTS]; // Array for imag part of FFT
73 volatile int j = 0; // Keep track of which bin stores the photodiode voltage
74 const int adcPin = A1; // Analog input pin for photodiode signal
75
76 // For calculating the Stokes vector

```

```

77 double A = 0; // DC peak
78 double B = 0; // Imaginary part of 2*f peak
79 double C = 0; // Real part of 4*f peak
80 double D = 0; // Imaginary part of 4*f peak
81 float beta = 0.0524; // Compensate for imperfect QWP retardance
82 float delta = (M_PI/2) + beta; // Actual measured retardance
83 double stokes[] = {0, 0, 0, 0}; // Stokes vector
84
85 // Parameters calculated from the Stokes vector
86 double DOP = 0; // Degree of polarization
87 double longitude = 0; // Longitude of Stokes vector, 2*psi
88 double elevation = 0; // Elevation of Stokes vector from equator, 2*chi
89 double orientation = 0; // Angle of polarization ellipse major axis relative to X-
    axis
90 double ellipticityAngle = 0; // atan( minor axis / major axis )
91
92 // AVERAGING LAST 10 MEASUREMENTS
93 // Arrays for storing last 10 measurements
94 double set_stokes_0[] = {0, 0, 0, 0, 0, 0, 0, 0, 0, 0, 0};
95 double set_stokes_1[] = {0, 0, 0, 0, 0, 0, 0, 0, 0, 0, 0};
96 double set_stokes_2[] = {0, 0, 0, 0, 0, 0, 0, 0, 0, 0, 0};
97 double set_stokes_3[] = {0, 0, 0, 0, 0, 0, 0, 0, 0, 0, 0};
98 double set_DOP[] = {0, 0, 0, 0, 0, 0, 0, 0, 0, 0, 0};
99 double set_longitude[] = {0, 0, 0, 0, 0, 0, 0, 0, 0, 0, 0};
100 double set_elevation[] = {0, 0, 0, 0, 0, 0, 0, 0, 0, 0, 0};
101 double set_orientation[] = {0, 0, 0, 0, 0, 0, 0, 0, 0, 0, 0};
102 double set_ellipticityAngle[] = {0, 0, 0, 0, 0, 0, 0, 0, 0, 0, 0};
103
104 // Index for counting assignment to arrays
105 int indexArr = 0;
106
107 // Sums for averages
108 double sum_stokes[] = {0, 0, 0, 0};
109 double sum_DOP = 0;
110 double sum_longitude = 0;
111 double sum_elevation = 0;
112 double sum_orientation = 0;
113 double sum_ellipticityAngle = 0;
114
115 // Average values
116 double avg_stokes[] = {0, 0, 0, 0};
117 double avg_DOP = 0;
118 double avg_longitude = 0;
119 double avg_elevation = 0;
120 double avg_orientation = 0;
121 double avg_ellipticityAngle = 0;
122
123 // Strings with which to display the results
124 String S0_str = String(stokes[0], 0); // Light intensity, 2 decimals
125 String S1_str = String(stokes[1], 2); // Rectilinear Stokes parameter
126 String S2_str = String(stokes[2], 2); // Diagonal Stokes parameter
127 String S3_str = String(stokes[3], 2); // Circular Stokes parameter
128 String orient_str = String(orientation * DEGREES, 0); // Angle of ellipse
129 String long_str = String(longitude * DEGREES, 0); // Longitude of Stokes vector

```

```

130 String elev_str = String(elevation * DEGREES, 0); // Elevation of Stokes vector
131 String message1_str = "Measuring period"; // Display on first line of LCD
132 String message2_str = "please wait"; // Display on second line of LCD
133
134 // For controlling which screen is shown with the toggle button
135 int switchPin = 6; // Toggle switch input
136 int switchVal = 0; // Value of toggle switch (HIGH or LOW)
137 int screen = 0; // Controls which screen is shown
138
139 // For controlling when the LCD updates
140 double Tstamp = 0; // Current program time, in ms
141 double updateFreq = 250; // How often to update the LCD, in ms
142 int updateNum = 1; // Keep track of updates
143 double T0 = 0; // Start of program time, in ms
144
145
146 // ***** CREATE OBJECTS *****
147
148 // Create FFT object
149 arduinoFFT FFT = arduinoFFT();
150
151 // Create LCD object
152 const int rs = 16, en = 14, d4 = 5, d5 = 4, d6 = 3, d7 = 2;
153 LiquidCrystal lcd(rs, en, d4, d5, d6, d7);
154
155
156 // ***** S E T U P *****
157
158 void setup() {
159     // set up the LCD's number of columns and rows:
160     lcd.begin(16, 2);
161     // Print a message to the LCD; will be "Measuring period" at first
162     lcd.print( message1_str );
163     lcd.setCursor(0, 1); // Move to beginning of second line
164     lcd.print( message2_str );
165
166     Serial.begin(9600);
167
168     // Wipe the data in prep for the first measurement and FFT
169     for (int k=0; k < NPTS; k++) {
170         vReal[k] = 0;
171         vImag[k] = 0;
172     }
173
174     // Set up the input pin for the photodiode signal
175     pinMode( adcPin, INPUT );
176
177     // Set up the input pin for the toggle switch to change LCD display
178     pinMode( switchPin, INPUT );
179
180     // Set up the interrupt pin as an input
181     pinMode( interruptPin, INPUT );
182     // Attach the external interrupt to the trigger_ISR
183     attachInterrupt( digitalPinToInterrupt ( interruptPin ), trigger_ISR, RISING );

```



```

184
185 // Wait a second so the trigger period is well characterized by trigger_ISR.
186 delay( 1000 ); // Delay in ms
187
188 // Initialize a timer to interrupt NPTS times each rotation period
189 noInterrupts(); // Turn off interrupts
190 Timer1.initialize( rotation_period / NPTS );
191 interrupts(); // Turn interrupts back on again
192
193 // Attach the timer interrupt to the sampling_ISR
194 Timer1.attachInterrupt( sampling_ISR );
195
196 // Set the processing flag so the next trigger will begin measurement
197 processing = false;
198
199 }
200
201
202 // ***** L O O P *****
203
204 void loop() {
205 // The loop only processes the data if the 'processing' flag is set to TRUE
206 if ( processing ) {
207
208 // Output detected intensity signal to the Serial Plotter
209 //for (int k=0; k < NPTS; k++) {
210 //Serial.println(vReal[k]);
211 //}
212
213 // P R O C E S S I N G
214 // Process 'vReal' and 'vImag' to obtain the Stokes parameters
215 FFT.Compute(vReal, vImag, NPTS, FFT_FORWARD); // Compute FFT in-place
216
217 A = 2 * vReal[0] / NPTS; // DC peak
218 B = 4 * vImag[2] / NPTS; // Imaginary part of 2*f peak
219 C = 4 * vReal[4] / NPTS; // Real part of 4*f peak
220 D = 4 * vImag[4] / NPTS; // Imaginary part of 4*f peak
221 // S0: total light intensity
222 stokes[0] = (A - (C / ( tan(delta/2)*tan(delta/2) ) ) ) / (sqrt(2*M_PI) );
223 // S1: rectilinear Stokes parameter
224 stokes[1] = C / ( stokes[0] * sin(delta/2)*sin(delta/2) * sqrt(2*M_PI) );
225 // S2: diagonal Stokes parameter
226 stokes[2] = D / ( stokes[0] * sin(delta/2)*sin(delta/2) * sqrt(2*M_PI) );
227 // S3: circular Stokes parameter
228 stokes[3] = B / ( stokes[0] * sin(delta) * sqrt(2 * M_PI) );
229 DOP = sqrt(stokes[1]*stokes[1]+stokes[2]*stokes[2]+stokes[3]*stokes[3])/stokes
    [0];
230 // Poincare sphere angles
231 longitude = atan2( stokes[2], stokes[1] );
232 elevation = atan2( stokes[3], sqrt( stokes[1]*stokes[1] + stokes[2]*stokes[2]
    ) );
233 // Polarization ellipse angles
234 orientation = 0.5 * longitude; // Angle relative to X-axis
235 ellipticityAngle = 0.5 * elevation; // atan( minor axis / major axis )

```

```

236
237 // A V E R A G I N G
238 set_stokes_0[indexArr] = stokes[0];
239 set_stokes_1[indexArr] = stokes[1];
240 set_stokes_2[indexArr] = stokes[2];
241 set_stokes_3[indexArr] = stokes[3];
242 set_DOP[indexArr] = DOP;
243 set_longitude[indexArr] = longitude;
244 set_elevation[indexArr] = elevation;
245 set_orientation[indexArr] = orientation;
246 set_ellipticityAngle[indexArr] = ellipticityAngle;
247
248 // Index control and set back to zero after the 10th measurement
249 indexArr++; // increment index
250 if( indexArr == 10){
251     indexArr = 0;
252 }
253
254 // Zero the sum arrays
255 sum_stokes[0] = 0;
256 sum_stokes[1] = 0;
257 sum_stokes[2] = 0;
258 sum_stokes[3] = 0;
259 sum_DOP = 0;
260 sum_longitude = 0;
261 sum_elevation = 0;
262 sum_orientation = 0;
263 sum_ellipticityAngle = 0;
264
265 // Calculate the averages
266 for (int k = 0; k <= (arraySetNumber-1); k++){
267     sum_stokes[0] += set_stokes_0[k];
268     sum_stokes[1] += set_stokes_1[k];
269     sum_stokes[2] += set_stokes_2[k];
270     sum_stokes[3] += set_stokes_3[k];
271     sum_DOP += set_DOP[k];
272     sum_longitude += set_longitude[k];
273     sum_elevation += set_elevation[k];
274     sum_orientation += set_orientation[k];
275     sum_ellipticityAngle += set_ellipticityAngle[k];
276 }
277
278 avg_stokes[0] = sum_stokes[0] / arraySetNumber;
279 avg_stokes[1] = sum_stokes[1] / arraySetNumber;
280 avg_stokes[2] = sum_stokes[2] / arraySetNumber;
281 avg_stokes[3] = sum_stokes[3] / arraySetNumber;
282 avg_DOP = sum_DOP / arraySetNumber;
283 avg_longitude = sum_longitude / arraySetNumber;
284 avg_elevation = sum_elevation / arraySetNumber;
285 avg_orientation = sum_orientation / arraySetNumber;
286 avg_ellipticityAngle = sum_ellipticityAngle / arraySetNumber;
287
288 // Output Stokes parameters to Serial output for interfacing with a computer
289 Serial.print(avg_stokes[0]);

```

```

290     Serial.print(" ");
291     Serial.print(avg_stokes[1]);
292     Serial.print(" ");
293     Serial.print(avg_stokes[2]);
294     Serial.print(" ");
295     Serial.print(avg_stokes[3]);
296     Serial.print(" ");
297     Serial.print(avg_longitude);
298     Serial.print(" ");
299     Serial.print(avg_elevation);
300     Serial.print(" ");
301
302     // Determine whether to update the LCD screen
303     if ( Tstamp == 0 ) {
304         T0 = millis();
305     }
306     Tstamp = millis();
307     if ( (Tstamp-T0) > updateNum*updateFreq ) {
308         updateLCD = true;
309     }
310     else {
311         updateLCD = false;
312     }
313
314     // The loop only updates the LCD screen if the 'updateLCD' flag is set to TRUE
315     if ( updateLCD ) {
316         // D I S P L A Y
317         // Display the results of the data analysis
318         // Prepare the String objects to be displayed
319         // Stokes parameters
320         S0_str = String(avg_stokes[0], 0); // Light intensity, 2 decimals
321         S1_str = String(avg_stokes[1], 2); // Rectilinear Stokes parameter
322         S2_str = String(avg_stokes[2], 2); // Diagonal Stokes parameter
323         S3_str = String(avg_stokes[3], 2); // Circular Stokes parameter
324         // Poincare sphere angles
325         orient_str = String(avg_orientation * DEGREES, 0); // Angle of ellipse
326         long_str = String(avg_longitude * DEGREES, 1); // Longitude angle
327         elev_str = String(avg_elevation * DEGREES, 1); // Elevation angle
328         // Concatenate the Strings into the message to display
329         message1_str = S1_str + " " + S2_str + " " + S3_str;
330         message2_str = orient_str + " " + long_str + " " + elev_str;
331
332         lcd.clear(); // Clear the LCD screen so no remnants from last message
333         lcd.home(); // Set the cursor to beginning of first line
334
335         // Detect the toggle switch to switch between LCD display types
336         switchVal = digitalRead(switchPin);
337         if ( switchVal == HIGH ) {
338             screen = 2;
339         }
340         else {
341             screen = 1;
342         }
343

```

```

344     switch(screen){
345         case 1:
346             // Display the Stokes parameters
347             lcd.print(S0_str);
348             lcd.setCursor(6,0);
349             lcd.print("Stokes:");
350             lcd.setCursor(0,1); // Move cursor to beginning of second line
351             lcd.print( message1_str );
352             break;
353
354         case 2:
355             // Display the intensity, ellipse orientation, longitude, and elevation
356             lcd.print(S0_str);
357             lcd.setCursor(6,0);
358             lcd.print("Angles:");
359             lcd.setCursor(1,1); // Move cursor to beginning of second line
360             lcd.print( message2_str );
361             break;
362
363         default:
364             // Calibration screen shown at the beginning
365             lcd.print("  Phase: ");
366             lcd.setCursor(10,0);
367             lcd.print(long_str);
368             lcd.setCursor(0,1);
369             lcd.print("Flip the switch to cont");
370             break;
371     }
372     updateNum++; // Increment updateNum for next loop cycle
373     updateLCD = false; // Don't update LCD until it is time again
374 }
375
376 // C L E A N   U P
377 // Wipe the imaginary part of the FFT in prep for the next loop
378 for (int k=0; k < NPTS; k++) {
379     vImag[k] = 0;
380 }
381 // Notify the ISRs that we're done processing the data
382 processing = false;
383
384 }
385
386 // Update the timer interrupt period based on the current trigger period
387 noInterrupts(); // Turn off interrupts
388 Timer1.setPeriod( rotation_period / NPTS );
389 interrupts(); // Turn interrupts back on again.
390 }
391
392
393 // ***** INTERRUPT SERVICE ROUTINES *****
394
395 void trigger_ISR() {
396     curr_trigger = micros();
397     // Microseconds since the Arduino board began running the current program.

```

```

398
399     rotation_period = OLDFACTOR * rotation_period + NEWFACTOR * (curr_trigger -
        prev_trigger);
400     // Average rotation period over the last N triggers (N=10)
401     // It takes N triggers to reach a stable value after start-up
402
403     // Save current trigger time for the next call of trigger_ISR
404     prev_trigger = curr_trigger;
405
406     if ((!processing) && (!startMeasuring)) { // If the loop is done processing
407         startMeasuring = true; // ...then start measuring the next cycle.
408
409         // Measure the first sample of photodiode voltage and store it
410         // j should have been set to 0 in sampling_ISR after the last measurement
411         vReal[j] = analogReadFast( adcPin ); // 10-bit resolution (0-1023)
412         j++; // increment the bin number for the next sample
413         Timer1.restart(); // Restart the timer at the beginning of a new period
414                         // This keeps the timer in phase with the trigger
415     }
416 }
417
418 void sampling_ISR() { // Runs NPTS - 1 times per of rotation
419     // Measure only when the trigger says go
420     if ( startMeasuring ) {
421         if ( j == NPTS - 1 ) { // If this is the last measurement in this cycle...
422             Timer1.stop(); // Stop the timer, which prevents the ISR from running again
423             startMeasuring = false; // Set the flag to prevent further measurement
424             processing = true; // Start processing of data in the loop()
425         }
426
427         // Measure the photodiode voltage and store it
428         vReal[j] = double( analogReadFast( adcPin ) ); // 10-bit resolution (0-1023)
429         // Increment the bin number modulo the number of bins
430         // This makes j=0 after the last measurement
431         j = (j + 1) % NPTS;
432     }
433 }
434
435 // end Polarimeter_final.ino

```

# Bibliography

- [1] Ehud Altman et al. “Quantum Simulators: Architectures and Opportunities”. en. In: *PRX Quantum* 2.1 (Feb. 2021), p. 017003. ISSN: 2691-3399. DOI: [10.1103/PRXQuantum.2.017003](https://doi.org/10.1103/PRXQuantum.2.017003).
- [2] Peter Lodahl. “Quantum-dot based photonic quantum networks”. en. In: *Quantum Science and Technology* 3.1 (Jan. 2018), p. 013001. ISSN: 2058-9565. DOI: [10.1088/2058-9565/aa91bb](https://doi.org/10.1088/2058-9565/aa91bb).
- [3] Lilian Childress and Ronald Hanson. “Diamond NV centers for quantum computing and quantum networks”. en. In: *MRS Bulletin* 38.2 (Feb. 2013), pp. 134–138. ISSN: 0883-7694, 1938-1425. DOI: [10.1557/mrs.2013.20](https://doi.org/10.1557/mrs.2013.20).
- [4] Chunhua Dong, Yingdan Wang, and Hailin Wang. “Optomechanical interfaces for hybrid quantum networks”. en. In: *National Science Review* 2.4 (Dec. 2015), pp. 510–519. ISSN: 2053-714X, 2095-5138. DOI: [10.1093/nsr/nwv048](https://doi.org/10.1093/nsr/nwv048).
- [5] H. J. Kimble. “The quantum internet”. en. In: *Nature* 453.7198 (June 2008), pp. 1023–1030. ISSN: 0028-0836, 1476-4687. DOI: [10.1038/nature07127](https://doi.org/10.1038/nature07127).
- [6] D. Gammon et al. “Fine Structure Splitting in the Optical Spectra of Single GaAs Quantum Dots”. In: *Physical Review Letters* 76.16 (Apr. 1996), pp. 3005–3008. DOI: [10.1103/PhysRevLett.76.3005](https://doi.org/10.1103/PhysRevLett.76.3005).
- [7] K. Brunner et al. “Sharp-line photoluminescence of excitons localized at GaAs/AlGaAs quantum well inhomogeneities”. en. In: *Applied Physics Letters* 64.24 (June 1994), pp. 3320–3322. ISSN: 0003-6951, 1077-3118. DOI: [10.1063/1.111265](https://doi.org/10.1063/1.111265).
- [8] Hyochul Kim et al. “A quantum logic gate between a solid-state quantum bit and a photon”. en. In: *Nature Photonics* 7.5 (May 2013), pp. 373–377. ISSN: 1749-4885. DOI: [10.1038/nphoton.2013.48](https://doi.org/10.1038/nphoton.2013.48).

- [9] R. Hanson et al. "Spins in few-electron quantum dots". en. In: *Reviews of Modern Physics* 79.4 (Oct. 2007), pp. 1217–1265. ISSN: 0034-6861, 1539-0756. DOI: [10.1103/RevModPhys.79.1217](https://doi.org/10.1103/RevModPhys.79.1217).
- [10] G. S. Solomon et al. "Vertically Aligned and Electronically Coupled Growth Induced InAs Islands in GaAs". en. In: *Physical Review Letters* 76.6 (Feb. 1996), pp. 952–955. ISSN: 0031-9007, 1079-7114. DOI: [10.1103/PhysRevLett.76.952](https://doi.org/10.1103/PhysRevLett.76.952).
- [11] Zhiming M Wang. *Self-Assembled Quantum Dots*. 1st ed. Vol. 1. Lecture Notes in Nanoscale Science and Technology 2195-2159. Springer-Verlag New York, 2008. ISBN: 978-0-387-74191-8. DOI: [10.1007/978-0-387-74191-8](https://doi.org/10.1007/978-0-387-74191-8).
- [12] M.S. Skolnick and D.J. Mowbray. "SELF-ASSEMBLED SEMICONDUCTOR QUANTUM DOTS: Fundamental Physics and Device Applications". In: *Annual Review of Materials Research* 34.1 (2004), pp. 181–218. DOI: [10.1146/annurev.matsci.34.082103.133534](https://doi.org/10.1146/annurev.matsci.34.082103.133534).
- [13] Marian A. Herman and Helmut Sitter. *Molecular Beam Epitaxy: Fundamentals and Current Status*. en. Google-Books-ID: FHPtCAAQBAJ. Springer Science & Business Media, Dec. 2012. ISBN: 978-3-642-80060-3.
- [14] K. M. Cha, K. Shibata, and K. Hirakawa. "Single electron transport through site-controlled InAs quantum dots". en. In: *Applied Physics Letters* 101.22 (Nov. 2012), p. 223115. ISSN: 0003-6951, 1077-3118. DOI: [10.1063/1.4769039](https://doi.org/10.1063/1.4769039).
- [15] J. H. Lee, Z. M. Wang, and G. J. Salamo. "The Control on Size and Density of InAs QDs by Droplet Epitaxy (April 2009)". In: *IEEE Transactions on Nanotechnology* 8.4 (July 2009), pp. 431–436. ISSN: 1536-125X. DOI: [10.1109/TNANO.2009.2021654](https://doi.org/10.1109/TNANO.2009.2021654).
- [16] Siming Chen et al. "Electrically pumped continuous-wave III–V quantum dot lasers on silicon". en. In: *Nature Photonics* 10.5 (May 2016), pp. 307–311. ISSN: 1749-4885, 1749-4893. DOI: [10.1038/nphoton.2016.21](https://doi.org/10.1038/nphoton.2016.21).
- [17] P. Martyniuk and A. Rogalski. "Quantum-dot infrared photodetectors: Status and outlook". en. In: *Progress in Quantum Electronics* 32.3-4 (Jan. 2008), pp. 89–120. ISSN: 00796727. DOI: [10.1016/j.pquantelec.2008.07.001](https://doi.org/10.1016/j.pquantelec.2008.07.001).

- [18] S Chakrabarti et al. “High-performance mid-infrared quantum dot infrared photodetectors”. en. In: *Journal of Physics D: Applied Physics* 38.13 (July 2005), pp. 2135–2141. ISSN: 0022-3727, 1361-6463. DOI: [10.1088/0022-3727/38/13/009](https://doi.org/10.1088/0022-3727/38/13/009).
- [19] J. Gérard et al. “Enhanced Spontaneous Emission by Quantum Boxes in a Monolithic Optical Microcavity”. en. In: *Physical Review Letters* 81.5 (Aug. 1998), pp. 1110–1113. ISSN: 0031-9007, 1079-7114. DOI: [10.1103/PhysRevLett.81.1110](https://doi.org/10.1103/PhysRevLett.81.1110).
- [20] M. Bayer et al. “Inhibition and Enhancement of the Spontaneous Emission of Quantum Dots in Structured Microresonators”. In: *Physical Review Letters* 86.14 (Apr. 2001), p. 3168. DOI: [10.1103/PhysRevLett.86.3168](https://doi.org/10.1103/PhysRevLett.86.3168).
- [21] H. Y. Ryu et al. “Over 30-fold enhancement of light extraction from free-standing photonic crystal slabs with InGaAs quantum dots at low temperature”. en. In: *Applied Physics Letters* 79.22 (Nov. 2001), pp. 3573–3575. ISSN: 0003-6951, 1077-3118. DOI: [10.1063/1.1420405](https://doi.org/10.1063/1.1420405).
- [22] Dirk Englund et al. “Controlling the Spontaneous Emission Rate of Single Quantum Dots in a Two-Dimensional Photonic Crystal”. en. In: *Physical Review Letters* 95.1 (July 2005), p. 013904. ISSN: 0031-9007, 1079-7114. DOI: [10.1103/PhysRevLett.95.013904](https://doi.org/10.1103/PhysRevLett.95.013904).
- [23] M. Müller et al. “On-demand generation of indistinguishable polarization-entangled photon pairs”. en. In: *Nature Photonics* 8.3 (Mar. 2014), pp. 224–228. ISSN: 1749-4885. DOI: [10.1038/nphoton.2013.377](https://doi.org/10.1038/nphoton.2013.377).
- [24] Xing Ding et al. “On-Demand Single Photons with High Extraction Efficiency and Near-Unity Indistinguishability from a Resonantly Driven Quantum Dot in a Micropillar”. In: *Physical Review Letters* 116.2 (Jan. 2016), p. 020401. DOI: [10.1103/PhysRevLett.116.020401](https://doi.org/10.1103/PhysRevLett.116.020401).
- [25] N. Somaschi et al. “Near-optimal single-photon sources in the solid state”. en. In: *Nature Photonics* 10.5 (May 2016), pp. 340–345. ISSN: 1749-4885. DOI: [10.1038/nphoton.2016.23](https://doi.org/10.1038/nphoton.2016.23).
- [26] S. Varoutsis et al. “Restoration of photon indistinguishability in the emission of a semiconductor quantum dot”. In: *Physical Review B* 72.4 (July 2005), p. 041303. DOI: [10.1103/PhysRevB.72.041303](https://doi.org/10.1103/PhysRevB.72.041303).



- [27] S. Laurent et al. "Indistinguishable single photons from a single-quantum dot in a two-dimensional photonic crystal cavity". In: *Applied Physics Letters* 87.16 (Oct. 2005), pp. 163107–163107–3. ISSN: 00036951. DOI: [doi:10.1063/1.2103397](https://doi.org/10.1063/1.2103397).
- [28] A. Kiraz, M. Atatüre, and A. Imamoglu. "Quantum-dot single-photon sources: Prospects for applications in linear optics quantum-information processing". en. In: *Physical Review A* 69.3 (Mar. 2004), p. 032305. ISSN: 1050-2947, 1094-1622. DOI: [10.1103/PhysRevA.69.032305](https://doi.org/10.1103/PhysRevA.69.032305).
- [29] Daniel Huber et al. "Highly indistinguishable and strongly entangled photons from symmetric GaAs quantum dots". en. In: *Nature Communications* 8 (May 2017), ncomms15506. ISSN: 2041-1723. DOI: [10.1038/ncomms15506](https://doi.org/10.1038/ncomms15506).
- [30] Charles Santori et al. "Triggered Single Photons from a Quantum Dot". In: *Physical Review Letters* 86.8 (Feb. 2001), p. 1502. DOI: [10.1103/PhysRevLett.86.1502](https://doi.org/10.1103/PhysRevLett.86.1502).
- [31] P. Michler et al. "A Quantum Dot Single-Photon Turnstile Device". en. In: *Science* 290.5500 (Dec. 2000), pp. 2282–2285. ISSN: 0036-8075, 1095-9203. DOI: [10.1126/science.290.5500.2282](https://doi.org/10.1126/science.290.5500.2282).
- [32] Christian Kurtsiefer et al. "Stable Solid-State Source of Single Photons". In: *Physical Review Letters* 85.2 (July 2000), pp. 290–293. DOI: [10.1103/PhysRevLett.85.290](https://doi.org/10.1103/PhysRevLett.85.290).
- [33] Matthew Pelton et al. "Efficient Source of Single Photons: A Single Quantum Dot in a Micropost Microcavity". en. In: *Physical Review Letters* 89.23 (Nov. 2002), p. 233602. ISSN: 0031-9007, 1079-7114. DOI: [10.1103/PhysRevLett.89.233602](https://doi.org/10.1103/PhysRevLett.89.233602).
- [34] Z. L. Yuan et al. "Electrically driven single-photon source". In: *Science* 295.5552 (2002), pp. 102–105.
- [35] D. C. Unitt et al. "Polarization control of quantum dot single-photon sources via a dipole-dependent Purcell effect". en. In: *Physical Review B* 72.3 (July 2005), p. 033318. ISSN: 1098-0121, 1550-235X. DOI: [10.1103/PhysRevB.72.033318](https://doi.org/10.1103/PhysRevB.72.033318).

- [36] A. Bennett et al. "High performance single photon sources from photolithographically defined pillar microcavities". In: *Optics Express* 13.1 (Jan. 2005), pp. 50–55. DOI: [10.1364/OPEX.13.000050](https://doi.org/10.1364/OPEX.13.000050).
- [37] A. Muller et al. "Creating Polarization-Entangled Photon Pairs from a Semiconductor Quantum Dot Using the Optical Stark Effect". In: *Physical Review Letters* 103.21 (Nov. 2009), p. 217402. DOI: [10.1103/PhysRevLett.103.217402](https://doi.org/10.1103/PhysRevLett.103.217402).
- [38] Ren-Bao Liu, Wang Yao, and L.J. Sham. "Quantum computing by optical control of electron spins". In: *Advances in Physics* 59.5 (2010), pp. 703–802. ISSN: 0001-8732. DOI: [10.1080/00018732.2010.505452](https://doi.org/10.1080/00018732.2010.505452).
- [39] David P. DiVincenzo. "Double Quantum Dot as a Quantum Bit". en. In: *Science* 309.5744 (Sept. 2005), pp. 2173–2174. ISSN: 0036-8075, 1095-9203. DOI: [10.1126/science.1118921](https://doi.org/10.1126/science.1118921).
- [40] E. Knill, R. Laflamme, and G. J. Milburn. "A scheme for efficient quantum computation with linear optics". en. In: *Nature* 409.6816 (Jan. 2001), pp. 46–52. ISSN: 0028-0836. DOI: [10.1038/35051009](https://doi.org/10.1038/35051009).
- [41] Xiaodong Xu et al. "Coherent Optical Spectroscopy of a Strongly Driven Quantum Dot". en. In: *Science* 317.5840 (Aug. 2007), pp. 929–932. ISSN: 0036-8075, 1095-9203. DOI: [10.1126/science.1142979](https://doi.org/10.1126/science.1142979).
- [42] David Press et al. "Complete quantum control of a single quantum dot spin using ultrafast optical pulses". en. In: *Nature* 456.7219 (Nov. 2008), pp. 218–221. ISSN: 0028-0836. DOI: [10.1038/nature07530](https://doi.org/10.1038/nature07530).
- [43] Richard J. Warburton. "Single spins in self-assembled quantum dots". en. In: *Nature Materials* 12.6 (June 2013), pp. 483–493. ISSN: 1476-1122. DOI: [10.1038/nmat3585](https://doi.org/10.1038/nmat3585).
- [44] Brian D. Gerardot et al. "Optical pumping of a single hole spin in a quantum dot". en. In: *Nature* 451.7177 (Jan. 2008). Bandiera\_abtest: a Cg\_type: Nature Research Journals Number: 7177 Primary\_atype: Research Publisher: Nature Publishing Group, pp. 441–444. ISSN: 1476-4687. DOI: [10.1038/nature06472](https://doi.org/10.1038/nature06472).
- [45] Jack Hansom et al. "Environment-assisted quantum control of a solid-state spin via coherent dark states". en. In: *Nature Physics* 10.10 (Oct. 2014), pp. 725–730. ISSN: 1745-2473. DOI: [10.1038/nphys3077](https://doi.org/10.1038/nphys3077).

- [46] Dapeng Ding et al. "Coherent Optical Control of a Quantum-Dot Spin-Qubit in a Waveguide-Based Spin-Photon Interface". In: *Physical Review Applied* 11.3 (Mar. 2019), p. 031002. DOI: [10.1103/PhysRevApplied.11.031002](https://doi.org/10.1103/PhysRevApplied.11.031002).
- [47] Charles H. Bennett and Gilles Brassard. "Quantum cryptography: Public key distribution and coin tossing". en. In: *Theoretical Computer Science* 560 (Dec. 2014), pp. 7–11. ISSN: 03043975. DOI: [10.1016/j.tcs.2014.05.025](https://doi.org/10.1016/j.tcs.2014.05.025).
- [48] Edo Waks et al. "Quantum cryptography with a photon turnstile". en. In: *Nature* 420.6917 (Dec. 2002), pp. 762–762. ISSN: 0028-0836, 1476-4687. DOI: [10.1038/420762a](https://doi.org/10.1038/420762a).
- [49] Y. Yamamoto. "Quantum communication and information processing with quantum dots". In: *Quantum Information Processing* 5.5 (2006), pp. 299–311.
- [50] Rinaldo Trotta et al. "Highly Entangled Photons from Hybrid Piezoelectric-Semiconductor Quantum Dot Devices". en. In: *Nano Letters* 14.6 (June 2014), pp. 3439–3444. ISSN: 1530-6984, 1530-6992. DOI: [10.1021/nl500968k](https://doi.org/10.1021/nl500968k).
- [51] A Kiraz et al. "Cavity-quantum electrodynamics with quantum dots". en. In: (), p. 10.
- [52] Miro Kroutvar et al. "Optically programmable electron spin memory using semiconductor quantum dots". en. In: *Nature* 432.7013 (Nov. 2004), pp. 81–84. ISSN: 0028-0836, 1476-4687. DOI: [10.1038/nature03008](https://doi.org/10.1038/nature03008).
- [53] T. Walther et al. "Nature of the Stranski-Krastanow Transition during Epitaxy of InGaAs on GaAs". In: *Physical Review Letters* 86.11 (Mar. 2001), pp. 2381–2384. DOI: [10.1103/PhysRevLett.86.2381](https://doi.org/10.1103/PhysRevLett.86.2381).
- [54] A.G. Cullis et al. "Stranski-Krastanow transition and epitaxial island growth". In: *Physical Review B* 66.8 (Aug. 2002), p. 081305. DOI: [10.1103/PhysRevB.66.081305](https://doi.org/10.1103/PhysRevB.66.081305).
- [55] D. Leonard, K. Pond, and P. M. Petroff. "Critical layer thickness for self-assembled InAs islands on GaAs". In: *Physical Review B* 50.16 (Oct. 1994), pp. 11687–11692. DOI: [10.1103/PhysRevB.50.11687](https://doi.org/10.1103/PhysRevB.50.11687).

- [56] R. Leon et al. "Spatially-Resolved Visible Luminescence of Self-Assembled Semiconductor Quantum Dots". In: *Science* 267.5206 (1995). Qq068 Times Cited:154 Cited References Count:25, pp. 1966–1968.
- [57] David P. DiVincenzo. "Quantum Computation". en. In: *Science* 270.5234 (Oct. 1995), pp. 255–261. ISSN: 0036-8075, 1095-9203. DOI: [10.1126/science.270.5234.255](https://doi.org/10.1126/science.270.5234.255).
- [58] Xiaodong Xu et al. "Fast Spin State Initialization in a Singly Charged InAs-GaAs Quantum Dot by Optical Cooling". In: *Physical Review Letters* 99.9 (Aug. 2007), p. 097401. DOI: [10.1103/PhysRevLett.99.097401](https://doi.org/10.1103/PhysRevLett.99.097401).
- [59] J. Berezovsky et al. "Picosecond Coherent Optical Manipulation of a Single Electron Spin in a Quantum Dot". en. In: *Science* 320.5874 (Apr. 2008), pp. 349–352. ISSN: 0036-8075, 1095-9203. DOI: [10.1126/science.1154798](https://doi.org/10.1126/science.1154798).
- [60] E. B. Flagg and Glenn S. Solomon. "Optical spin readout method in a quantum dot using the ac Stark effect". In: *Physical Review B* 92.24 (Dec. 2015), p. 245309. DOI: [10.1103/PhysRevB.92.245309](https://doi.org/10.1103/PhysRevB.92.245309).
- [61] J. M. Elzerman et al. "Few-electron quantum dot circuit with integrated charge read out". en. In: *Physical Review B* 67.16 (Apr. 2003), p. 161308. ISSN: 0163-1829, 1095-3795. DOI: [10.1103/PhysRevB.67.161308](https://doi.org/10.1103/PhysRevB.67.161308).
- [62] J. M. Elzerman et al. "Single-shot read-out of an individual electron spin in a quantum dot". en. In: *Nature* 430.6998 (July 2004), pp. 431–435. ISSN: 0028-0836. DOI: [10.1038/nature02693](https://doi.org/10.1038/nature02693).
- [63] Gert Schedelbeck et al. "Coupled Quantum Dots Fabricated by Cleaved Edge Overgrowth: From Artificial Atoms to Molecules". en. In: *Science* 278.5344 (Dec. 1997), pp. 1792–1795. ISSN: 0036-8075, 1095-9203. DOI: [10.1126/science.278.5344.1792](https://doi.org/10.1126/science.278.5344.1792).
- [64] A Hartmann et al. "Structure and optical properties of semiconductor quantum nanostructures self-formed in inverted tetrahedral pyramids". en. In: *Journal of Physics: Condensed Matter* 11.31 (Aug. 1999), pp. 5901–5915. ISSN: 0953-8984, 1361-648X. DOI: [10.1088/0953-8984/11/31/302](https://doi.org/10.1088/0953-8984/11/31/302).
- [65] N. P. Kobayashi et al. "*In situ*, atomic force microscope studies of the evolution of InAs three-dimensional islands on GaAs(001)". en. In: *Applied Physics Letters* 68.23 (June 1996), pp. 3299–3301. ISSN: 0003-6951, 1077-3118. DOI: [10.1063/1.116580](https://doi.org/10.1063/1.116580).

- [66] A. S. Bhatti et al. "Optical spectroscopy of quasimonolayer InAs at the onset of quantum-dot nucleation". In: *Physical Review B* 60.4 (July 1999), pp. 2592–2598. DOI: [10.1103/PhysRevB.60.2592](https://doi.org/10.1103/PhysRevB.60.2592).
- [67] H. Benisty, H. De Neve, and C. Weisbuch. "Impact of planar microcavity effects on light extraction-Part II: selected exact simulations and role of photon recycling". English. In: *IEEE Journal of Quantum Electronics* 34.9 (Sept. 1998), pp. 1632–1643. ISSN: 0018-9197. DOI: [10.1109/3.709579](https://doi.org/10.1109/3.709579).
- [68] Pascale Senellart, Glenn Solomon, and Andrew White. "High-performance semiconductor quantum-dot single-photon sources". en. In: *Nature Nanotechnology* 12.11 (Nov. 2017), pp. 1026–1039. ISSN: 1748-3387, 1748-3395. DOI: [10.1038/nnano.2017.218](https://doi.org/10.1038/nnano.2017.218).
- [69] Hui Wang et al. "Towards optimal single-photon sources from polarized microcavities". en. In: *Nature Photonics* 13.11 (Nov. 2019), pp. 770–775. ISSN: 1749-4893. DOI: [10.1038/s41566-019-0494-3](https://doi.org/10.1038/s41566-019-0494-3).
- [70] T. Heindel et al. "Electrically driven quantum dot-micropillar single photon source with 34% overall efficiency". In: *Applied Physics Letters* 96.1 (Jan. 2010), pp. 011107–011107–3. ISSN: 00036951. DOI: [doi:10.1063/1.3284514](https://doi.org/10.1063/1.3284514).
- [71] G. S. Solomon, M. Pelton, and Y. Yamamoto. "Single-mode Spontaneous Emission from a Single Quantum Dot in a Three-Dimensional Microcavity". en. In: *Physical Review Letters* 86.17 (Apr. 2001), pp. 3903–3906. ISSN: 0031-9007, 1079-7114. DOI: [10.1103/PhysRevLett.86.3903](https://doi.org/10.1103/PhysRevLett.86.3903).
- [72] Charles Santori et al. "Indistinguishable photons from a single-photon device". en. In: *Nature* 419.6907 (Oct. 2002), pp. 594–597. ISSN: 0028-0836, 1476-4687. DOI: [10.1038/nature01086](https://doi.org/10.1038/nature01086).
- [73] Antonio Badolato et al. "Deterministic Coupling of Single Quantum Dots to Single Nanocavity Modes". In: *Science* 308.5725 (May 2005), pp. 1158–1161. DOI: [10.1126/science.1109815](https://doi.org/10.1126/science.1109815).
- [74] D. H. Ahn et al. "A broad-band planar-microcavity quantum-dot single-photon source with a solid immersion lens". en. In: *Applied Physics Letters* 118.17 (Apr. 2021), p. 174001. ISSN: 0003-6951, 1077-3118. DOI: [10.1063/5.0046065](https://doi.org/10.1063/5.0046065).

- [75] N. Srocka et al. "Enhanced photon-extraction efficiency from InGaAs/-GaAs quantum dots in deterministic photonic structures at  $1.3 \mu\text{m}$  fabricated by in-situ electron-beam lithography". en. In: *AIP Advances* 8.8 (Aug. 2018), p. 085205. ISSN: 2158-3226. DOI: [10.1063/1.5038137](https://doi.org/10.1063/1.5038137).
- [76] T. Heindel et al. "A bright triggered twin-photon source in the solid state". en. In: *Nature Communications* 8.1 (Apr. 2017), p. 14870. ISSN: 2041-1723. DOI: [10.1038/ncomms14870](https://doi.org/10.1038/ncomms14870).
- [77] Yu-Ming He et al. "On-demand semiconductor single-photon source with near-unity indistinguishability". en. In: *Nature Nanotechnology* 8.3 (Mar. 2013), pp. 213–217. ISSN: 1748-3387. DOI: [10.1038/nnano.2012.262](https://doi.org/10.1038/nnano.2012.262).
- [78] Andrei Schliwa, Momme Winkelkemper, and Dieter Bimberg. "Impact of size, shape, and composition on piezoelectric effects and electronic properties of In ( Ga ) As / Ga As quantum dots". en. In: *Physical Review B* 76.20 (Nov. 2007), p. 205324. ISSN: 1098-0121, 1550-235X. DOI: [10.1103/PhysRevB.76.205324](https://doi.org/10.1103/PhysRevB.76.205324).
- [79] Gustavo A. Narvaez, Gabriel Bester, and Alex Zunger. "Carrier relaxation mechanisms in self-assembled (In,Ga)As/GaAs quantum dots: Efficient P->S Auger relaxation of electrons". In: *Physical Review B* 74.7 (Aug. 2006), p. 075403. DOI: [10.1103/PhysRevB.74.075403](https://doi.org/10.1103/PhysRevB.74.075403).
- [80] Praket P. Jha and Philippe Guyot-Sionnest. "Trion Decay in Colloidal Quantum Dots". In: *ACS Nano* 3.4 (Apr. 2009), pp. 1011–1015. ISSN: 1936-0851. DOI: [10.1021/nm9001177](https://doi.org/10.1021/nm9001177).
- [81] Young-Shin Park et al. "Auger Recombination of Biexcitons and Negative and Positive Trions in Individual Quantum Dots". In: *ACS Nano* 8.7 (July 2014), pp. 7288–7296. ISSN: 1936-0851. DOI: [10.1021/nm5023473](https://doi.org/10.1021/nm5023473).
- [82] Annika Kurzmann et al. "Auger Recombination in Self-Assembled Quantum Dots: Quenching and Broadening of the Charged Exciton Transition". In: *Nano Letters* 16.5 (May 2016), pp. 3367–3372. ISSN: 1530-6984. DOI: [10.1021/acs.nanolett.6b01082](https://doi.org/10.1021/acs.nanolett.6b01082).
- [83] M. Bayer et al. "Fine structure of neutral and charged excitons in self-assembled In(Ga)As/(Al)GaAs quantum dots". In: *Physical Review B* 65.19 (May 2002), p. 195315. DOI: [10.1103/PhysRevB.65.195315](https://doi.org/10.1103/PhysRevB.65.195315).

- [84] J. G. Tischler et al. "Fine structure of trions and excitons in single GaAs quantum dots". en. In: *Physical Review B* 66.8 (Aug. 2002), p. 081310. ISSN: 0163-1829, 1095-3795. DOI: [10.1103/PhysRevB.66.081310](https://doi.org/10.1103/PhysRevB.66.081310).
- [85] E. Steimetz et al. "Stranski-Krastanov formation of InAs quantum dots monitored during growth by reflectance anisotropy spectroscopy and spectroscopic ellipsometry". In: *Journal of Crystal Growth* 170.1-4 (1997), pp. 208–214.
- [86] J. S Lee et al. "In<sub>0.5</sub>Ga<sub>0.5</sub>As quantum dot intermixing and evaporation in GaAs capping layer growth". In: *Journal of Applied Physics* 84.12 (1998). 144BJ Times Cited:17 Cited References Count:7, pp. 6686–6688.
- [87] Y. M. Manz et al. "Optical and structural anisotropy of InP/GaInP quantum dots for laser applications". en. In: *Applied Physics Letters* 83.5 (Aug. 2003), pp. 887–889. ISSN: 0003-6951, 1077-3118. DOI: [10.1063/1.1598290](https://doi.org/10.1063/1.1598290).
- [88] Takashi Kita et al. "Multidirectional observation of an embedded quantum dot". en. In: *Applied Physics Letters* 90.4 (Jan. 2007), p. 041911. ISSN: 0003-6951, 1077-3118. DOI: [10.1063/1.2436633](https://doi.org/10.1063/1.2436633).
- [89] L. Besombes, K. Kheng, and D. Martrou. "Exciton and Biexciton Fine Structure in Single Elongated Islands Grown on a Vicinal Surface". en. In: *Physical Review Letters* 85.2 (July 2000), pp. 425–428. ISSN: 0031-9007, 1079-7114. DOI: [10.1103/PhysRevLett.85.425](https://doi.org/10.1103/PhysRevLett.85.425).
- [90] E. Blackwood et al. "Exchange interaction of excitons in GaAs heterostructures". In: *Physical Review B* 50.19 (Nov. 1994), pp. 14246–14254. DOI: [10.1103/PhysRevB.50.14246](https://doi.org/10.1103/PhysRevB.50.14246).
- [91] E. L. Ivchenko. "Fine Structure of Excitonic Levels in Semiconductor Nanostructures". en. In: *physica status solidi (a)* 164.1 (Nov. 1997), pp. 487–492. ISSN: 1521-396X. DOI: [10.1002/1521-396X\(199711\)164:1<487::AID-PSSA487>3.0.CO;2-1](https://doi.org/10.1002/1521-396X(199711)164:1<487::AID-PSSA487>3.0.CO;2-1).
- [92] M. Bayer et al. "Electron and Hole g Factors and Exchange Interaction from Studies of the Exciton Fine Structure in In<sub>0.60</sub>Ga<sub>0.40</sub>As Quantum Dots". In: *Physical Review Letters* 82.8 (Feb. 1999), p. 1748. DOI: [10.1103/PhysRevLett.82.1748](https://doi.org/10.1103/PhysRevLett.82.1748).



- [93] V. D. Kulakovskii et al. "Fine Structure of Biexciton Emission in Symmetric and Asymmetric CdSe/ZnSe Single Quantum Dots". In: *Physical Review Letters* 82.8 (Feb. 1999), pp. 1780–1783. DOI: [10.1103/PhysRevLett.82.1780](https://doi.org/10.1103/PhysRevLett.82.1780).
- [94] H. Kamada et al. "Excited-state optical transitions of excitons and biexcitons in a single  $\text{In}_x\text{Ga}_{1-x}\text{As}$  quantum disk". In: *Physical Review B* 58.24 (Dec. 1998), pp. 16243–16251. DOI: [10.1103/PhysRevB.58.16243](https://doi.org/10.1103/PhysRevB.58.16243).
- [95] Haiming Zhu et al. "Charge Transfer Dynamics from Photoexcited Semiconductor Quantum Dots". In: *Annual Review of Physical Chemistry* 67.1 (2016). \_eprint: <https://doi.org/10.1146/annurev-physchem-040215-112128>, pp. 259–281. DOI: [10.1146/annurev-physchem-040215-112128](https://doi.org/10.1146/annurev-physchem-040215-112128).
- [96] Disheng Chen et al. "Characterization of the local charge environment of a single quantum dot via resonance fluorescence". In: *Physical Review B* 93.11 (Mar. 2016), p. 115307. DOI: [10.1103/PhysRevB.93.115307](https://doi.org/10.1103/PhysRevB.93.115307).
- [97] O. Gazzano et al. "Effects of resonant-laser excitation on the emission properties in a single quantum dot". EN. In: *Optica* 5.4 (Apr. 2018), pp. 354–359. ISSN: 2334-2536. DOI: [10.1364/OPTICA.5.000354](https://doi.org/10.1364/OPTICA.5.000354).
- [98] Hai Son Nguyen et al. "Photoneutralization and slow capture of carriers in quantum dots probed by resonant excitation spectroscopy". In: *Physical Review B* 87.11 (Mar. 2013), p. 115305. DOI: [10.1103/PhysRevB.87.115305](https://doi.org/10.1103/PhysRevB.87.115305).
- [99] Gary R. Lander et al. "Charging dynamics of single InAs quantum dots under both resonant and above-band excitation". In: *arXiv:1812.07672 [cond-mat, physics:quant-ph]* (Dec. 2018). arXiv: 1812.07672.
- [100] R. J. Warburton et al. "Optical emission from a charge-tunable quantum ring". en. In: *Nature* 405.6789 (June 2000), pp. 926–929. ISSN: 0028-0836. DOI: [10.1038/35016030](https://doi.org/10.1038/35016030).
- [101] M. Ediger et al. "Controlled generation of neutral, negatively-charged and positively-charged excitons in the same single quantum dot". In: *Applied Physics Letters* 86.21 (May 2005), p. 211909. ISSN: 0003-6951, 1077-3118. DOI: [10.1063/1.1937996](https://doi.org/10.1063/1.1937996).



- [102] M. Baier et al. "Optical spectroscopy of charged excitons in single quantum dot photodiodes". In: *Physical Review B* 64.19 (Oct. 2001), p. 195326. DOI: [10.1103/PhysRevB.64.195326](https://doi.org/10.1103/PhysRevB.64.195326).
- [103] Matthias C. Löbl et al. "Narrow optical linewidths and spin pumping on charge-tunable close-to-surface self-assembled quantum dots in an ultra-thin diode". en. In: *Physical Review B* 96.16 (Oct. 2017), p. 165440. ISSN: 2469-9950, 2469-9969. DOI: [10.1103/PhysRevB.96.165440](https://doi.org/10.1103/PhysRevB.96.165440).
- [104] George Gabriel Stokes, Joseph Larmor, and John William Strutt Rayleigh. *Mathematical and physical papers*. eng. Cambridge : University Press, 1880.
- [105] William A. Shurcliff. *Polarized Light: Production and Use*. en. Publication Title: Polarized Light. Harvard University Press, Oct. 2013. ISBN: 978-0-674-42413-5. DOI: [10.4159/harvard.9780674424135](https://doi.org/10.4159/harvard.9780674424135).
- [106] E. Wolf. "Optics in terms of observable quantities". en. In: *Il Nuovo Cimento (1943-1954)* 12.6 (Dec. 1954), pp. 884–888. ISSN: 1827-6121. DOI: [10.1007/BF02781855](https://doi.org/10.1007/BF02781855).
- [107] Eugene Hecht. *Optics*. en. 5 ed. Boston: Pearson Education, Inc, 2017. ISBN: 978-0-13-397722-6.
- [108] Beth Schaefer et al. "Measuring the Stokes polarization parameters". In: *American Journal of Physics* 75.2 (Jan. 2007), pp. 163–168. ISSN: 0002-9505. DOI: [10.1119/1.2386162](https://doi.org/10.1119/1.2386162).
- [109] Andrew Zangwill. *Modern Electrodynamics*: en. 1st ed. Cambridge University Press, Dec. 2012. ISBN: 978-1-139-03477-7. DOI: [10.1017/CB09781139034777](https://doi.org/10.1017/CB09781139034777).
- [110] Edward Collett. "The Description of Polarization in Classical Physics". en. In: *American Journal of Physics* 36.8 (Aug. 1968), pp. 713–725. ISSN: 0002-9505, 1943-2909. DOI: [10.1119/1.1975098](https://doi.org/10.1119/1.1975098).
- [111] M. O Scully and M. S Zubairy. *Quantum Optics*. University Press, Cambridge, U. K., 1997.
- [112] C. Cohen-Tannoudji and S. Reynaud. "Dressed-atom description of resonance fluorescence and absorption spectra of a multi-level atom in an intense laser beam". en. In: *Journal of Physics B: Atomic and Molecular Physics* 10.3 (1977), p. 345. ISSN: 0022-3700. DOI: [10.1088/0022-3700/10/3/005](https://doi.org/10.1088/0022-3700/10/3/005).

- [113] B. R. Mollow. "Power Spectrum of Light Scattered by Two-Level Systems". In: *Physical Review* 188.5 (Dec. 1969), pp. 1969–1975. DOI: [10.1103/PhysRev.188.1969](https://doi.org/10.1103/PhysRev.188.1969).
- [114] Joseph W Goodman. *Introduction to Fourier Optics*. McGraw-Hill, 1996.
- [115] N. A. Vamivakas et al. "Spin-resolved quantum-dot resonance fluorescence". In: *Nature Physics* 5.3 (Jan. 2009), pp. 198–202. ISSN: 1745-2473, 1745-2481. DOI: [10.1038/nphys1182](https://doi.org/10.1038/nphys1182).
- [116] Andreas V. Kuhlmann et al. "A dark-field microscope for background-free detection of resonance fluorescence from single semiconductor quantum dots operating in a set-and-forget mode". In: *Review of Scientific Instruments* 84.7 (July 2013), p. 073905. ISSN: 0034-6748, 1089-7623. DOI: [10.1063/1.4813879](https://doi.org/10.1063/1.4813879).
- [117] A. Muller et al. "Resonance Fluorescence from a Coherently Driven Semiconductor Quantum Dot in a Cavity". In: *Physical Review Letters* 99.18 (Nov. 2007), p. 187402. ISSN: 0031-9007, 1079-7114. DOI: [10.1103/PhysRevLett.99.187402](https://doi.org/10.1103/PhysRevLett.99.187402).
- [118] Disheng Chen, Gary R. Lander, and Edward B. Flagg. "Resonance Fluorescence of an InGaAs Quantum Dot in a Planar Cavity Using Orthogonal Excitation and Detection". In: *JoVE (Journal of Visualized Experiments)* 128 (Oct. 2017), e56435–e56435. ISSN: 1940-087X. DOI: [10.3791/56435](https://doi.org/10.3791/56435).
- [119] Alexei L. Glebov et al. "Volume Bragg gratings as ultra-narrow and multiband optical filters". In: *Micro-Optics 2012*. Vol. 8428. International Society for Optics and Photonics, May 2012, p. 84280C. DOI: [10.1117/12.923575](https://doi.org/10.1117/12.923575).
- [120] Leonid B. Glebov. "High brightness laser design based on volume Bragg gratings". en. In: ed. by Gary L. Wood and Mark A. Dubinskii. Orlando (Kissimmee), FL, May 2006, p. 621601. DOI: [10.1117/12.667196](https://doi.org/10.1117/12.667196).
- [121] Francesco Pagliano et al. "Dynamically controlling the emission of single excitons in photonic crystal cavities". en. In: *Nature Communications* 5.1 (Dec. 2014), p. 5786. ISSN: 2041-1723. DOI: [10.1038/ncomms6786](https://doi.org/10.1038/ncomms6786).

- [122] Je-Hyung Kim et al. "Super-Radiant Emission from Quantum Dots in a Nanophotonic Waveguide". en. In: *Nano Letters* 18.8 (Aug. 2018), pp. 4734–4740. ISSN: 1530-6984, 1530-6992. DOI: [10.1021/acs.nanolett.8b01133](https://doi.org/10.1021/acs.nanolett.8b01133).
- [123] Andrei Faraon et al. "Local quantum dot tuning on photonic crystal chips". en. In: *Applied Physics Letters* 90.21 (May 2007), p. 213110. ISSN: 0003-6951, 1077-3118. DOI: [10.1063/1.2742789](https://doi.org/10.1063/1.2742789).
- [124] Timothy M. Sweeney et al. "Cavity-stimulated Raman emission from a single quantum dot spin". en. In: *Nature Photonics* 8.6 (June 2014), pp. 442–447. ISSN: 1749-4885, 1749-4893. DOI: [10.1038/nphoton.2014.84](https://doi.org/10.1038/nphoton.2014.84).
- [125] G. Fernandez et al. "Optically Tunable Spontaneous Raman Fluorescence from a Single Self-Assembled InGaAs Quantum Dot". en. In: *Physical Review Letters* 103.8 (Aug. 2009), p. 087406. ISSN: 0031-9007, 1079-7114. DOI: [10.1103/PhysRevLett.103.087406](https://doi.org/10.1103/PhysRevLett.103.087406).
- [126] Jianping Wang et al. "Towards Scalable Entangled Photon Sources with Self-Assembled InAs / GaAs Quantum Dots". en. In: *Physical Review Letters* 115.6 (Aug. 2015), p. 067401. ISSN: 0031-9007, 1079-7114. DOI: [10.1103/PhysRevLett.115.067401](https://doi.org/10.1103/PhysRevLett.115.067401).
- [127] Yan Chen et al. "Wavelength-tunable entangled photons from silicon-integrated III–V quantum dots". en. In: *Nature Communications* 7 (Jan. 2016), p. 10387. ISSN: 2041-1723. DOI: [10.1038/ncomms10387](https://doi.org/10.1038/ncomms10387).
- [128] Joel Q. Grim et al. "Scalable in operando strain tuning in nanophotonic waveguides enabling three-quantum-dot superradiance". en. In: *Nature Materials* 18.9 (Sept. 2019), pp. 963–969. ISSN: 1476-4660. DOI: [10.1038/s41563-019-0418-0](https://doi.org/10.1038/s41563-019-0418-0).
- [129] Johannes D Plumhof et al. "Experimental methods of post-growth tuning of the excitonic fine structure splitting in semiconductor quantum dots". en. In: *Nanoscale Research Letters* 7.1 (Dec. 2012), p. 336. ISSN: 1556-276X. DOI: [10.1186/1556-276X-7-336](https://doi.org/10.1186/1556-276X-7-336).
- [130] Luca Sapienza et al. "Nanoscale optical positioning of single quantum dots for bright and pure single-photon emission". en. In: *Nature Communications* 6 (July 2015). DOI: [10.1038/ncomms8833](https://doi.org/10.1038/ncomms8833).

- [131] Yu-Ming He et al. "Deterministic implementation of a bright, on-demand single-photon source with near-unity indistinguishability via quantum dot imaging". EN. In: *Optica* 4.7 (July 2017). Publisher: Optical Society of America, pp. 802–808. ISSN: 2334-2536. DOI: [10.1364/OPTICA.4.000802](https://doi.org/10.1364/OPTICA.4.000802).
- [132] Jin Liu et al. "Cryogenic photoluminescence imaging system for nanoscale positioning of single quantum emitters". en. In: *Review of Scientific Instruments* 88.2 (Feb. 2017), p. 023116. ISSN: 0034-6748, 1089-7623. DOI: [10.1063/1.4976578](https://doi.org/10.1063/1.4976578).
- [133] Jin Liu et al. "Single Self-Assembled InAs/GaAs Quantum Dots in Photonic Nanostructures: The Role of Nanofabrication". In: *Physical Review Applied* 9.6 (June 2018), p. 064019. DOI: [10.1103/PhysRevApplied.9.064019](https://doi.org/10.1103/PhysRevApplied.9.064019).
- [134] Jiquan Wang et al. "Multi-offspring genetic algorithm and its application to the traveling salesman problem". en. In: *Applied Soft Computing* 43 (June 2016), pp. 415–423. ISSN: 15684946. DOI: [10.1016/j.asoc.2016.02.021](https://doi.org/10.1016/j.asoc.2016.02.021).
- [135] Zakir H Ahmed. "Genetic Algorithm for the Traveling Salesman Problem using Sequential Constructive Crossover Operator". en. In: *International Journal of Biometrics* (), p. 10.
- [136] Andreas Muller et al. "Ultrahigh-finesse, low-mode-volume Fabry–Perot microcavity". en. In: (), p. 3.
- [137] M. Shirasaki. "Large angular dispersion by a virtually imaged phased array and its application to a wavelength demultiplexer". en. In: *Optics Letters* 21.5 (Mar. 1996), p. 366. ISSN: 0146-9592, 1539-4794. DOI: [10.1364/OL.21.000366](https://doi.org/10.1364/OL.21.000366).
- [138] Masataka Shirasaki. "Virtually Imaged Phased Array". en. In: *FUJITSU Sci. Tech. J.* (1999), p. 13.
- [139] T. A. Wilkinson et al. "Complete Stokes vector analysis with a compact, portable rotating waveplate polarimeter". In: *Review of Scientific Instruments* 92.9 (Sept. 2021). Publisher: American Institute of Physics, p. 093101. ISSN: 0034-6748. DOI: [10.1063/5.0052835](https://doi.org/10.1063/5.0052835).

- [140] Matthew R. Foreman and Peter Török. "Information and resolution in electromagnetic optical systems". en. In: *Physical Review A* 82.4 (Oct. 2010), p. 043835. ISSN: 1050-2947, 1094-1622. DOI: [10.1103/PhysRevA.82.043835](https://doi.org/10.1103/PhysRevA.82.043835).
- [141] J. Noda, K. Okamoto, and Y. Sasaki. "Polarization-maintaining fibers and their applications". In: *Journal of Lightwave Technology* 4.8 (Aug. 1986). Conference Name: Journal of Lightwave Technology, pp. 1071–1089. ISSN: 1558-2213. DOI: [10.1109/JLT.1986.1074847](https://doi.org/10.1109/JLT.1986.1074847).
- [142] Juan M. Bueno. "Polarimetry using liquid-crystal variable retarders: theory and calibration". en. In: *Journal of Optics A: Pure and Applied Optics* 2.3 (May 2000). Publisher: IOP Publishing, pp. 216–222. ISSN: 1464-4258. DOI: [10.1088/1464-4258/2/3/308](https://doi.org/10.1088/1464-4258/2/3/308).
- [143] Paul A. Williams. "Rotating-wave-plate Stokes polarimeter for differential group delay measurements of polarization-mode dispersion". EN. In: *Applied Optics* 38.31 (Nov. 1999), pp. 6508–6515. ISSN: 1539-4522. DOI: [10.1364/AO.38.006508](https://doi.org/10.1364/AO.38.006508).
- [144] Søren Bobach et al. "Note: A portable rotating waveplate polarimeter". In: *Review of Scientific Instruments* 88.3 (Mar. 2017), p. 036101. ISSN: 0034-6748. DOI: [10.1063/1.4977220](https://doi.org/10.1063/1.4977220).
- [145] Matthew J. Romerein et al. "Calibration method using a single retarder to simultaneously measure polarization and fully characterize a polarimeter over a broad range of wavelengths". EN. In: *Applied Optics* 50.28 (Oct. 2011), pp. 5382–5389. ISSN: 1539-4522. DOI: [10.1364/AO.50.005382](https://doi.org/10.1364/AO.50.005382).
- [146] Toshiki Kihara. "Measurement method of Stokes parameters using a quarter-wave plate with phase difference errors". EN. In: *Applied Optics* 50.17 (June 2011), pp. 2582–2587. ISSN: 1539-4522. DOI: [10.1364/AO.50.002582](https://doi.org/10.1364/AO.50.002582).
- [147] S. Arnoldt. "Rotating Quarter-Wave Plate Stokes Polarimeter". Bachelors Thesis. Universität Bonn, Oct. 2011.
- [148] C. Flueraru et al. "Error Analysis of a Rotating Quarter-Wave Plate Stokes' Polarimeter". In: *IEEE Transactions on Instrumentation and Measurement* 57.4 (Apr. 2008), pp. 731–735. ISSN: 0018-9456. DOI: [10.1109/TIM.2007.913752](https://doi.org/10.1109/TIM.2007.913752).

- [149] H. G. Berry, G. Gabrielse, and A. E. Livingston. "Measurement of the Stokes parameters of light". EN. In: *Applied Optics* 16.12 (Dec. 1977), pp. 3200–3205. ISSN: 1539-4522. DOI: [10.1364/AO.16.003200](https://doi.org/10.1364/AO.16.003200).
- [150] P. S. Hauge. "Survey Of Methods For The Complete Determination Of A State Of Polarization". In: *Polarized Light: Instruments, Devices, Applications*. Vol. 0088. International Society for Optics and Photonics, Oct. 1976, pp. 3–10. DOI: [10.1117/12.955006](https://doi.org/10.1117/12.955006).
- [151] Richard Anderson. "Measurement of Mueller matrices". In: *Applied Optics* 31.1 (Jan. 1992), pp. 11–13. DOI: [10.1364/AO.31.000011](https://doi.org/10.1364/AO.31.000011).
- [152] Eric Compain, Stéphane Poirier, and Bernard Drevillon. "General and Self-Consistent Method for the Calibration of Polarization Modulators, Polarimeters, and Mueller-Matrix Ellipsometers". en. In: *Applied Optics* 38.16 (June 1999), p. 3490. ISSN: 0003-6935, 1539-4522. DOI: [10.1364/AO.38.003490](https://doi.org/10.1364/AO.38.003490).
- [153] Robert L. Brooks and Eric H. Pinnington. "Polarization measurements of He i singlet transitions following beam-tilted-foil excitation". en. In: *Physical Review A* 18.4 (Oct. 1978), pp. 1454–1458. ISSN: 0556-2791. DOI: [10.1103/PhysRevA.18.1454](https://doi.org/10.1103/PhysRevA.18.1454).
- [154] Zheng Ping Wang et al. "Novel method for measurement of retardance of a quarter-wave plate". In: *Optics & Laser Technology* 36.4 (June 2004), pp. 285–290. ISSN: 0030-3992. DOI: [10.1016/j.optlastec.2003.09.011](https://doi.org/10.1016/j.optlastec.2003.09.011).
- [155] Zheng Ping Wang et al. "Method of measuring the practical retardance and judging the fast or slow axis of a quarter-wave plate". In: *Measurement* 39.8 (Oct. 2006), pp. 729–735. ISSN: 0263-2241. DOI: [10.1016/j.measurement.2006.03.005](https://doi.org/10.1016/j.measurement.2006.03.005).
- [156] T. A. Wilkinson et al. "Spin-selective AC Stark shifts in a charged quantum dot". In: *Applied Physics Letters* 114.13 (Apr. 2019), p. 133104. ISSN: 0003-6951. DOI: [10.1063/1.5084244](https://doi.org/10.1063/1.5084244).
- [157] T. A. Wilkinson et al. "Dynamic nuclear polarization in a charged quantum dot induced by the AC Stark effect". In: *Quantum Nanophotonic Materials, Devices, and Systems 2019*. Vol. 11091. International Society for Optics and Photonics, Sept. 2019, p. 110910I. DOI: [10.1117/12.2529455](https://doi.org/10.1117/12.2529455).

- [158] A. Imamoglu et al. “Quantum Information Processing Using Quantum Dot Spins and Cavity QED”. In: *Physical Review Letters* 83.20 (Nov. 1999), pp. 4204–4207. DOI: [10.1103/PhysRevLett.83.4204](https://doi.org/10.1103/PhysRevLett.83.4204).
- [159] Christoph Kloeffel and Daniel Loss. “Prospects for Spin-Based Quantum Computing in Quantum Dots”. In: *Annual Review of Condensed Matter Physics* 4.1 (2013), pp. 51–81. DOI: [10.1146/annurev-conmatphys-030212-184248](https://doi.org/10.1146/annurev-conmatphys-030212-184248).
- [160] Aymeric Delteil et al. “Observation of Quantum Jumps of a Single Quantum Dot Spin Using Submicrosecond Single-Shot Optical Readout”. In: *Physical Review Letters* 112.11 (Mar. 2014), p. 116802. DOI: [10.1103/PhysRevLett.112.116802](https://doi.org/10.1103/PhysRevLett.112.116802).
- [161] E. A. Chekhovich et al. “Pumping of Nuclear Spins by Optical Excitation of Spin-Forbidden Transitions in a Quantum Dot”. In: *Physical Review Letters* 104.6 (Feb. 2010), p. 066804. DOI: [10.1103/PhysRevLett.104.066804](https://doi.org/10.1103/PhysRevLett.104.066804).
- [162] B. Eble et al. “Dynamic nuclear polarization of a single charge-tunable InAs/GaAs quantum dot”. In: *Physical Review B* 74.8 (Aug. 2006), p. 081306. DOI: [10.1103/PhysRevB.74.081306](https://doi.org/10.1103/PhysRevB.74.081306).
- [163] E. A. Chekhovich et al. “Nuclear spin effects in semiconductor quantum dots”. en. In: *Nature Materials* 12.6 (June 2013), pp. 494–504. ISSN: 1476-1122. DOI: [10.1038/nmat3652](https://doi.org/10.1038/nmat3652).
- [164] C. W. Lai et al. “Knight-Field-Enabled Nuclear Spin Polarization in Single Quantum Dots”. In: *Physical Review Letters* 96.16 (Apr. 2006), p. 167403. DOI: [10.1103/PhysRevLett.96.167403](https://doi.org/10.1103/PhysRevLett.96.167403).
- [165] A. S. Bracker et al. “Optical Pumping of the Electronic and Nuclear Spin of Single Charge-Tunable Quantum Dots”. In: *Physical Review Letters* 94.4 (Feb. 2005), p. 047402. DOI: [10.1103/PhysRevLett.94.047402](https://doi.org/10.1103/PhysRevLett.94.047402).
- [166] A. I. Tartakovskii et al. “Nuclear Spin Switch in Semiconductor Quantum Dots”. In: *Physical Review Letters* 98.2 (Jan. 2007), p. 026806. DOI: [10.1103/PhysRevLett.98.026806](https://doi.org/10.1103/PhysRevLett.98.026806).
- [167] Bernhard Urbaszek et al. “Nuclear spin physics in quantum dots: an optical investigation”. In: *Reviews of Modern Physics* 85.1 (Jan. 2013). arXiv:1202.4637 [cond-mat], pp. 79–133. ISSN: 0034-6861, 1539-0756. DOI: [10.1103/RevModPhys.85.79](https://doi.org/10.1103/RevModPhys.85.79).



- [168] H. D. Robinson and B. B. Goldberg. “Light-induced spectral diffusion in single self-assembled quantum dots”. In: *Physical Review B* 61.8 (Feb. 2000), R5086–R5089. DOI: [10.1103/PhysRevB.61.R5086](https://doi.org/10.1103/PhysRevB.61.R5086).
- [169] M. Abbarchi et al. “Spectral diffusion and line broadening in single self-assembled GaAs/AlGaAs quantum dot photoluminescence”. In: *Applied Physics Letters* 93.16 (2008), p. 162101. ISSN: 00036951. DOI: [10.1063/1.3003578](https://doi.org/10.1063/1.3003578).
- [170] Andreas V. Kuhlmann et al. “Charge noise and spin noise in a semiconductor quantum device”. en. In: *Nature Physics* 9.9 (Sept. 2013), pp. 570–575. ISSN: 1745-2473. DOI: [10.1038/nphys2688](https://doi.org/10.1038/nphys2688).
- [171] Hailin Wang et al. “Transient nonlinear optical response from excitation induced dephasing in GaAs”. en. In: *Physical Review Letters* 71.8 (Aug. 1993), pp. 1261–1264. ISSN: 0031-9007. DOI: [10.1103/PhysRevLett.71.1261](https://doi.org/10.1103/PhysRevLett.71.1261).
- [172] H. C. Schneider, W. W. Chow, and S. W. Koch. “Excitation-induced dephasing in semiconductor quantum dots”. en. In: *Physical Review B* 70.23 (Dec. 2004), p. 235308. ISSN: 1098-0121, 1550-235X. DOI: [10.1103/PhysRevB.70.235308](https://doi.org/10.1103/PhysRevB.70.235308).
- [173] Léonard Monniello et al. “Excitation-Induced Dephasing in a Resonantly Driven InAs / GaAs Quantum Dot”. en. In: *Physical Review Letters* 111.2 (July 2013), p. 026403. ISSN: 0031-9007, 1079-7114. DOI: [10.1103/PhysRevLett.111.026403](https://doi.org/10.1103/PhysRevLett.111.026403).
- [174] Florentin Reiter and Anders S. Sørensen. “Effective operator formalism for open quantum systems”. In: *Physical Review A* 85.3 (Mar. 2012), p. 032111. DOI: [10.1103/PhysRevA.85.032111](https://doi.org/10.1103/PhysRevA.85.032111).
- [175] D. Andrew Golter, Thomas K. Baldwin, and Hailin Wang. “Protecting a Solid-State Spin from Decoherence Using Dressed Spin States”. In: *Physical Review Letters* 113.23 (Dec. 2014), p. 237601. DOI: [10.1103/PhysRevLett.113.237601](https://doi.org/10.1103/PhysRevLett.113.237601).
- [176] Michael A. Nielsen. “Optical Quantum Computation Using Cluster States”. In: *Physical Review Letters* 93.4 (July 2004), p. 040503. DOI: [10.1103/PhysRevLett.93.040503](https://doi.org/10.1103/PhysRevLett.93.040503).



- 
- [177] Kenneth Sharman et al. “Quantum repeaters based on individual electron spins and nuclear-spin-ensemble memories in quantum dots”. en. In: *Quantum* 5 (Nov. 2021). arXiv: 2010.13863, p. 570. ISSN: 2521-327X. DOI: [10.22331/q-2021-11-02-570](https://doi.org/10.22331/q-2021-11-02-570).
- [178] Miriam Neumann et al. “Optical Stark shift to control the dark exciton occupation of a quantum dot in a tilted magnetic field”. en. In: *Physical Review B* 104.7 (Aug. 2021), p. 075428. ISSN: 2469-9950, 2469-9969. DOI: [10.1103/PhysRevB.104.075428](https://doi.org/10.1103/PhysRevB.104.075428).